Selective Assembly in Deformable Systems Using Templated Assembly by Selective Removal

by

Gunjan Agarwal

B.E. Manufacturing Processes and Automation Engineering
Netaji Subhas Institute of Technology, Delhi University, 2007

SUBMITTED TO THE DEPARTMENT OF MECHANICAL ENGINEERING
IN PARTIAL FULFILLMENT OF THE REQUIREMENTS FOR THE DEGREE OF

MASTER OF SCIENCE IN MECHANICAL ENGINEERING
AT THE
MASSACHUSETTS INSTITUTE OF TECHNOLOGY

JUNE 2009

ARCHIVES

Author .....
Department of Mechanical Engineering
May , 2009

Certified by .....
Carol Livermore
Associate Professor
Thesis Supervisor

Accepted by .....
David E. Hardt
Chairman, Department Committee on Graduate Students

Selective Assembly in Deformable Systems Using Templated Assembly by Selective Removal

by

Gunjan Agarwal

Submitted to the Department of Mechanical Engineering on May 8, 2009, in Partial Fulfillment of the Requirements for the Degree of Master of Science in Mechanical Engineering

ABSTRACT

The current work presents the first demonstration of successful assembly of deformable polymer microspheres on patterned rigid substrates using Templated Assembly by Selective Removal (TASR). Also presented is a quantitative model for predicting the successful self-assembly of deformable materials using TASR.

Successful assembly of silica microspheres using TASR on a silicon template carried out in previous work has established that the technique works effectively for assembly of hard materials on a rigid substrate. However, the situation for the assembly of soft materials is different. In systems comprising soft materials, the contact area between the two mating surfaces can potentially change via deformation which influences the shape matching between the component and the substrate that TASR relies on as its underlying principle. The contact area at the interface is in turn decided by the nature of contact between the two interacting surfaces. Therefore, the Hertzian elastic theory for contact between a sphere was used for deciding whether the assembly of two new materials is attributed to shape matching or to plastic deformation. In accordance with the stated hypothesis, it was concluded that the assembly of Polystyrene (PS) microspheres on a rigid substrate such as silicon will yield successful results. Experiments were conducted to confirm this deduction from theoretical analysis.

The thesis presents simultaneous self assembly of 2 μm diameter polystyrene microspheres on a patterned silicon template, where grids with uniformly well-matched hole sizes were completely filled demonstrating nearly 100% assembly yield while grids with varying hole sizes demonstrate selectivity in assembly. Quantitative comparison of the data on assembly of deformable systems with existing TASR models for non-deformable systems shows significant agreement.

The predictive model for self assembly of deformable materials can pave the way for assessing the viability of trying out the assembly of a new material by comparing its parametric values with those that have already been successfully demonstrated and established.

Thesis Supervisor: Dr. Carol Livermore
Title: Associate Professor

Acknowledgement

I would like to thank Prof. Carol Livermore for her constant guidance and motivation throughout the course of this project. It is only through her invaluable support and motivation that I will be able to achieve this milestone in the process of learning at MIT, which started two years ago. Carol's meticulous supervision of my work, appreciation of ideas which lead us onto the right track while pointing out the flaws and suggesting improvements at the same time, during each and every step of my research at MIT has undoubtedly brought out the best in me. I owe my sincere gratitude to her for being not only my advisor and mentor, but also a friend whom I shall always look upon with admiration and respect.

A critical role has been played in this project also by my colleague and friend - Feras Eid, and I cannot thank him enough for his unabiding enthusiasm and patience with answering the smallest of my queries. The current work has been built brick by brick upon the foundation created by the pioneers of TASR – Feras Eid and Sunghwan Jung. Although Sunghwan is no longer a part of this group, his contribution to all of the later works on TASR since his own has also been immense, as he was the first to create the theory upon which the future of TASR rests.

I also take this opportunity to thank Amelia Servi, who is also a part of our research group and has contributed tremendously in this project. Without her wonderful fabrication skills, which are more of her innate talent than acquired expertise, this project would not be where it stands today.

Finally, I would also like to acknowledge the constant support and motivation provided by my parents, Dr. Narender Kumar Agarwal and Mrs. Neelu Agarwal. Their firm belief in me has kept me going strong always.

This work was supported by our sponsors from the National Science Foundation, UROP, and Pappalardo Graduate Fellowship and my sincerest thanks are due to them for their generosity.

Table of Contents

ABSTRACT **3**
ACKNOWLEDGEMENT **5**
TABLE OF CONTENTS **7**
LIST OF FIGURES **10**
LIST OF TABLES **16**

CHAPTER 1
INTRODUCTION TO TEMPLATED ASSEMBLY BY SELECTIVE REMOVAL

1.1 Concept of self assembly using TASR **18**
1.2 Previous work on assembly of rigid materials using TASR and motivation for the current work **23**
1.3 Conventional top-down fabrication vs bottom-up approach using TASR with deformable materials **26**
1.4 Applications of self-assembled deformable systems **28**
1.4.1 Optical meta-materials 29
1.4.2 Chemical and biological sensing applications 29
1.4.3 Shape and size-selective chromatography 30
1.4.4 Cell sorting 32
1.5 Thesis outline **33**

CHAPTER 2
THEORY AND MATHEMATICAL MODELING

2.1 Description of original TASR model **36**
2.1.1 Concept of the model 36
2.1.2 Interfacial energy 41
2.1.3 Contact area 43
2.1.4 Surface roughness 46
2.1.5 Retention and removal moments 48
2.1.5.1 Calculation of retention moment 48
2.1.5.2 Calculation of removal moment 49
2.2 Introduction to TASR modeling for deformable systems **53**
2.2.1 Classification of cases under consideration 54
2.2.2 Discussion of elasticity 56
2.3 Predictive model for TASR **59**

2.4 Hertzian theory of contact **60**
2.5 Model results and analysis **65**
2.5.1 Theoretical results for assembly of deformable microspherical components on rigid substrates 66
2.5.1.1 Assembly of microspherical components on a flat substrate 66
2.5.1.2 Assembly of microspherical components on a substrate with a finite radius of curvature 68
2.5.2 Method for verification of model results 71
2.5.3 Model extension to assembly of rigid microspherical components on deformable substrates 73
2.5.4 Model extension to assembly of deformable microspherical components on deformable substrates 76
2.5.5 Selected experimental study based on model results 78

CHAPTER 3
EXPERIMENTAL WORK

3.1 Outline of experiments **79**
3.2 Template fabrication **80**
3.3 Template and component preparation **85**
3.3.1 Template functionalization 85
3.3.2 Component preparation 86
3.4 Self-assembly protocol **87**
3.5 Comparative experimental study **89**
3.6 Fabrication of deformable template replicates **91**

CHAPTER 4
RESULTS AND ANALYSIS

4.1 Overview **96**

Experimental Results

4.2 Template fabrication results **97**
4.3 Simultaneous and selective assembly **98**
4.4 Variation of yield from template to template **102**
4.5 Influence of assembly parameters on yield **104**
4.5.1 Effect of voltage on transducer 104
4.5.2 Effect of volume fraction of water in assembly mixture 107
4.6 Results of comparative assembly **108**

Analysis and Discussions

4.7 Model Verification **110**

4.8 Uncertainty calculations.....121
4.9 Possibility of plastic deformation at the nano-scale.....124

CHAPTER 5
CONCLUSIONS AND FUTURE WORK

5.1 Conclusions.....129
5.2 Challenges for future work in progress.....131
5.2.1 Extension of theoretical modeling.....132
5.2.2 Approach to self-assembly of biological materials.....134
5.2.3 Approach to self-assembly of anisotropic materials.....138

References.....140

List of Figures

Figure 1.1: Schematic illustration of the experimental set-up for TASR including the assembly bath (in which variable chemistry and shape matching are implemented through the choice of materials and component/template geometry) and the 1.7 MHz ultrasonic transducer that introduces mechanical forces to the selective removal system 22

Figure 1.2: Schematic illustration of removal of components from incorrectly matched sites on the template surface by *roll-off* (Courtesy of Sunghwan Jung) 25

Figure 1.3: Schematic description of *shape and size selective chromatography* using templated assembly by selective removal. The mixture of desired and undesired components is flowed into the separation chamber containing a shape selective surface which assembles the desired components onto surface by TASR. These components can be recovered later by ultrasonic excitation.....31

Figure 1.4: (A) A sickle-cell anemia infected red blood cell (B) A healthy red blood cell in the human body. The marked difference in shapes of the healthy cell and the infected cell suggest their possible sorting using TASR which works on shape and size selectivity. (Image source : http ://www.carnegieinstitution.org/first_light_case/horn/lessons/sickle.html).....33

Figure 2.1: Graphical plot showing variation in interfacial energy of assembly fluid mixture comprising ethanol and water with the hydrophobic template surface vs. the variation in fraction of water in the assembly mixture. As the fraction of water in mixture increases, the interfacial energy of the system increases.....42

Figure 2.2: Schematic showing concept of rotation of coordinate axes used in calculation of nominal fractional contact area between spherical component and larger sized or matching hole of radius, r_h. Value of contact angle β is calculated to find the contact curve formed by points on hole within adhesive distance d_a of sphere and spherical integration for each value Φ is performed along the entire surface of sphere to find total contact area A_n (Adapted from [13]) 45

Figure 2.3: Schematic illustration of the difference in constraint conditions and degree of deformation in cases (A) A deformable sphere contacting a rigid substrate and (B) A rigid sphere indenting a deformable substrate under the application of load. The deformation is more pronounced in case (A) than (B) due to difference in constraining conditions.....55

Figure 2.4: Stress-strain curves for (A) perfectly elastic material (B) perfectly plastic material (C) elastic-strain hardening material (D) elastic-perfectly plastic material. Most of the materials under consideration for TASR can be described by the elastic-perfectly plastic model.....57

Figure 2.5: Stress-strain curve for a viscoelastic material. The shaded red area is a hysteresis loop which shows the amount of energy lost as heat in a loading and unloading cycle. Non-linear elastic behavior such as that shown here for certain materials might have to be considered for assessment of their applicability to TASR.....58

Figure 2.6 : Schematic description of deformable sphere of radius R pressed by a rigid flat due to application of contact load P. An interference ω is obtained upon the contact, with a circular contact region of radius a.....61

Figure 2.7: Graphical plot showing variation in interference ratio ω/ω_c with variation in radius of curvature for a deformable polystyrene microsphere being pressed on a flat silica surface by a contact load. In general, as the radius of component increases, ω/ω_c decreases. The results are obtained from the theoretical model for deformable systems in TASR.....66

Figure 2.8: Schematic illustration showing lesser room for deformation in case where assembly site has a radius of curvature R_t (negative) for the assembly of a spherical component (with a positive radius of curvature R_c) as opposed to a case of deformation of a sphere on a flat (with infinite radius of curvature).....70

Figure 2.9: Graphical plot showing variation in ratio of indentation pressure to yield strength of substrate, γ with variation in radius of curvature for a rigid silica microsphere indenting flat, deformable PS and PMMA surfaces. In general, as the radius of component increases, γ decreases very slightly, remaining almost constant. The results are obtained from the theoretical model for deformable systems in TASR.....75

Figure 3.1 : Schematic illustration of sequence for fabrication of assembly template. (A) Small patterns are exposed in oxidized Si wafer covered with resist using e-beam lithography. (B) Exposed spot are etched isotropically using BOE in order to produce desired hemispherical sites for component matching. (C) Template is covered with SAM to make it hydrophobic.....81

Figure 3.2: CAD layout of mask pattern used for fabrication of templated surface by electron-beam lithography. The numbers below each of the 15 grids shows the starting spot size used for that grid of spots on the e-beam tool (Courtesy of Amelia Servi).....82

Figure 3.3: Atomic Force Microscopy (AFM) images of holes with starting spot sizes (from (a)-(d)) of 50, 100, 200, and 500 nm. Smaller starting hole sizes correspond to better shape

matching with spherical components and therefore higher anticipated assembly yield (Courtesy of Amelia Servi) 84

Figure 3.4: Photographs of the assembly set-up used for TASR experiments. (A) An overview of the experimental apparatus used. (B) Optical microscope used for imaging the assembly template (C) A magnified view of a portion of the set-up in (A). A megahertz frequency acoustic transducer is kept at the bottom of a large beaker which is filled with water. A smaller assembly beaker is suspended above the transducer in the larger beaker into which the patterned assembly template is immersed face-up.....88

Figure 3.5: Optical micrograph showing visible distortion of polystyrene microspheres scattered on the silica template using 8% acetone-water assembly mixture at 40 V. The acetone causes swelling and dissolution of the polystyrene microspheres and causes failure of shape –matching of these components to the hemispherical sites fabricates on the templates for assembly using TASR.....90

Figure 3.6: Schematic description of the process for fabrication of deformable PDMS replicates off patterned silica templates by a two-step molding process using soft lithography.....93

Figure 3.7: Optical micrograph of PDMS replicate created off silica masters used in previous works [1-3] using soft lithography in order to demonstrate the concept of patterning deformable templates.....95

Figure 4.1: Optical micrographs of patterned template before assembly experiments using TASR. (A) Overview of four patterned grids with different starting spot sizes (B) Grid 0 comprised of uniformly sized holes with starting spot sizes of 45 nm (C) Grid 1 comprised of mixed 2x2 arrays of 45,100,200 and 500 nm starting spot sizes. Missing holes in grids are defects in e-beam lithography or developing process.....97

Figure 4.2: Optical micrographs showing polystyrene microspheres (2 micron in diameter) self assembled on a patterned silicon template using TASR. This demonstrates nearly 100% yield for a uniform array of holes with a starting resist opening 45 nm under these assembly conditions. Comparison with the known empty holes shown in Fig. 4.1 confirms that the circular patterns in these images are filled holes rather than empty ones 99

Figure 4.3: (A) Optical micrograph of section of template showing Arrays 1, 10, 101 and 110. While arrays 10 and 110 show uniform assembly, array 1 and 101 show selective assembly (B) Magnified optical micrograph of Array 1 (C) Schematic diagram of the repeated 2x2 pattern of different size/shape holes on the assembly template, with starting resist opening sizes of 500 nm (upper left), 200 nm (lower left), 100 nm (upper right), and 45 nm (lower right). (D) Optical micrograph of assembly into an array of holes comprising multiple units of the 2x2 unit pattern.

The holes with the largest starting size are all empty, while the better matched holes are all filled.....101

Figure 4.4: Optical micrographs showing variation in assembly yield from template to template under identical assembly conditions of 45 V and 8% water fraction by volume. The assembly yield varies from 60.64% in (A) to 61.3% in (B) to 57.4% in (C).....103

Figure 4.5: Optical micrographs showing effect of variation in voltage on the transducer on TASR assembly yield results. Experiments were performed at a water volume fraction of 8% with input voltages of: (A) 35 V, (B) 40 V, (C) 45 V, (D) 50 V, (E) 55 V, and (F) 60 V. Assembly yield climbs from a low value of 7% at 35 V to 98.9% at 45V before dropping down again to 6.5% at 60 V during the progressive increase in voltage.....105

Figure 4.6: Variation of fractional assembly yield and defects in assembly plotted vs. voltage on the transducer during assembly. The assembly yield first increases with increase in voltage, takes a peak value of nearly 100% at 45V and falls down sharply thereafter with subsequent increase in voltage. Assembly defects are observed to be low.....106

Figure 4.7: Optical micrographs showing variation in assembly yield with varying fraction of water by volume in assembly mixture, for water fractions of (A) 4% water (B) 8% water and (C) 16% water at 45 V. An assembly yield of 21.7% is obtained at 4% water, which increases to 99% on increasing water fraction to 8%, before dropping down to 8.7% at 16% water by volume in the assembly mixture.....108

Figure 4.8: (A) AFM section profile of a 50 nm hole on patterned silica template (B) 3-Dimensional view of the same hole in top view (C) 8^{th} order polynomial curve fit to the above AFM hole profile using SPIP software by Image Metrology.....112

Figure 4.9: Plot of fractional nominal contact area (Ratio of nominal contact area between microsphere and substrate to the surface area of sphere) versus starting distance from center of hole, r (nm) for hole with starting spot size as 50nm.....113

Figure 4.10: Fractional assembly yield and fractional nominal contact area plotted vs the starting spot size for holes on the patterned silicon template. As the starting spot size (and hence the hole size) increases, the fractional nominal contact area decreases and correspondingly, assembly yield also decreases.....114

Figure 4.11: AFM images showing 3-D surface plots and cross-sections of a polystyrene microsphere assembled in an assembly site on a silica surface, at different size scales ranging from a few microns in (A)-(B) to 100nm in (C)-(D), down to 10 nm in (E)-(F). Surface roughness parameters for polystyrene such as rms roughness and peak heights were obtained from these images (Images courtesy of Amelia Servi).....116

Figure 4.12: AFM images showing 3-D surface plots and cross-sections of a hole on the coated silica surface at different size scales. (A) and (B) show 3-D surface plots at size scales of 1 micron and 200 nm respectively while (C) and (D) are the corresponding sectional images of these plots. Surface roughness parameters for silica template such as rms roughness and peak heights were obtained from these images.....117

Figure 4.13: Plot of fractional assembly yield vs the ratio of retention moment to removal moment for assembly of both silica and polystyrene microspheres on a coated silica template.....118

Figure 4.14: Measured assembly yield plotted vs. the ratio of retention moments to removal moments (ret/rem values). The yield is plotted vs. the minimum, nominal and maximum values of ret/rem ratio, taking into account uncertainties in the intensity of the acoustic excitation due to spatial variation and the value of surface roughness.....123

Figure 4.15: Cross-sectional roughness analysis showing aspect ratios of nano-scaled peaks on the as-fabricated silica surface of the template at the patterned sites. (A) and (B) are top-views of two different locations inside a hole on the template surface obtained by atomic force microscopy. (C) and (D) are cross-sectional views of (A) and (B) respectively obtained using surface analysis SPIP software package by Image Metrology. Low aspect ratios in topography suggest that nano-scale plastic deformation of polystyrene microspheres due to asperities on patterned silica surface will be minimal if it occurs at all. 125

Figure 4.16: Plasticity Index, ψ plotted vs. radius of curvature of asperities, R on surface. As the radius of curvature increases, the value of Plasticity Index decreases. Purely elastic regime extends for values of ψ below 0.6 which are obtained for radii of curvature of 6 microns and above, while predominantly plastic regime extends for value of ψ above 1 which are obtained for radii of curvature below 2 microns.....127

Figure 5.1: (A) Image of healthy SF-9 insect cells (B) Image of enlarged SF-9 cells after infection with baculovirus. Cells labeled in blue with the help of a dye called Trypan Blue indicate dead cells after infection with virus (C) Optical micrograph of silicon master template created for sorting of the healthy cells from infected cells based on concept of size selectivity and self-assembly using TASR. (Images of cells taken from www.nexcelom.com).....135

Figure 5.2: Fabrication process flow highlighting key steps to be followed for creating silicon template masters for the purpose of cell sorting of different sized SF-9 cells using TASR.....137

Figure 5.3: Scanning Electron Microscopic image of one of the holes on the patterned silicon master template fabricated for self-assembly and sorting of SF-9 cells. The nearly isotropic hemispherical profile, with slight undercut observed is achieved by deep reactive ion etching of silicon.....137

Figure 5.4: Optical micrograph showing patterned silicon template with patterns containing both cylindrical as well as spherical assembly sites aimed at the simultaneous assembly of different shapes using TASR.....139

List of Tables

Table 2.1: Material properties of common materials considered for analysis[38].....65

Table 2.2 : Model results for different material combinations describing the case of a 2 micron diameter deformable microspherical component made of commonly available polymers contacting a relatively rigid substrate which is assumed to be made of silica.....67

Table 2.3: Theoretical model results for the polystyrene-silica assembly combination, taking into consideration the hole geometry for different starting hole sizes.....69

Table 2.4: Comparison of actual contact load and contact area for assembly combinations in comparison with critical values for transition from elastic to plastic regime.....72

Table 2.5: Model results for different material combinations describing the case of a deformable microspherical component, made of commonly available polymers contacting a replicatable deformable substrate, made of PMMA for a component diameter of 2 microns...77

Table 4.1: Key surface roughness analysis results obtained for the polystyrene components and patterned silica template surface using Atomic Force Microscopy and Nanoscope software (by Veeco).....115

Chapter 1

Introduction to Templated Assembly by Selective Removal

1.1 Concept of self assembly using TASR

The term 'self-assembly' is used to describe processes in which a disordered system of pre-existing components transform into an organized structure without external direction. As mentioned by Whitesides et. al. [1], self-assembling processes encompass several disciplines and occur within a range of scales. While a variety of self assembly techniques have been devised at several different scales, starting from the molecular scale where chemistry and biology assist the self-assembly process, to the meso-scale (from 100 microns-millimeters) where several conventional mechanical forces have been used to assemble components into diverse architectures, significant challenges still remain for assembly in the intermediate scale. Self assembly at the intermediate scale becomes much more challenging because of several factors such as uncertainties in intermolecular mechanisms, lack of control, and challenges in inspection and measurement [2-4]. However, it is also beneficial to achieve self-assembly at this scale because of the demands of diverse architectures created at this scale with applications ranging from chemical and biological sensing, to electronics and optics [5,6].

Various works in the past have successfully demonstrated some assembly capabilities at the intermediate scale by using different methods to overcome these challenges. Some of the common elements that have been used to help assist the assembly in such processes include forces to promote adhesion such as chemical forces, electrostatic forces, capillary forces, etc along with the geometric patterning of assembly surface. Many of these forces which drive the assembly process are relatively weak at the macroscopic scale, but become significant at the intermediate scale of interest.

Using these concepts, Aizenberg et al. [7] demonstrated the assembly of charged colloids onto patterned templates with the help of electrostatic and capillary forces. Here electrostatic forces were introduced at binding sites and were used to drive selective assembly of microspheres in a liquid while capillary forces were used to precisely position the microspheres at the centers of the binding sites during drying of the liquid. Similarly, Xia et al. [8] and Cui et al. [9] used capillary forces to drag and pack microspheres into holes predefined on the surface of a template, controlling the number of microspheres packed in each hole by the relative sizes of the microspheres and the holes. Chen et al. [10] demonstrated the assembly of colloids onto patterned templates, where electrostatic and secondary interactions were used to drive selective organization of microspheres onto regions of a substrate which were patterned with polyelectrolyte multilayer films. Using fluidic and gravitational forces, as well as shape and size selectivity to achieve self-assembly, Smith et al. [11] demonstrated the assembly of light emitting diodes into a silicon substrate. In the work of Cheng et al. [12], self assembly of block co-polymers was achieved by spin casting a block co-polymer over surfaces patterned with grooves to create periodic arrays of nanospheres. More recently, self-assembly of objects has

also been achieved by tethering them to DNA origami, building upon the concept of biologically-based self-assembly, as demonstrated by Sobey et. al [13] and Chhabra et. al. [14], using DNA–mediated self-assembly to control the positioning of gold nanoparticles and fluorescent molecules termed "fluorophores". All of the previous works on self-assembly discussed here have successfully demonstrated different subsets of the attributes required for practical implementation of assembly techniques, such as precision, selectivity, scalability, compatibility, etc. The current work introduces an extension of a flexible, site selective self assembly technique that seeks to address many of these challenges simultaneously. This technique is called Templated Templated Assembly by Selective Removal (TASR).

TASR is a unique approach to self assembly at that relies on a fundamentally shape and size selective mechanism for assembling components onto surfaces at the micro and nano scales. TASR enables simultaneous assembly of diverse components into complex and highly precise systems with a range of potential applications. TASR may be used either as a permanent or as a reversible assembly process, enabling its use not only for construction of final systems but also for applications such as chromatography.

TASR employs a combination of chemistry, surface topography and controllable ultrasonically-induced fluid forces to assemble diverse sets of objects selectively from fluid into designated sites on a 2D surface [2-4]. Figure 1.1 shows a schematic diagram of the assembly set-up. The components and substrate, after undergoing chemical surface modification by coating with an adhesion promoter, are placed in a fluid environment for the assembly process, and megahertz frequency ultrasound is applied to the fluid. Competition between the chemical adhesive effects and fluidic removal effects drive the selective assembly. Components remain

assembled in a given assembly site when adhesive effects are stronger than removal effects; otherwise, they are removed. The assembly selectivity (that is, whether adhesive or removal effects are dominant) depends in part on the degree to which the component to be assembled matches the shape and dimensions of the surface topography at that location. The surface topography is designed such that holes at various locations in the substrate surface match the shapes of the components that are intended to assemble there.

The TASR concept has been demonstrated previously with silica microspheres assembled on patterned silicon substrates, and a model has been created to explain the assembly of rigid components on a rigid substrate [2-4]. Because TASR depends on shape and size matching between surfaces, the assembly of more deformable materials (i.e. materials in which deformation can change the degree of apparent shape matching between component and substrate) is more challenging. The current work presents analysis and experiments on the extension of the TASR technique to deformable materials. Such materials may be used for applications ranging from assembling functionalized polymer particles for chemical or biological sensors, to creation of optical meta-materials, to shape- and size-based sorting of biological materials such as cells. For simplicity, assembly of deformable materials will be considered here for spherical components; however the analysis and techniques are readily extendable to many non-spherical shapes.

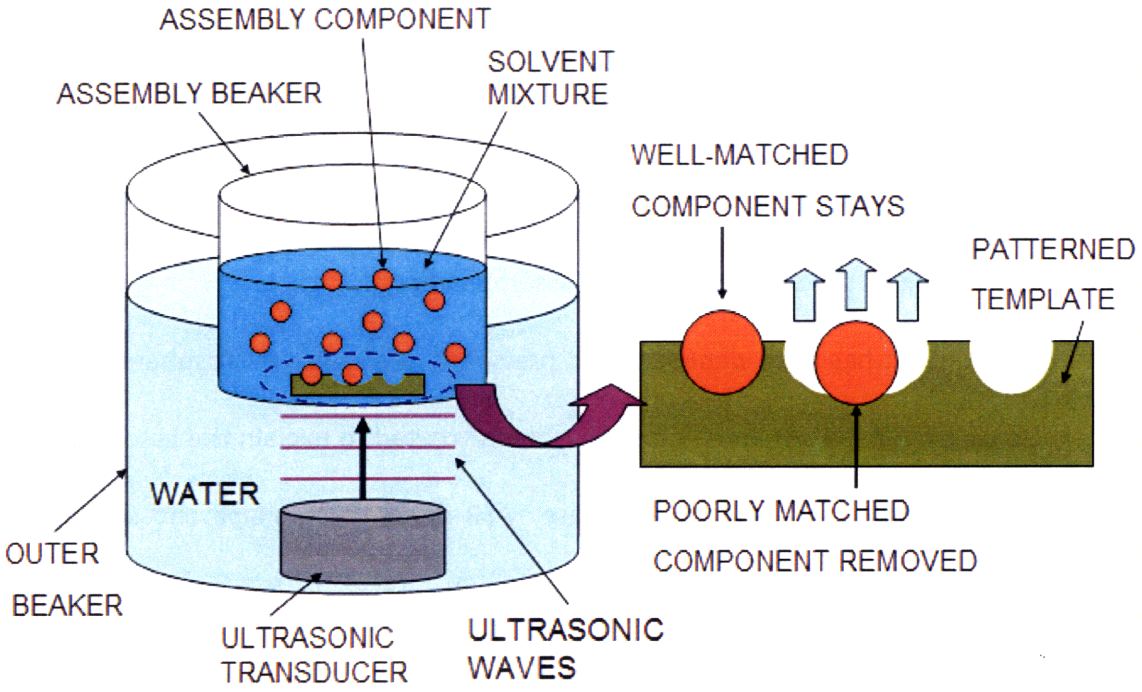

Figure 1.1: Schematic illustration of the experimental set-up for TASR including the assembly bath (in which variable chemistry and shape matching are implemented through the choice of materials and component/template geometry) and the 1.7 MHz ultrasonic transducer that introduces mechanical forces to the selective removal system

1.2 Previous work on assembly of rigid materials using TASR and motivation for the current work

As stated before, the TASR approach has been demonstrated experimentally and modeled theoretically for the self-assembly of rigid materials such as silica on silicon template surfaces in previous work [2-4]. Sunghwan Jung et. al. [2] did a proof-of-concept demonstration of TASR and established for the first time that the technique can work effectively; in particular, his work demonstrated TASR's effectiveness for assembly at the micron scale. The experimental concept was extended and developed further by Feras Eid et. al. [3-4], who extended the idea of *selective* self-assembly to *simultaneous and selective* self- assembly of different sized micro and nano components onto specific locations on an assembly template.

A theoretical model was first proposed by Jung et. al. in [2] and verified in [2-4]. The foundations of this model were based on the basic concept of TASR which is stated as follows. In order to achieve self-assembly, components which are to be assembled, as well as the template onto which they are to be assembled, are placed in a fluid environment. The use of fluid media is a natural choice, since many micro-components are manufactured and kept in the form of dispersions in fluid media. In addition, the interaction between the components and substrate in the fluid medium may be tailored to promote the assembly process.

There are several means by which the surfaces of interest can be made to adhere to each other in a medium such as oil, for instance. By creation of *hydrophilic* surfaces on both the component to be assembled as well as the template onto which it is assembled, the two surfaces can be made to adhere to each other in the oily, non-polar medium. Another way of

driving adhesion between mating surfaces for the purpose of self-assembly can be by the creation of *hydrophobic* surfaces in a polar fluid medium such as water. This concept of creating hydrophobic surfaces is used in TASR in order to achieve selective self- assembly by shape and size matching. Although other forms of component-substrate attraction exist (such as gravitational, electrostatic, or magnetic interactions), hydrophobic interactions are compatible with the TASR mechanism because the strength of the component-substrate interaction scales linearly with the area of contact between the component and the substrate, as discussed below.

In this implementation of TASR, hydrophobic surfaces adhere in water-based fluid media, and the strength of these *adhesive forces* between surfaces is dependent on the contact area and hence the degree of shape matching between the component and the substrate. At the same time, the assembly fluid is excited by an ultrasonic beam at a megahertz-range frequency in order to drive TASR's selective removal process and also to ensure the circulation of components. The *mechanical forces* that are applied to the components as a result of this ultrasonic excitation attempt to remove the components from the surface. While the adhesive retention forces dominate in sites where the shape of the component is well-matched with the topography on the template (so that the component stays in the site), the mechanical removal forces emerge stronger in a poorly matched site (so that the component is removed from the site). The mechanism by which these poorly-matched components are removed from the site is best described as *roll-off,* and is depicted in a schematic illustration in Figure 1.2. The net result is that holes that are well-matched to a type of component that is present in the fluid medium

are filled with those components, whereas holes that are poorly-matched to the components remain empty at the end of the TASR process.

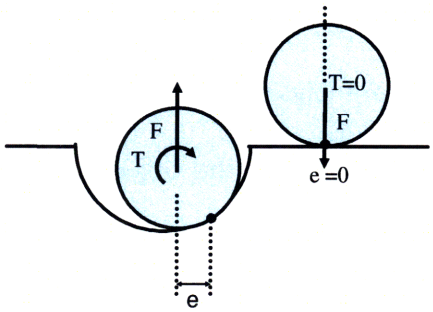

Figure 1.2: Schematic illustration of removal of components from incorrectly matched sites on the template surface by *roll-off* (Courtesy of Sunghwan Jung)

Prior modeling [2-4] determined that rigid assembly components are rolled out of poorly-matched assembly sites by a combination of fluid forces. This removal occurred when the removal moments generated as a result of these removal forces exceeded the retention moments generated as a result of the retention forces due to adhesion.

It was then concluded that the variation in assembly yield (quantified in terms of the number of holes on the patterned template surface that were filled by the assembly process out of the total number of holes of that size on the template) was related to the progressive increase/decrease in the ratio of the mechanical moments that promoted component retention to the mechanical moments that promoted component removal. Yield approached 0% when the removal moment due to fluid forces exceeded retention moment due to adhesion forces and approached 100% when retention moments exceeded removal moments. Further details of the concept of TASR as well as the theoretical model for TASR proposed and verified in previous work [2-4] are described at length in Chapter 2, Section 2.1.

Based on this theoretical framework, we seek to describe also the assembly of deformable systems and compare the assembly trends in rigid systems with those in deformable systems. However, since the retention moment is closely related to shape matching between the components and the substrate, the analysis becomes more challenging for soft, deformable systems where the possibility of a change in the original shape of the object on account of deformation must also be considered. In order to address this case where a deformable object might change its shape in order to increase its contact area with another object, we propose here a new theoretical model that complements the original TASR model [2-4] for the case of deformable objects. Details of the theory for analyzing deformations and creation of a mathematical model for predicting the self-assembly of new materials are described at length in Chapter 2.

1.3 Conventional top-down fabrication vs bottom-up approach using TASR with deformable materials

Conventional micro-fabrication processes are top-down processes in which a material is produced in bulk and then shaped into a finished part by a variety of processes. There are certain limitations in the kind of structures that can be created by means of this top-down approach. For example, in conventional micro-fabrication, one is required to carry out the desired fabrication steps in a certain order only, since a slight variation from the conventional sequence, such as the use of certain chemicals near the end of the process might damage a structure created at the beginning of the process. Similarly, one might not be able to create a

particular structure on the starting substrate material as this might require the introduction of factors like the use of high temperatures that a structure already created on the substrate cannot tolerate. TASR can play an important role in such situations since it can overcome the process incompatibilities in micro and nanofabrication. The strength of self assembly using TASR lies in the fact that it enables a method of creating the components separately, by means of the most effective process, and then their integration afterwards into the final system. By means of this technique, one can then address the issues of chemical or thermal incompatibilities in the original synthesis processes for each type of component individually. Therefore, by taking advantage of the fact that one can build up from the nano-scale to the macro-scale in processes such as TASR as opposed to the reverse way around in conventional techniques, diverse self-assembled architectures can be created from scratch using the bottom-up approach that TASR relies on.

In parallel with analyzing the techniques that can be used in order to create more precise and efficient systems, it is also worthwhile to investigate the spectra of materials that can be worked upon to manufacture systems using either approach to manufacturing. Deformable materials such as polymers and their self assembled architectures pose for an interesting study in this context of manufacturing using the bottom-up approach. Some of the advantages of incorporating polymers into our systems are that most polymers available today are fairly inexpensive, flexible, transparent to visible and ultraviolet radiations. Most polymers can be easily molded and their surface properties are easily modified. Many polymers possess improved biocompatibility or bioactivity over conventional materials such as silicon which are toxic. This makes polymers better suited for biological applications such as medical implants or

drug delivery devices. Deformable components made of polymers and biological materials are also important for several other applications, such as optically-based chemical or biological sensors. TASR, which works using the bottom-up approach, can potentially act as an efficient and precise method of creating systems out of deformable materials for these applications, as after building the sensing components separately, one can then assemble and integrate them into the final system. Thus, investigating the self-assembly of deformable materials such as polymers using TASR holds promising potential for comparison with traditional semiconductor fabrication techniques in an effort to achieve better precision and a higher efficiency for the same application with the use of minimum resources. At the same time, new applications with deformable structures created using techniques such as TASR which are not possible to achieve with conventional approaches also provide motivation for further study.

1.4 Applications of self –assembled deformable systems

Some of the potential uses of self-assembled deformable systems include optical meta-materials, chemical or biological sensors, biological cell-sorting devices, and shape and size-selective chromatography. TASR is a powerful tool for creating diverse systems from such deformable structures. Each of these potential applications of TASR is discussed in the following sections.

1.4.1 Optical meta-materials

A metamaterial is a material that gains its properties from its structure rather than its composition. Since the *structure* of meta-materials is of specific interest in regulating their functionality, self-assembly of these materials using TASR or other techniques can create the desired architecture from the materials of choice. Metamaterials hold special relevance in electromagnetism, especially optics and photonics [6,15-16].

Optical metamaterials, in particular, are of special interest to us since TASR is a technique for self-assembly which works best in the intermediate scales of a few nanometers to a few microns and this makes it potentially well matched to optical length scales. Once assembled using the appropriate technique, 3-D optical metamaterial structures possessing unique properties on account of their structure, such as a negative refractive index or negative magnetic permeability, can be used for applications such as bending light backwards, which is then further exploited in applications such as *invisibility* or creation of *superlenses*. These superlenses can then be used for the creation of better microscopes and imaging instruments [17-18]. Specifically considering the case of polymers, the markedly different optical properties of different polymers can also be fully exploited to achieve a variety of optical effects once they have assembled into the requisite configuration.

1.4.2 Chemical and biological sensing applications

Self-assembled systems of deformable structures created using TASR can also serve as chemical or biological sensors. In this application, the surfaces of the components would first

be functionalized to enable them to sense the chemical or biological species of interest. When species bind to these types of functionalized components, the optical properties of the components are modified. This can enable a form of "*molecular recognition*" of biological and chemical species. Examples of this include detecting changes in the optical fluorescence signal from a functionalized microsphere [19], or detecting changes in the optical resonant frequency of whispering gallery modes of functionalized microspheres upon attachment of a single molecule to the functionalized surface [20-21]. The subsequent selective assembly of these components onto different regions of a surface by TASR may then be exploited to code chemical sensitivity into spatial information in the final self assembled system or to make measurements of the presence of various species at a range of specified locations within the final system.

1.4.3 Shape and size-selective chromatography

The underlying concept of selectivity in TASR can be extended to develop a new kind of chromatography that is simultaneously shape and size selective. Such a technique can be useful in filtering applications such as sorting chemical synthesis products in the 100 nm to 250 nm scale [22], or for filtering different crystal polymorphs of a pharmaceutical compound to retain only the desired biologically effective form. The working principle of the concept is shown by the schematic diagram in Figure 1.3. The template is first created with features to match the shape and size of the desired components to be assembled onto it. The assembly mixture containing both the desired components that we want to assemble as well as those that are required to be filtered out is then flowed into a chamber which contains the shape and size

selective patterned template surface. Well-matched components are assembled onto the patterned surface using TASR. The desired components are hence retained onto the surface and are separated out from the mixture. These components can then be recovered back to some extent for further use by removing them from the template surface. The removal process will separate out some but not all of the components, since TASR works best and most quickly in the presence of an oversupply of components. Ideally, this entire separation process using TASR will at least exclude all unmatched components from the assembled system.

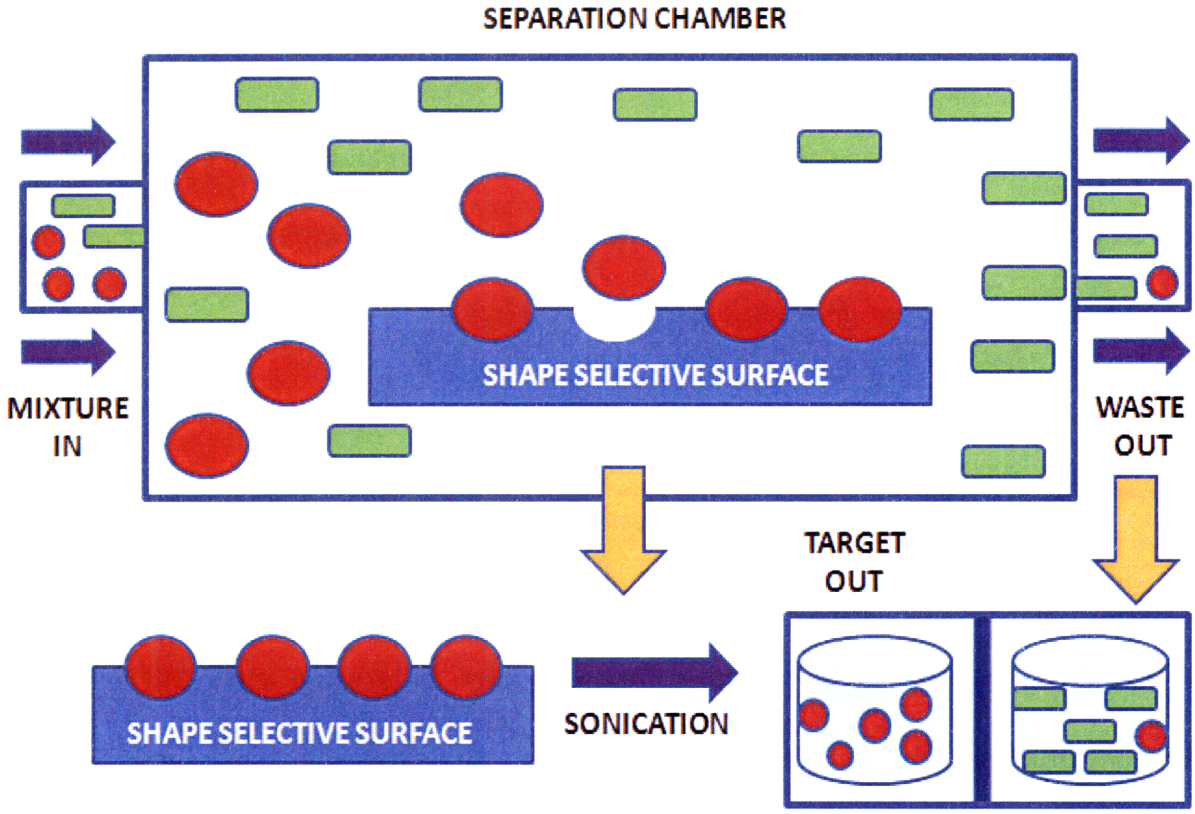

Figure 1.3: Schematic description of *shape and size selective chromatography* using templated assembly by selective removal. The mixture of desired and undesired components is flowed into the separation chamber containing a shape selective surface which assembles the desired components onto surface by TASR. These components can be recovered later by ultrasonic excitation.

There already exist techniques which utilize the concept of chromatography for separation of components based on *size selectivity*. One such technique [23] that has been developed based on this principle uses porous particles to separate molecules of different size wherein molecules that are smaller than the pore size can enter the particles and therefore have a longer path and longer transit time in the separation chamber than larger molecules which cannot enter the particles. Different molecules therefore have different total transit times through the separation column, and the technique works on *selective permeation*. However, such techniques do not take into account the shape of the molecule, and it is not possible to separate components roughly of the same size using techniques that have been previously developed. The significance of TASR as a technique for chromatography therefore lies in the fact that it simultaneously selects according to *both the size and the shape* of the object under consideration for purposes of either separation or assembly.

1.4.4 Cell sorting

TASR can also be used as a tool for biological applications. Cell sorting is one possible application of shape and size selective chromatography as discussed above. All cells exhibit different structural, physical and chemical interactions with external materials, and TASR might not be applicable to all cells, as the shape and size of certain types of cells is not very clearly defined. However, in certain other cases such as red blood cells (RBC) in sickle cell anemia, the ordinary doughnut form of the RBC is markedly distorted into the sickle-shape, as depicted in Figure 1.4. Since red blood cells are fairly robust in terms of shape and size, TASR may be used

in such cases in order to sort the healthy cells from the infected cells for the purposes of infected cell count taken from a blood sample.

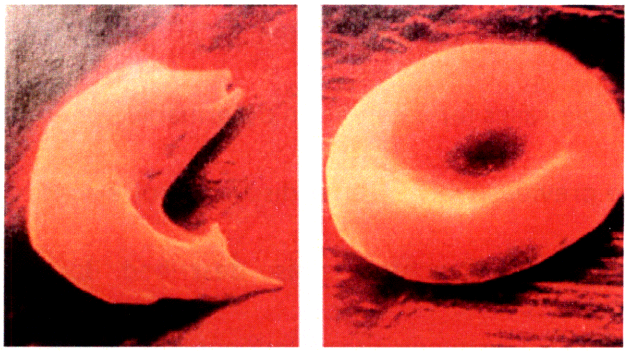

(A) (B)

Figure 1.4: (A) A sickle-cell anemia infected red blood cell (B) A healthy red blood cell in the human body. The marked difference in shapes of the healthy cell and the infected cell suggest their possible sorting using TASR which works on shape and size selectivity. (Image source : http ://www.carnegieinstitution.org/first_light_case/horn/lessons/sickle.html)

1.5 Outline of thesis

The thesis is divided into five chapters. Chapter 1 aims at providing an *introduction* to the basic concept and purpose of Templated Assembly by Selective Removal. Until this point, the principle of TASR has been introduced wherein competition between adhesive retention forces and mechanical removal forces drives the selectivity of the self-assembly. Previous experimental and theoretical work done in this field for assembly of rigid components on rigid patterned templates have also been described [2-4]. Based on a thorough interpretation of the relevance of the original TASR model, the need for a new theoretical model is introduced; this

model should address the issues of deformability in the assembling system. Various potential applications of deformable materials assembled using TASR are then discussed.

Chapter 2 introduces the *theoretical framework* for modeling the assembly of deformable materials. The original model for TASR-based assembly of rigid structures on rigid substrates is reviewed. Then the possible cases for assembly in deformable systems are discussed along with their relationship to the previous work. A brief discussion of elasticity pertinent to the theory for self-assembly of deformable structures is also described. Based on the Hertzian contact theory for analysis of contact between the component to be assembled and the substrate surface, a mathematical model is proposed which describes whether deforming components will deform elastically or elastically/plastically, and hence whether TASR will be effective. Relevant to the current experimental thrust, the case of assembly of deformable components on rigid substrates is analyzed in detail, and model results are tabulated. A polymer of interest for experimental purposes (polystyrene) is then identified.

Chapter 3 describes the *experimental work* carried out in order to demonstrate and characterize the self assembly of polystyrene microspheres on patterned silica substrates. The fabrication process of the silica templates for self-assembly is described. Subsequently, template and component preparation and the experimental protocol for assembly are discussed. Finally, solvent selection and template replication methods are discussed.

Chapter 4 focuses on *experimental results and analysis*. Results for the assembly of polystyrene microspheres 2 micron in diameter on patterned silica substrates are presented. Assembly in holes of uniform size/shape is compared with assembly in holes of different sizes/shapes for establishing selectivity of assembly for deformable materials. The dependence

of assembly results on assembly parameters is presented, along with the results of comparative experiments as discussed in Chapter 3. The results obtained from experiments are then analyzed using the original TASR model and the expanded model for TASR based on the theory of elastic/plastic contact.

Finally, Chapter 5 presents the *conclusions and scope for future work*. A brief summary of the goals achieved by the current work and recommendations for future work are presented.

Chapter 2

Theory and Mathematical Modeling

2.1 Description of original TASR model

2.1.1 Concept of the model

A brief introduction to the concept of TASR and the previous work done in this domain were discussed in Section 1.2 in Chapter 1. This section describes in detail some of the key ideas and theoretical formulations from the original TASR model. Although this model was proposed and verified in previous work [2-4], it will be of relevance in later sections for the purposes of comparison with the current work.

As discussed before, the key elements in TASR are the components and the patterned substrate that they are to be assembled onto. Self-assembly is achieved by creating adhesion forces between interacting surfaces of the component and the substrate. The strength of this adhesion is controlled by the interfacial energy and by the degree of shape and size matching of the components to features on the template surface. It is the adhesion forces that are responsible for retention of components on the substrate in sites where the components are well matched to the template topography in the presence of removal forces, the origin of which will be discussed in greater detail in following sections.

Adhesion in this system, as also in previous work on TASR [2-4], is achieved by working with hydrophobic surfaces in a fluid that contains water. For this purpose, the components and the substrate are coated with a self-assembled monolayer (SAM) that makes the surface hydrophobic (if not hydrophobic naturally, as certain polymeric materials such as polystyrene and PDMS are). Silane-based SAMs, such as Octadecyltrichlorosilane ($CH_3(CH_{22})_{17}SiCl_3$), or OTS for short, is one such adhesion promoter that has been used in previous work [2-4] in order to make the surface of a material such as silica hydrophobic. The organic tails of the OTS increase the interfacial energy with water, thus generating the hydrophobic effect and promoting component-substrate adhesion.

These hydrophobically-coated components and the coated template are then placed in the assembly mixture, which is a solvent/water mixture. The assembly mixture contains a certain fraction of water for promoting adhesion of hydrophobic surfaces, and regulating this fraction of water can affect assembly results by affecting the degree of adhesion between interacting surfaces. The assembly mixture also contains an appropriate solvent; the relative amounts of solvent and water control the interfacial energy of the system (described in section 2.1.2). The interfacial energy relates the contact area between two materials to the total free surface energy. Self-assembly, including TASR, works by minimizing the free energy of the system. It is energetically favorable for hydrophobic surfaces to stay in contact with each other in a water based environment, as this lowers the free energy of the system as compared with the case in which the surfaces are apart. Choosing the right solvent and using an appropriate fraction of this solvent in the assembly mixture is critical for achieving the desired interfacial energy in the system and correspondingly, high assembly yield results.

Whereas tailoring the chemistry adjusts the strength of the adhesion per unit area, shape matching increases the area of contact and hence the total strength of the component/substrate adhesion. Shape matching between the components and the features on the substrate then leads to adhesion in the correct sites upon interaction of hydrophobic surfaces in the assembly mixture. The adhesion achieved as a result generates both adhesive forces and adhesive moments that counteract any forces or moments that may act to remove the components from binding sites. These adhesive moments, which will be referred to here as retention moments, are responsible for binding the components most strongly to well-matched sites. Retention moments (which are covered in greater detail in section 2.1.5.1) are related to the change in contact area (described in section 2.1.3) between the component and the substrate in transition from one location to another and to the interfacial energy of the system. Retention moments are thus a measure of the resistance felt in moving the component from one location, where it has a given contact area with the substrate, to another location, where the contact area and the interfacial energy are different.

The initial assembly of components onto substrate is random, since it results from essentially random circulation and since all surfaces immersed in the assembly mixture are essentially hydrophobic and can adhere at any location. It is the removal process in TASR that drives the assembly process' ultimate selectivity. Removal moments are generated in the system by fluidic forces produced by high frequency acoustic excitation of the assembly mixture. A megasonic flow field is generated by the acoustic transducer (which operates at a frequency of 1.7 MHz) and apart from inducing the circulation of components in the flow field, the excitation also produces different kinds of forces – oscillatory as well as non-oscillatory that

act on the component. A subset of these forces (and the mechanical moments that they can produce) tends to remove the components from the substrate by rolling the component out of the site on the template using a mechanism called "roll-off" [2-4]. Depending on whether the moments that promote retention are stronger than the moments that promote removal, or vice versa, the components will be either retained or removed. Therefore, by controlling the magnitudes of these removal and retention forces and moments, selective assembly can be achieved.

The original TASR model [2-4] stated that the retention of the component in a site takes place when the retention moments generated as result of the forces that promote component adhesion to the patterned surface exceed the removal moments which try to remove the component from the site; this promotes the retention of components in well-matched sites. On the other hand, removal from a site takes place when moments that promote component removal (which are generated as a result of the ultrasonically induced fluid forces) exceed the moments that promote component adhesion; this promotes the removal of components from poorly-matched sites. Prior modeling described how assembly yield varies with the ratio of retention moments to removal moments. It was established theoretically and experimentally by both Jung [2] and Eid [3-4] that as this ratio increased from a value below about one to above about one, progressively higher assembly yield was recorded. When the retention moments were less than the removal moments, the assembly yield was low, approaching zero value. When the retention moments became approximately equal to the removal moments (at a ratio of approximately one), the yield increased sharply. For further increases in this ratio, the

retention moments dominated over the removal moments and assembly yields as high as nearly 100% were recorded experimentally.

2.1.2 Interfacial energy

The interfacial energy between a solid and a liquid surface is defined by the Young's equation which states:

$$\gamma_s = \gamma + \gamma_L \cos\theta \quad (2.1)$$

where γ_s is the energy of formation of the solid surface, γ_L is the surface tension of the liquid , γ is the interfacial energy between the solid and liquid interface, and θ is the contact angle between the liquid-solid interface. Measurement of interfacial energy is carried out by measuring the contact angle θ using goniometry once we know the values of γ_s and γ_L.

It is to be noted here that actual contact angle measurements for measurement of the interfacial energy were not carried out here. Instead, literature values [24-25, 39-40] were used to quantify the interfacial energy of solvent-water mixtures as a function of the fraction of water in assembly mixture, to obtain trends similar to that in previous work [2-4]. Figure 2.1 shows the graphical plot for variation in the interfacial energy of an ethanol water-mixture with the substrate surface for variation in the fractions of water (by weight) in assembly mixture. Values of interfacial energy of the solvent-water mixtures at concentrations of water other than those plotted in the figure can also be calculated from the plot by means of interpolation. It is also to be noted that only the nominal values of interfacial energy are plotted here. However, there might be variation in these values of interfacial energy due to variation in measurement of contact angle which, depending on whether is advancing or receding will have slightly different values.

Since these values of interfacial energy of solvent mixture with the hydrophobic template surface are different for different solvents, therefore, as mentioned before, choosing the right solvent with an appropriate fraction of water in assembly mixture is crucial in deciding the interfacial energy of the system at which best assembly results will be obtained. Although the trend for increase in interfacial energy of the mixture with increase in fraction of water in the assembly mixture is observed to be the same here for an ethanol-water assembly mixture when compared with the trend for acetone-water assembly mixture as recorded in previous work [2-4], values of interfacial energy for two different solvent mixtures at the same fraction of water in the mixture will be different. Therefore, the right solvent must be chosen for assembly using TASR depending on the components to be assembled.

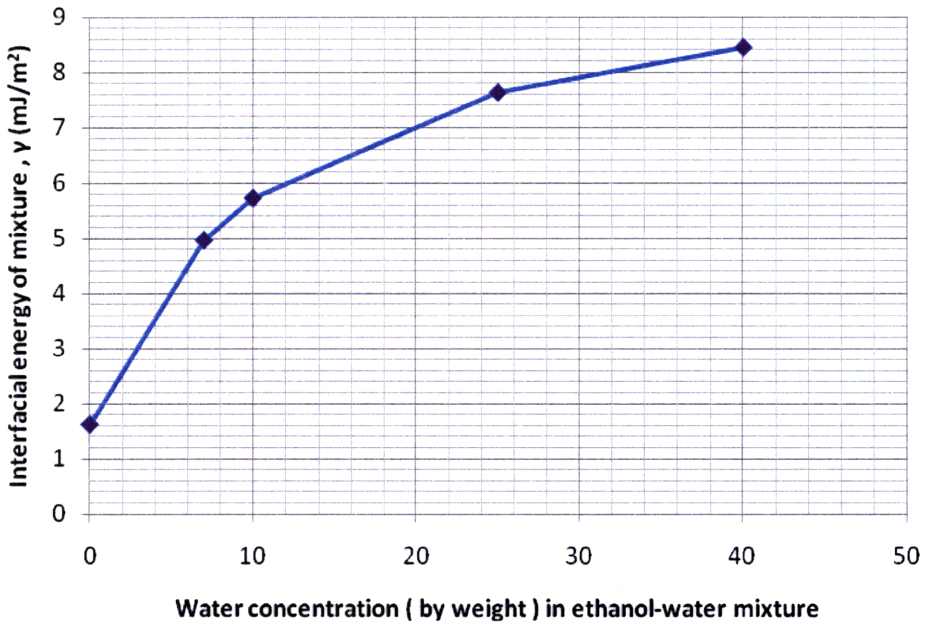

Figure 2.1: Graphical plot showing variation in interfacial energy of assembly fluid mixture comprising ethanol and water with the hydrophobic template surface vs. the variation in fraction of water in the assembly mixture. As the fraction of water in mixture increases, the interfacial energy of the system increases.

2.1.3 Contact area

Contact area calculations were done in order to calculate the retention moments and to study the effect of fractional contact area on assembly results. This section describes succinctly the outline of the approach used in previous work [2-4] to calculate numerically the nominal fractional contact area between the spherical component and the hemispherical hole. Only spherical components and axisymmetric holes are considered here. Nominal contact area between component and substrate does not take into account the surface roughness effects. Rather, it is the area over which the nominally smooth surfaces of the component and template are separated by no more than a specified distance d_a where the component is located at a given position on the substrate's surface [4]. This 'adhesive distance' d_a represents the range of action of adhesive surface forces and is taken to be 1.5 nm based on literature values [2]. The *contact curve* between the spherical component and the hole (binding site) on the template is then defined by identifying the points on the sphere that are within this adhesive distance of the binding site surface ; points on the sphere at a distance from the hole outside of this range are assumed not to be in contact. It should be noted that we have assumed here that the sphere's diameter is smaller than that of hole, which is a valid assumption for the cases that will be discussed using this approach in Section 4.6.

Although the basic principle used is simple, contact area calculations become complicated because the shape of the holes obtained on the template surface after the fabrication process (discussed in detail in section 3.2) is not exactly hemispherical due to factors such as finite lithographic feature size, resist delamination etc., so that the surface diameter is larger than it would be for a hemispherical hole of the same depth. It is therefore necessary to calculate the

contact area numerically [4]. Atomic Force Microscopy is therefore used to obtain the hole shape profiles, which are determined to be approximately axisymmetric. A commercial surface analysis software package (SPIP by Image Metrology) is then used to fit an 8^{th} order curve of the form y=f(x) to the cross-sectional AFM profile, where y is vertical distance from the bottom of the hole and x is the radial distance from the centerline. The sphere is now assumed to roll along the hole from the lowermost point in the cross-section (also defined as the origin of the *global coordinate frame of reference (x,y,z)* as shown in Figure 2.2) to any point A on the sphere surface along the sidewall with coordinates (xa, ya, 0) with respect to the global axes. Sphere rolling is assumed to take place in the same plane as the cross-section of the hole. Therefore, z=0 for point A on the sidewall which is the contact point between the sphere and the hole. A second coordinate system, the *body-fixed frame of reference (X, Y, Z) is* now defined on the sphere to study points on the sphere surface, origin of which is defined at the sphere's center. The contact area calculation algorithm is essentially based on the concept of rotation of these coordinate axes frames and is thus compatible with any sphere-hole configuration.

The algorithm discretizes the path covered by the sphere during rolling inside the hole into points at horizontal distance x_a from the center of the hole, the range starting at a distance x=0 and ending at the radius of hole x= R_{hole}. The y coordinate for each of these points is obtained from the relation y=f(x) that describes the geometry of the hole. A conditional loop is then set up to calculate values of angles β_1 and β_2 (where β_2 is above the contact point and β_1 is below it) at which at which equation for the hole is satisfied for values of distance from the sphere center of ($R_{component}$+da). In other words, β_1 and β_2 describe the farthest angular extent of the points on the hole that are within adhesive distance of the sphere, where $R_{component}$ is the radius

of the spherical component. This defines the contact curve between the sphere and the hole. For each value of azimuthal angle Φ, which is the angle between the plane of the cross-section of hole and the plane passing through the sphere center and the examined point on sphere surface, the value of these contact angles is calculated and then spherical integration is performed numerically to calculate the contact area A_n, which is finally given by the expression:

$$A_n = nR^2_{component}\Delta\phi\sum\sum_{1}^{n}(2-\cos\beta_1-\cos\beta_2) \qquad (2.2)$$

where n ΔΦ= π radians [3-4].

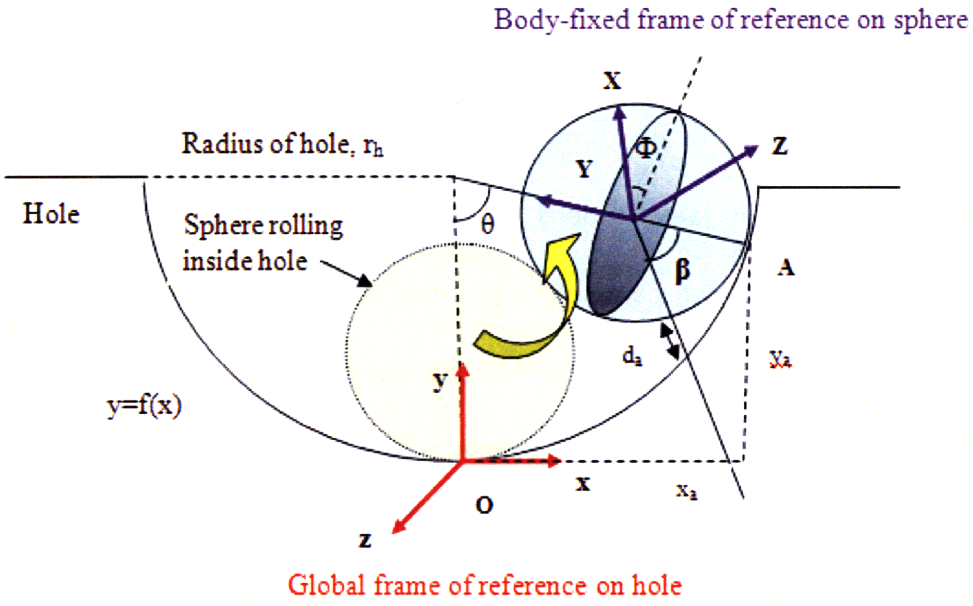

Figure 2.2: Schematic showing concept of rotation of coordinate axes used in calculation of nominal fractional contact area between spherical component and larger sized or matching hole of radius, r_h. Value of contact angle β is calculated to find the contact curve formed by points on hole within adhesive distance d_a of sphere and spherical integration for each value Φ is performed along the entire surface of sphere to find total contact area A_n (Adapted from [4]).

2.1.4 Surface roughness

In order to calculate the real contact area, the surface roughness effects have to be taken into account. This surface roughness might originate from either the non-uniformity of the surface's hydrophobic self-assembled monolayer coating or from the fabrication process itself, which involves some steps that can potentially induce surface roughness. The real contact area (taking into account the roughness, is a fraction of the nominal contact area calculated numerically following the approach highlighted in section 2.1.3 because roughness may bring some points on the surface out of the contact distance . Therefore, a roughness factor was defined in order to assess how much of the nominal contact area between the interacting surfaces is in contact in reality. Step-by–step calculation of this roughness factor is described in detail in previous work [2-4]. Here we summarize only the key equations that are used for analysis of surface roughness in later sections. In order to describe the surfaces of both the components and the substrate, two parameters are used to describe each surface: the mean surface roughness (rms) value, σ and the peak height, h. For calculation of these values, a coordinate system is defined with x as the axis parallel to the surface and a reference plane z=0 for the heights z(x) of asperities above the surface. The root mean square roughness, σ over a section of length L along the x-axis is then calculated using the relation below:

$$\sigma^2 = \frac{1}{L}\int_0^L z^2 dx \qquad (2.3)$$

Peak height is the height of the largest asperity as measured from the reference plane z=0 over surface length L.

The equivalent surface roughness takes into account the rms roughness values for both the component and the template , $\sigma_{component}$ and $\sigma_{template}$ respectively, and is calculated using the relation:

$$\sigma_{eq} = (\sigma^2_{template} + \sigma^2_{component})^{\frac{1}{2}} \quad . \quad (2.4)$$

Following a similar approach, the equivalent peak height is given by the relation:

$$h_{eq.} = \frac{1}{2}(h_{template} + h_{component}) \quad , \quad (2.5)$$

where $h_{template}$ and $h_{component}$ are the peak heights of the template and component surfaces respectively. The roughness factor C_r, as in previous work [2-4], is then calculated using the relation:

$$C_r = 1 - \frac{1}{\sqrt{2\pi}} \int_{-\infty}^{(h_{eq.} - d_a)/\sigma_{eq.}} \exp\left(-\frac{1}{2}\left(\frac{z}{\sigma_{eq.}}\right)^2\right) d\left(\frac{z}{\sigma_{eq.}}\right) \quad , \quad (2.6)$$

where z is the height of the asperities on the surface above the reference plane z=0 and d_a is the adhesive distance as defined in previous section. This relation is derived using Gaussian probability distribution function [26] that calculates the fraction of points that are at a height greater than or equal to $(h_{eq.} - d_a)$ from the reference plane of the rough surface.

Using the value of the roughness factor for the particular combination of component and template material, we can now arrive at the value of the real contact area between interacting surfaces once we know the value of the nominal contact area using the following relation:

$$A' = C_r A_n \quad (2.7)$$

where A' is the value of the real fractional contact area, C_r is the roughness factor and A_n is the nominal fractional contact area.

2.1.5 Retention and removal moments

2.1.5.1 Calculation of retention moment

Following the analysis of Eid and Jung [2-4], mathematical approximations of retention and removal forces and moments acting on the system can be made. The retention force is directly proportional to the differential change in the free energy that takes place upon displacement of the sphere from its original location to a location where it has greater contact with the liquid. The change in this free energy in turn is directly related to the magnitude of lost contact area between sphere and hole. Incorporating also the effects of surface roughness, the magnitude of the retaining force which opposes removal of component from substrate is then given by the expression:

$$F_{retention} = -\gamma\left(C_r \frac{dA_n}{dz} + A_n \frac{dC_r}{dz}\right) \qquad (2.8)$$

where dz is the differential change in distance during the translation of sphere from one location to the other. As is seen from equation (2.8), the values of both the roughness factor, C_r, and nominal fractional contact area A_n , change when a component moves to another location, and this is taken into account by the expression for the retention force. The retention moment, on the other hand, is calculated using the value $d\Phi$, which is the differential change in the

rolling angle via rotation of the sphere. Retention moment is then calculated using the following equation:

$$M_{retention} = -\gamma C_r \frac{dA_n}{d\phi} \qquad (2.9)$$

The value of the right hand side in the above equation is calculated by making use of the differential chain rule and knowing that,

$$ds = Rd\phi \quad , \qquad (2.10)$$

where R is the radius of the particle and *ds* is the differential distance covered by the sphere during rolling by an angle *dΦ*. Since *ds* can be further expressed in terms of the differential increments along the x and y axis, *dx* and *dy*, and their values, along with the value of dA_n, are calculated in the form of finite differences from the contact area algorithm as described previously in section 2.1.3, the net value of the retention moment can be calculated numerically, using the expression:

$$M_{retention} = \gamma R C_r \left(\frac{-dA_n}{\sqrt{dx^2 + dy^2}} \right) \qquad (2.11)$$

2.1.5.2 Calculation of removal moment

The calculation of the net removal moments involves analytical expressions for several fluidic forces obtained from literature [27] for cases which resemble the situation under consideration.

As mentioned in previous work [2-4], there are two types of fluid forces in this system. The primary forces, which have dominant contribution to the removal moment are due to unsteady low Reynold's number flow past a sphere while the secondary forces are acoustic in nature. Solving the simplified Navier-Stokes equation that describes the system accurately [28], as shown in equation 2.12, the total hydrodynamic drag acting on the sphere is expressed as a result of three primary forces, the added mass force, the viscous drag force and the Basset force [29].

$$\rho \frac{\partial u}{\partial t} = -\nabla P + \mu \nabla^2 u \quad (2.12)$$

The added mass force is a result of the relative acceleration of the spherical component with respect to the fluid in the vicinity. The viscous drag force, equivalent to the Stokes drag, results from the shear stresses generated as a result of the velocity gradients between the surface of the sphere and the bulk fluid medium. The Basset force is a result of the varying-thickness boundary layer developed around the sphere due to change in its relative velocity with respect to the medium and accounts for deviations of the flow pattern from steady state. Lift and buoyant forces are negligible for the case under consideration here as was also observed in [2-4], which worked on similar situations.

Along with the primary forces that are generated due to the flow past a sphere, secondary forces are also generated from the megasonic flow field that is created within the assembly fluid by the megasonic transducer. The acoustic streaming drag is one such force that results from the loss of acoustic momentum due to attenuation of sound waves in the viscous fluid

medium [30]. Another effect of the sound field is the generation of the radiation pressure force which is exerted on the components due to scattering of the acoustic waves by them [31].

It was demonstrated after detailed calculations in previous work [2-4] that the net removal moment, $M_{removal}$, could be estimated effectively by the expression:

$$M_{removal} = M_{addedmass} + M_{radiation} + \sqrt{\left(\left(M_{viscous} + M_{Basset}\cos 45^{\circ}\right)^2 + \left(M_{addedmass} + M_{Basset}\sin 45^{\circ}\right)^2\right)} \quad (2.13)$$

where moments due to the Basset force, M_{Basset}, the radiation force , $M_{radiation}$, the viscous drag force, $M_{viscous}$ and the added mass force, $M_{addedmass}$ were each calculated separately using analytical expressions [27-34] to arrive at the final moment value. The expressions for each of these moments is listed in equations (2.14)-(2.17) below [4]

$$M_{addedmass} = \left(\frac{4}{3}\pi^2 f R_{component}^4 \sqrt{\left(\frac{I\rho}{c}\right)}\right)\sin\theta \quad (2.14)$$

$$M_{viscous} = 6\pi\mu R_{component}^2 \sqrt{\left(\frac{I}{\rho c}\right)}\sin\theta \quad (2.15)$$

$$M_{basset} = \sqrt{\left(\frac{72\pi^3 \mu I f}{c}\right)} R_{component}^3 \sin\theta \quad (2.16)$$

$$M_{radiation} = 64\rho\left(\frac{2\pi f}{c}\right)^4 R_{component}^7 U^2 \sin\theta \quad , \quad (2.17)$$

where f is the ultrasonic wave frequency, equal to 1.7 MHz in our case. The parameter c is the velocity of the waves created due to ultrasonic vibrations (that is the speed of sound in the

medium) and is related to the material properties of the elastic medium in which it is travelling, such as the Young's modulus E, Poisson's ratio v and the medium density ρ, through by the following relation [4]:

$$c = \sqrt{\frac{E}{3\rho(1-2\upsilon)}} \qquad (2.18)$$

U is the wave velocity amplitude given by [27]

$$U = \sqrt{\frac{I}{\rho c}} \quad , \qquad (2.19)$$

and I is the intensity of the incident acoustic wave at the given location, which is attenuated in the direction of travel and is defined by the relation [35]

$$I(a) = I_o e^{-\alpha a} \quad . \qquad (2.20)$$

I(a) is the intensity at a given location a in the direction of travel, I_o is the intensity at source position a=0 , and α is the attenuation coefficient of the travel medium. The parameter θ used for calculating these moments has been defined previously in section 2.1.2 for calculation of nominal fractional contact area during rolling of sphere inside the hole.

2.2 Introduction to TASR modeling for deformable systems

As discussed previously, Templated Assembly by Selective Removal (TASR) is essentially a competition between adhesive retention effects and fluidic removal effects in order to achieve selective self-assembly. Because both the retention and the removal moments increase with component size, TASR can be effective across scales. The component to be assembled is retained therefore in a well-matched site where the geometry of the component to be assembled matches the topography of the template. On the other hand, ultrasonically-generated removal forces will remove it from a site where it is not well-matched. Thus, the shape and size selectivity principle of TASR fundamentally depends on the component's shape. Since deformable structures can change their shape and size under the application of a load, the component/template contact area may depend on the degree of deformation. Therefore systems incorporating deformable components cannot be described completely by theoretical frameworks such as the original TASR model [2-4] that do not take into account the deformation of the components and/or substrate. To accommodate the possibility of deformation, a second model for TASR-based self assembly in deformable systems is hereby proposed. This model relies on the elastic-plastic contact theory of deformation to determine when the original TASR model is or is not valid. This model complements the original TASR model for rigid structures that was formulated by Jung[2] and Eid[3-4]. Details of the model are described in the following sections, starting with a classification of the cases that are currently relevant for study.

2.2.1 Classification of cases under consideration

The scope of potential experiments and applications for TASR encompasses both rigid and deformable materials, both for the components as well as for the assembly templates. Therefore, four major classifications arise from a combination of the above inputs. The first of these possible combinations, i.e. the assembly of rigid materials on rigid substrates using TASR has been already modeled and studied extensively in previous work [2-4]. This leaves three cases that are relevant for assessing the effect of deformation of either the component or the substrate on the assembly yield results:

1) How a deformable sphere interacts with a rigid substrate,

2) How a rigid sphere indents a deformable substrate, and

3) How a deformable sphere interacts with a deformable substrate.

At first glance, it might seem that a single model should accurately predict the contact theory for all of these cases once the variations in material properties for the various combinations have been incorporated. This is not the case, however, because the constraint conditions are quite different for the three cases, and these differences result in different deformations under load. The literature survey documents the differences between the first [41-42], second and third cases listed above. In the first case, the curvature of a deformable sphere changes continuously during the deformation, and the displaced material of the deformable sphere is free to expand radially outwards. However, in the case 2 of indentation, the exact opposite occurs, as the radius of the rigid spherical indenter remains constant while the displaced material in the indented half-space is confined by the rigid indenter and the elastic bulk of the half-space. This concept is shown with the help of an exaggerated schematic

in Figure 2.3, which illustrates conceptually the pronounced deformation in case 1 due to unconstrained boundary conditions as opposed to case 2 where the room for deformation is much less.

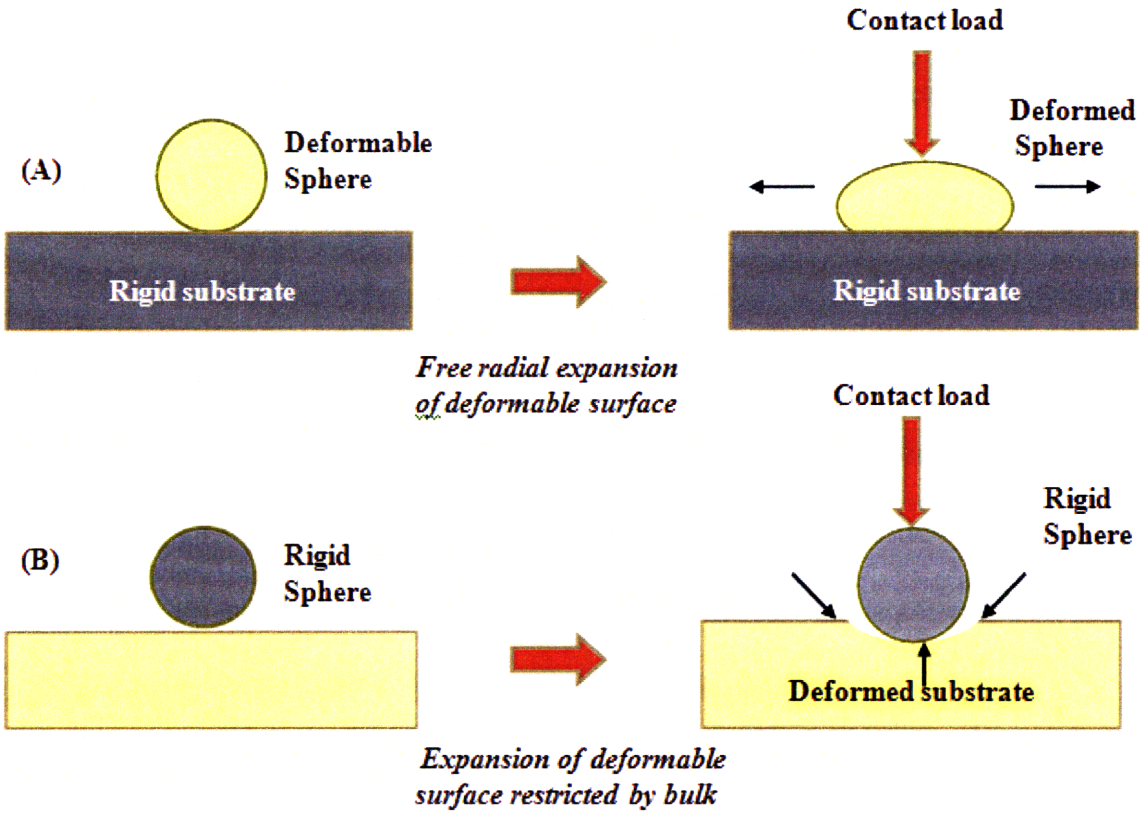

Figure 2.3: Schematic illustration of the difference in constraint conditions and degree of deformation in cases (A) A deformable sphere contacting a rigid substrate and (B) A rigid sphere indenting a deformable substrate under the application of load. The deformation is more pronounced in case (A) than (B) due to difference in constraining conditions.

The third case of a deformable sphere contacting a deformable substrate is more complicated than the first two cases as it involves a combination of two or more models depending on the materials under consideration. If the assembly is that of a deformable sphere whose mechanical behavior is similar to that of the substrate it is to be assembled onto (e.g. the assembly of polystyrene microspheres on a substrate such as PMMA), then the case can be

modeled on the lines of case 1 if the constraint conditions favor the deformation of the component. If, however, the behavior of the deformable component and the substrate is markedly different in terms of elasticity and mechanical properties, then this difference in behavior of the two materials also needs to be incorporated in the final model which simultaneously addresses the deformations of both the sphere and the substrate.

2.2.2 Discussion of elasticity

In order to better understand the above cases, a brief discussion of elasticity is also relevant. An elastic material, by definition, is a material which deforms under stress but returns to its original shape once the stress is removed. A plastic material, on the other hand, deforms permanently under the action of stress. An elastic–perfectly plastic material is one which, after its yield point, keeps on stretching infinitely without a further increase in stress beyond the yield stress point. This is in contrast to an elastic-strain hardening material which after the onset of yield still needs further application of load in order to continue to stretch. The difference in mechanical behavior of each of these types of materials can be seen clearly from stress-strain curves for each of these cases in Figure 2.4.

In the analysis that follows, the deformable material under consideration has been assumed in most of the cases to be *elastic-perfectly plastic* with identical behavior in tension and compression, which is a fairly reasonable approximation for most of the polymers under consideration such as polystyrene, polytetrafluoroethylene (PTFE), poly methyl methacrylate (PMMA), and melamine. The only exception to this phenomenon in the material set considered

for the current work is exhibited by rubber-like materials such as Polydimethylsiloxane (PDMS), which are deformable but show different mechanical properties depending on the set-up conditions.

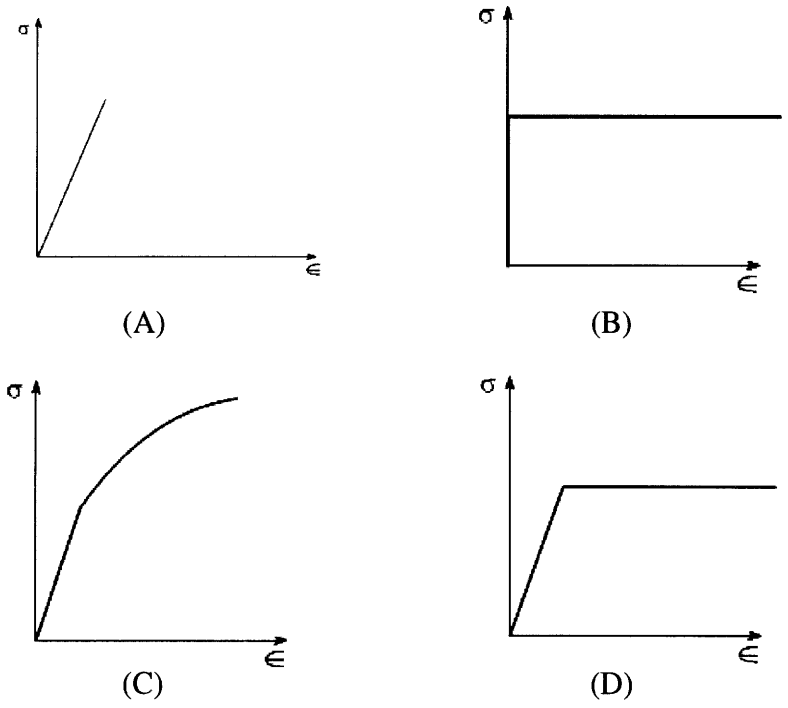

Figure 2.4: Stress-strain curves for (A) perfectly elastic material (B) perfectly plastic material (C) elastic-strain hardening material (D) elastic-perfectly plastic material. Most of the materials under consideration for TASR can be described by the elastic-perfectly plastic model.

For such materials, linear elastic models do not accurately describe the observed material behavior. Their stress-strain relationship can be defined as non-linearly elastic, isotropic, incompressible and generally independent of strain rate. Hyperelasticity provides a means of modeling the stress-strain behavior of some such materials. The behavior of vulcanized elastomers often conforms closely to the hyperelastic ideal. Elastomers and biological tissues are also often modeled via the hyperelastic idealization. While a linear elastic material has a

linear relationship between applied stress and strain, a viscoelastic material and a hyperelastic material do not. A hyperelastic material will initially be linear, but at a certain point, the stress-strain curve will plateau due to the release of energy as heat while straining the material. Then, at another point, the elastic modulus of the material will increase again. A *viscoelastic* material, on the other hand, is one that exhibits both viscous and elastic characteristics when undergoing deformation. Viscous materials resist shear flow, and they strain linearly with time when stress is applied. Elastic materials, on the other hand, strain instantaneously when stretched and just as quickly return to their original state on removal of stress. The stress-strain curve for a viscoelastic material, as seen from Figure 2.5, is very different from that of an elastic material. The red area shown in the figure is a hysteresis loop and shows the amount of energy lost (as heat) in a loading and unloading cycle. PDMS, in particular, shows the properties of a viscoelastic material at low temperatures and a hyperelastic material at high temperatures.

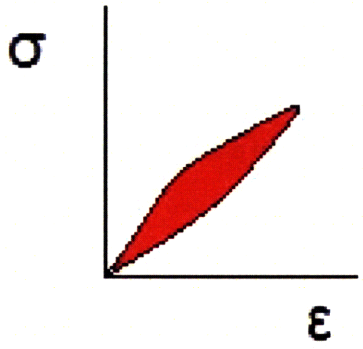

Figure 2.5: Stress-strain curve for a viscoelastic material. The shaded red area is a hysteresis loop which shows the amount of energy lost as heat in a loading and unloading cycle. Non-linear elastic behavior such as that shown here for certain materials might have to be considered for assessment of their applicability to TASR.

Materials such as PDMS are of great interest to us for incorporation in TASR systems since they are commonly available and can easily be molded and cured to replicate patterns, as will be

discussed in detail in Section 3.6. Therefore, special mechanical properties of rubber-like polymers such as PDMS might have to be considered for the accurate modeling of deformable systems created from them. Although a brief description of these effects follows, a detailed treatment of the effects of these properties is outside the scope of what will be presented here.

2.3 Predictive model for TASR

The extension to TASR theory proposed here takes into account the mechanical properties of the components and substrate and rests on a simple energy argument. Self assembly in general and TASR in particular depend on the tendency of systems to minimize their free energy. If the deformations of components and substrate are fully elastic, any reduction in system free energy due to the increase in contact area upon deformation will equal the increase in system free energy due to the storage of elastic energy in the deformed structures. Therefore, for purely elastic deformations, the original TASR model should still apply. In contrast, if the deformation enters the plastic regime, some of the energy will be dissipated, and the TASR model should no longer apply completely. Therefore, the ability to assemble deformable systems (with deformable components and/or substrate templates) comes down to the question of at what point the deformations enter the plastic regime. This in turn depends on a) the mechanical properties of the component and substrate materials, b) the magnitude of the force that holds the component on the substrate, and c) whether the component, the substrate, or both are deformable, as described above.

Although the same concept (the significance of the onset of plastic deformation) applies independent of whether it is the substrate, the components, or both that are deformable, the details of when plastic deformation sets in depend on which elements are deformable. The case of deformable spherical components assembling on an essentially rigid substrate will be considered first. Cases of rigid components indenting deformable substrates are discussed in section 2.5.3 and deformable spherical components assembling on deformable substrates with comparable mechanical elastic behavior are described later in Section 2.5.4.

2.4 Hertzian theory of contact

Hertzian elastic contact theory [41], combined with prior analytical and numerical assessments of the onset of plastic deformation [42-45], is used to assess whether the component deformation is purely elastic or includes a plastic component. The theory that is employed here to describe deformation is strictly applicable either to two deformable spheres in elastic contact, a deformable sphere in elastic contact with a rigid flat, or to a deformable sphere in elastic contact with a rigid sphere. It may also be approximately applied to the present situation of a deformable sphere inside a hole with a local (but not quite constant) radius of curvature. For assessing the applicability of the TASR process to a given materials system, the parameter of interest is the value of the critical interference ω_c that marks the transition from the purely elastic to the elastic-plastic deformation regime. Interference is a measure of the sphere's deformation and is equal to the difference between the sphere's radius and the distance from the center of the deformed sphere to the surface that it contacts. In other words, it is the amount by which the sphere would have had to penetrate into the

second surface in order to approach it that closely in the absence of deformation. For values of the interference below the critical interference, the deformation is purely elastic and the original TASR theory is predicted to apply. For values of the interference above this value, the TASR theory is no longer entirely applicable.

The Hertzian closed-form expressions for the mechanics of two deformable spheres in purely elastic contact [41-44] can be used to determine the interference for a single elastic sphere in contact with a flat substrate (or indeed for a sphere in contact with a substrate with a given radius of curvature). Figure 2.6 depicts schematically such a case of a deformable sphere pressed by a rigid flat. On pressing a deformable sphere of radius R by application of a contact load P onto a rigid flat, a circular contact between the sphere and the flat is achieved which is described by a contact radius, a. An interference depth ω characterizes the deformation of the sphere due to the contact load applied by the rigid surface.

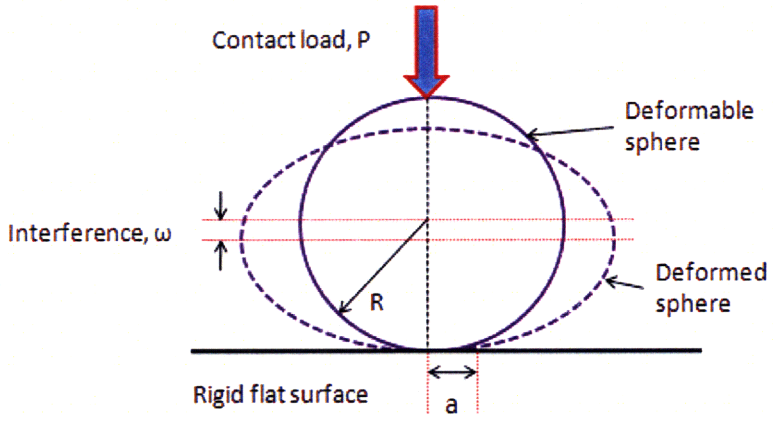

Figure 2.6: Schematic description of deformable sphere of radius R pressed by a rigid flat due to application of contact load P. An interference ω is obtained upon the contact, with a circular contact region of radius a.

The interference ω is given in the elastic regime by

$$\omega = \left(\frac{\pi \cdot p_{\max}}{2E'} \right)^2 R_{eq}, \qquad (2.21)$$

where the equivalent radius R_{eq} is given in terms of the component radius R_c and the template's local radius of curvature R_t by

$$\frac{1}{R_{eq}} = \frac{1}{R_c} + \frac{1}{R_t}, \qquad (2.22)$$

and the combined modulus E' is given in terms of the respective Young's moduli E_c and E_t and Poisson's ratios υ_c and υ_t of the components and template by

$$\frac{1}{E'} = \frac{\left(1-\upsilon_c^2\right)}{E_c} + \frac{\left(1-\upsilon_t^2\right)}{E_t}. \qquad (2.23)$$

The term $p_{\max}$ is the maximum value of the contact pressure at the component/template contact.

The contact pressure arises from the net force that presses the component into the substrate template. This force is almost entirely chemical in origin and is determined from the original TASR models [2-4]. If the contact between component and substrate template is approximated as a contact between two spherical surfaces, then the pressure may be taken to vary spatially as $\sqrt{1-r^2/a^2}$, where r is the radial distance out from the central contact point and a is the overall radius of the contact area. Within this approximation, the maximum value of the contact pressure $p_{\max}$ is simply related to the average contact pressure p_{avg} as

$$p_{\max} = \frac{3}{2} p_{avg} = \frac{3}{2} \frac{P}{A}, \qquad (2.24)$$

where the average pressure is the ratio of net force to contact area. According to Hertzian theory [41], the contact area between two elastic solids with spherical contact surfaces is given by

$$A = \pi a^2 = \pi \left(\frac{3R_{eq}P}{4E'} \right)^{2/3}. \qquad (2.25)$$

Combining these results yields the value of the interference for the physical situation; this value is valid until the onset of plastic deformation but becomes invalid beyond it. The interference ω is then compared with the critical interference value ω_c that marks the onset of plastic deformation. The critical interference has been calculated previously [45] to be

$$\omega_c = \left(\frac{\pi KH}{2E'} \right)^2 R_{eq}, \qquad (2.26)$$

where H is the hardness of the component and is related to its yield strength Y as

$$H = 2.8Y. \qquad (2.27)$$

In Eq. 2.26, K refers to the hardness coefficient of the spherical component. The value of K was found in [46] by modeling based on finite element results. Their resulting values depend on Poisson's ratio and are given by

$$K = 0.454 + 0.41\nu_c. \qquad (2.28)$$

Using these results, the ratio ω/ω_c of the interference to the critical interference may be calculated for various component and substrate materials, and for various geometries (radii of

curvature of spherical components and the template holes in which they assemble). If ω/ω_c is less than one, the original TASR model is predicted to be applicable, and the assembly is expected to be successful. If the calculated ratio exceeds one, then the TASR model will have begun to become invalid (though the discrepancy between the model and reality may be small for very small amounts of plastic deformation). In addition, for ratios above one, it is known that the interference exceeds the critical interference, but not by how much, because this interference calculation is only strictly valid in the purely elastic regime.

2.5 Model results and analysis

As gathered from the above equations which are the basis of this analysis, some of the material parameters that are necessary input values in the model for predicting the self-assembly of a soft sphere material on a hard substrate include Poisson's ratio, Young's modulus, yield strength, and diameter of the component to be assembled. The above properties for some of the common materials considered for the purposes of our modeling and experiments are listed in Table 2.1 below.

Table 2.1: Material Properties of common materials considered for analysis [38]

Material	Young's modulus, E (Gpa)	*Poisson's Ratio, υ*	Yield Strength, Y (Gpa)	Hardness, H(Gpa)
Polystyrene	2.55	0.38	0.012	0.032
PMMA	2.8	0.38	0.05	0.14
PTFE (Teflon)	0.5	0.31	0.015	0.042
Polypropylene	1.5-2	0.35	0.05	0.14
Melamine	11	0.31	0.085	0.238
PDMS	0.0005	0.4	0.007	0.0196
Silica	94	0.17	0.05	0.14
Silicon	150	0.27	7	19.6
Aluminum	70	0.33	0.4	1.12

2.5.1 Theoretical results for assembly of deformable microspherical components on rigid substrates

2.5.1.1 Assembly of microspherical component on a flat substrate

The ω/ω_c ratios for some typical material combinations for the case of a 2 micron diameter deformable sphere assembling on a flat, relatively rigid surface of silica are given in Table 2.2. This particular value of diameter for deformable assembly components was chosen in order to enable experimental verification of the model predictions since commonly available microspheres of different polymers are in this dimension range. For larger diameter, ω/ω_c will be less than is shown here; for smaller diameter, the ratio will increase, although slightly, as shown in Figure 2.7 for the case of polystyrene.

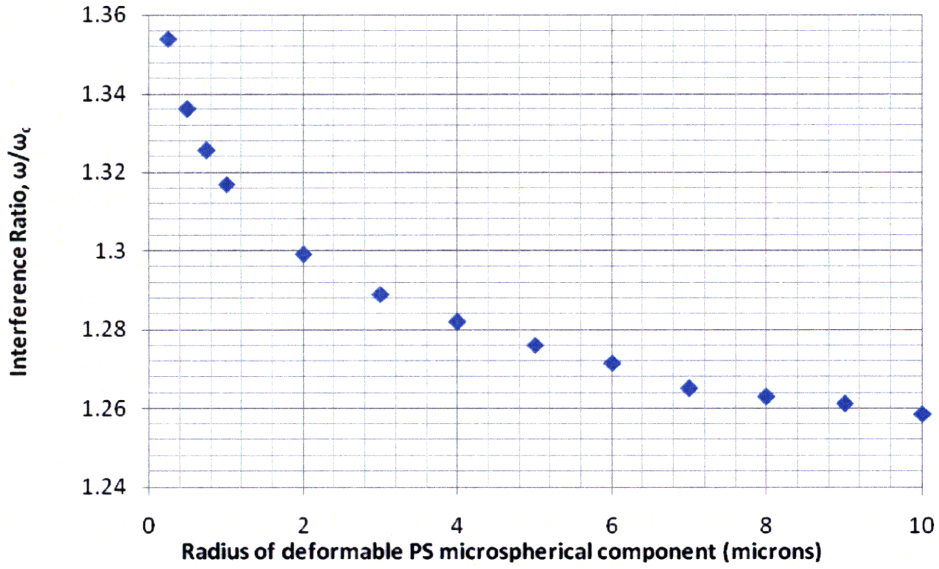

Figure 2.7: Predicted interference ratio ω/ω_c plotted vs radius of curvature for a deformable polystyrene microsphere being pressed on a flat silica surface by a contact load. In general, as the radius of component increases, ω/ω_c decreases. The results are obtained from the theoretical model for deformable systems in TASR.

It is to be noted that the values of the contact load used for obtaining these and subsequent interference ratio values are the values of retaining adhesive force for the case of a sphere inside a hole with partially matching geometry and not that for the case of a sphere contacting a flat surface. This ensures consistency with the model results obtained in section 2.5.1.2 for the case of a substrate with a finite radius of curvature, which form an important section of the theoretical analysis for the purpose of experimental validation. Although this might cause a certain variation in the numerical values of the ratios presented here, all of the trends that are concluded from this theoretical analysis will stay unchanged. For the examples described in Table 2.2, the template material is taken to be silicon dioxide for consistency with the experiments presented in Chapter 3. Silicon and silicon dioxide are commonly used materials in semiconductor fabrication processes because of the diversity of patterns that can be created in them.

Table 2.2: Model results for different material combinations describing the case of a 2 micron diameter deformable microspherical component made of commonly available polymers contacting a relatively rigid substrate which is assumed to be made of silica

Component material	**Template material**	ω/ω_c
PTFE (Teflon)	Silicon dioxide	0.090
PMMA	Silicon dioxide	0.079
Polystyrene	Silicon dioxide	1.3
Polypropylene	Silicon dioxide	0.051
Melamine	Silicon dioxide	0.155
PDMS	Silicon dioxide	3.74E-05

As can be seen from Table 2.2, the ratios ω/ω_c are well below the critical ratio of one for Polytetrafluoroethylene (PTFE), Poly-methylmethacrylate (PMMA) and Polypropylene components on the flat, relatively hard template substrate. The ratio for melamine, although less than one, is higher than the previous three cases. Extremely low values of ω/ω_c for PDMS interacting with silica reflect the extreme elastic deformability of PDMS. However, more interestingly, the ratio is somewhat higher than one for polystyrene components on a flat relatively hard substrate, indicating that whether TASR can operate successfully and be well-described by the original model will depend strongly on the details of a given situation. It is also important to note that the model described here takes into account only overall deformation of the sphere and not local deformations due to surface roughness, which will be discussed in greater detail in Section 4.10.

2.5.1.2 Assembly of microspherical components on a substrate with a finite radius of curvature

In the previous section, deformations in components assembling on flat substrates were considered. However, the model results will be different for different geometries of the substrate, since a finite radius of curvature R_t on the template surface will change the equivalent radius of curvature of the system, R_{eq}, as seen from equation 2.22. An important case to be addressed in context of TASR, which works on shape and size matching between the component and the assembly site on the template, is that of a sphere that is resting inside a hole on the substrate surface. In this case, the radius of curvature R_t of the assembly sites is

negative, leading to a much larger equivalent radius for the sphere-hole contact than for a sphere-flat contact.

As seen from Table 2.2, the value of ω/ω_c was slightly above one for the case of a PS microsphere 2 micron in diameter assembling on a flat silica substrate. Therefore, the case of a PS microsphere assembling on a silica substrate with a finite radius of curvature is now considered here to determine the effect of the geometry of the template on the ratio value ω/ω_c and accordingly, the nature of contact (elastic/elastic-plastic) at the interface. Table 2.3 shows the values of the interference ratio ω/ω_c for the case of a PS microsphere 2 microns in diameter assembling inside holes with diameters of 2.05 μm, 2.1 μm, 2.2 μm, and 2.5 μm on a silica substrate. These particular diameters were chosen as they represent the actual hole sizes on the silica templates used in the current work, which is explained in greater detail in Section 3.2 that describes template fabrication. As seen from the table, a larger equivalent radius of curvature R_{eq} decreases the ω/ω_c ratio for deformable spheres in holes as compared with deformable spheres on flat surfaces.

Table 2.3: Theoretical model results for the polystyrene-silica assembly combination, taking into consideration the hole geometry for different starting hole sizes.

Radius of hole on template, R_t (microns)	**Equivalent radius, R_{eq} (microns)**	**Interference Ratio, ω/ω_c**
1.025	41	**0.0089**
1.050	21	**0.0219**
1.100	11	**0.0522**
1.250	5	**0.1502**

The largest value of ω/ω_c for the polystyrene spheres in the holes is about 0.15, corresponding to the largest holes. This value in this case, therefore, is significantly below the critical value of one which marks the onset of plastic deformation in the system, in contrast with the case of a PS microsphere assembling on flat substrates where the value slightly exceeded one. Hence, TASR enabled assembly is predicted to be successful for the cases as are listed in Table 2.3, in terms of being able to achieve a completely elastic contact at the interface between the component and the substrate. Physically, in assembly of a microsphere inside a hole, there is less room for the extreme deformations that would lead the sphere to enter the plastic deformation regime. Figure 2.8 shows a schematic description of this concept.

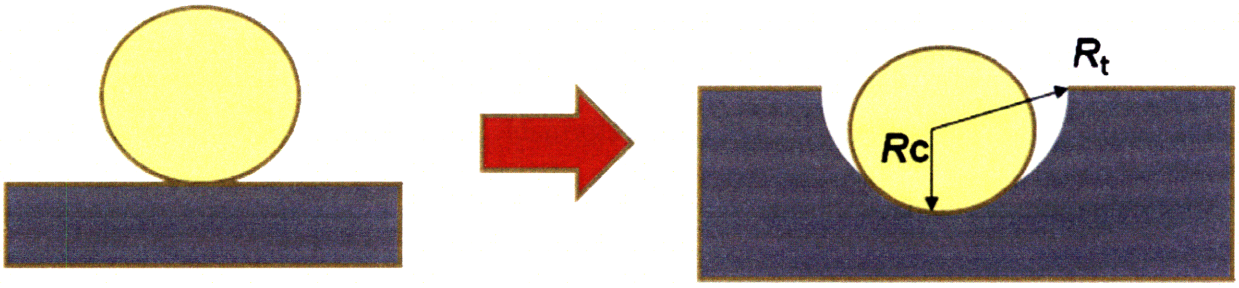

Figure 2.8: Schematic illustration showing lesser room for deformation in case where assembly site has a radius of curvature R_t (negative) for the assembly of a spherical component (with a positive radius of curvature R_c) as opposed to a case of deformation of a sphere on flat (with infinite radius of curvature).

2.5.2 Method for verification of model results

Upon calculation of the values of the ratio ω/ω_c for a combination of materials, we can compare the values of the *actual contact area* and the *contact load* calculated previously in equations (2.24) and (2.25) in order to obtain the ratio ω/ω_c, with the *critical values of the contact load and contact area* to double check that the system is indeed below the onset of plastic deformation according to these metrics for cases where the ratio is calculated to be less than 1. This is done using the value of the contact area, A_E and the contact load, P_E for the elastic contact as defined by the Hertzian contact theory:

$$A_E = \pi R \omega \qquad (2.29)$$

$$P_E = \frac{4}{3} E' \sqrt{R} (\omega)^{\frac{3}{2}} \qquad (2.30)$$

By replacing the values of interference in equations (2.29) and (2.30) above with the value of critical interference calculated using equation (2.26), the critical values of contact load and contact area for a deformable sphere on a rigid flat can be obtained. On comparison of these values to the actual values of the load and contact area calculated using equations (2.24) and (2.25) previously, we can reaffirm the model results. Table 2.4 presents model results calculated using the approach highlighted above for the same combinations of assembly components on a silica template as were considered for our analysis using the model, the results of which were tabulated previously in Table 2.2.

Table 2.4: Comparison of actual contact load and contact area for assembly combinations in comparison with critical values for transition from elastic to plastic regime

Component Material (Material 1)	Substrate Material (Material 2)	Contact Area from Hertzian Theory A (meter^2)	Contact load P (N)	Critical Contact Area A_c (meter^2)	Critical Contact Load P_c (N)
PTFE (Teflon)	Silica	1.4E-15	4.05E-09	1.5E-14	2.52E-07
PMMA	Silica	4.4E-16	4.05E-09	5.63E-15	3.12E-07
Polystyrene	Silica	3.63E-16	4.05E-09	3.69E-16	4.53E-09
Polypropylene	Silica	5.57E-16	4.05E-09	1.09E-14	5.94E-07
Melamine	Silica	1.96E-16	4.05E-09	1.26E-15	1.14E-07
PDMS	Silica	1.27E-13	4.05E-09	3.39E-9	2.75E-02

Table 2.4 reaffirms the results obtained from Table 2.2 previously that for most of the polymer combinations with silica templates considered for TASR in deformable systems, the interaction is indeed elastic. This is demonstrated by the fact that for most of the polymers, the values of the contact load and the contact area are below the critical contact load and critical contact area that mark the transition from elastic to plastic deformation. However, the values of contact load and contact area for polystyrene are very close to that of the critical values. This suggests once again that some portion of the contact in this case might be a result of plastic deformation.

2.5.3 Model extension to assembly of rigid microspherical components on deformable substrates

The case of rigid/deformable microspherical components assembling on deformable substrates is also of interest to us as mentioned in section 2.1.2 since the possibility of creating deformable, replicatable templates from rigid template masters would reduce the total fabrication cost involved and holds potential for mass production of templates without much difficulty. Therefore, analyzing these cases theoretically is of significance. This section highlights the approach for assessing deformations in deformable substrates when indented by microspheres made of a relatively rigid material.

As stated before, a deformable sphere contacting a rigid substrate is different from a rigid sphere contacting a deformable substrate because different constraint conditions lead to different behavior. Therefore, in order to address the case of the indentation of a deformable substrate by a rigid microsphere, a different parameter must be used to decide the nature of the contact between the two mating surfaces. Although the constraint conditions are different, the underlying concept of the transition from the elastic to the elastic-plastic regime remains the same.

Based on the case of Brinnel indentation of an elastic-plastic half-space considered by Mesarovic et al.[44], this parameter of interest describing the nature of deformation in the substrate was found to be γ, defined as:

$$\gamma = \frac{E' a}{R_{eq} \sigma_o} \qquad (2.31)$$

which is basically the ratio of the indentation pressure ($E'a/ R_{eq}$) and the initial yield strength σ_o of the half-space, or in this case the assembly substrate. Here R_{eq}, E' and a are the same parameters as used and described previously in equations (2.22), (2.23) and (2.25) respectively. From finite element predictions [44] of average indentation pressure, the completely elastic Hertzian regime extends for values of ($E'a/ \sigma_o R_{eq}$) less than 2.5. Above this value, plastic deformation in the substrate begins.

We have, until now, described the mechanical behavior of most polymers using the elastic-perfectly plastic model. The elastic-plastic model is valid for polymers such as PMMA, which is a common choice for creating replicates from master patterns made of silicon/silica by techniques such as nanoimprint lithography. It can also accurately describe the behavior of polymers such as polystyrene, as discussed before. However, polystyrene is not a commonly used substrate material and although it is briefly discussed here from a theoretical point of view, it is not of much interest for experimental purposes.

Using the above criterion, the theoretical model for deformable systems in TASR can be extended to assess the nature of the deformations for the case of rigid microspherical components contacting elastic-perfectly plastic, deformable substrates. For the case of a silica microsphere of radius 1 micron indenting a flat PMMA substrate, the value of the ratio γ using equation (2.31) is calculated to be 0.75, and the contact is determined to be purely elastic. On substrates of polystyrene, on the other hand, the value of γ is 3.05 for the same silica microsphere radius of 1 micron and therefore some amount of shape change due to plastic deformation might occur leading to at best a marginally successful assembly. Figure 2.9 shows and compares the trends for variation in the value of γ with increase in radius of curvature of

the rigid silica micro-spherical component for indentation of PS and PMMA substrates. As seen from the figure, for both the cases, the general trend is the same, i.e. as the radius of the component increases, the value of γ decreases very slightly, remaining almost constant. However, values of γ at the same radius of curvature are lower in all cases on a PMMA substrate than on one made of PS. This shows that for the same contact load, the PMMA substrate will have less chances of plastic deformation at the same component radius value as compared to PS.

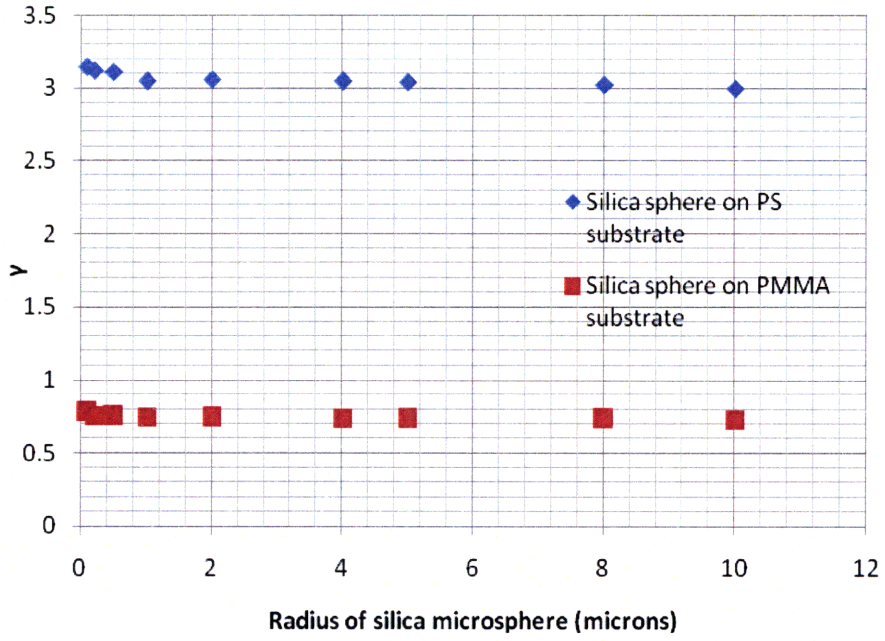

Figure 2.9: Ratio of indentation pressure to yield strength of substrate, γ plotted vs. radius of curvature for a rigid silica microsphere indenting flat, deformable PS and PMMA surfaces. In general, as the radius of component increases, γ decreases very slightly, remaining almost constant. The results are obtained from the theoretical model for deformable systems in TASR.

2.5.4 Model extension to assembly of deformable microspherical components on deformable substrates

The Hertzian theory extension used so far for describing the contact between a deformable solid and a relatively rigid solid originates from the theory of contact between two deformable solids with similar mechanical behavior. By combining these concepts of Hertzian theory with the criterion for onset of plastic deformation in a deformable substrate when indented by a rigid material, the theoretical model can now be extended to assess the deformations during the assembly of a deformable microspherical component on an elastic-perfectly plastic, deformable substrate such as one made of PMMA.

Before applying the same principle used until now to assess the possibility of plastic deformation in polymeric microspheres when assembled on deformable substrates such as PMMA, we need to investigate the possibility of the onset of plastic deformation in the deformable substrate material itself. In the previous section, the case of a microsphere, made of a relatively rigid material such as silica, indenting the deformable PMMA substrate was considered. Based on estimates made from previous finite element model results [44], the possibility of incurring plastic deformation in a deformable substrate made of PMMA at or above the micron size scale was eliminated. If the substrate does not deform plastically on contact with a more rigid material, then it may safely be assumed to have elastic behavior on contact with materials that are more deformable than it is under otherwise similar circumstances. The focus of the analysis then shifts to the possibility of deformation in the polystyrene sphere rather than in the PMMA substrate. Using the same model as before, the

same concept of a deformable sphere contacting a relatively rigid flat may now be extended to estimate the possibility of plastic deformation in deformable spheres made of different materials on a flat, relatively rigid PMMA substrate. The results of the model in terms of the ratio ω/ω_c are recorded in Table 2.5.

Table 2.5: Calculated values of the interference to critical interference ratio for different material combinations describing the case of a deformable microspherical component, made of commonly available polymers contacting a replicatable deformable substrate, made of PMMA for a component diameter of 2 microns

Component material	Template material	ω/ω_c
PTFE (Teflon)	PMMA	0.073
PMMA	PMMA	0.032
Polystyrene	PMMA	0.5675
Polypropylene	PMMA	0.026
Melamine	PMMA	0.022
PDMS	PMMA	3.74E-05

The model results in Table 2.5 again show the different behavior of Polystyrene as compared with other polymers. Although the value of the ratio of interest ω/ω_c is lower than one in this case, it is still much higher than the ratio for the other materials. The results from Table 2.5, when compared with results in Table 2.2, show that values of ω/ω_c obtained for the cases of deformable components assembling on relatively softer substrates such as PMMA are less than the values obtained for assembly of deformable components on hard substrates such as silica. This suggests that deformable components might be assembled more easily on softer substrates than hard substrates because the components will deform to a lesser degree.

2.5.5 Selected experimental study based on model results

In order to compare with the model results obtained in the previous sections, the assembly of deformable microspheres on patterned relatively rigid substrates using TASR will now be considered experimentally. As the model results showed, the assembly of Polystyrene (PS) microspheres on silica templates was found to be the most interesting situation for experimental verification due to the relatively high predicted values of ω/ω_c for PS as compared with other polymers. Chapter 3 describes in detail the procedure to be followed in order to create patterned silica substrates, prepare the template and PS components for the subsequent assembly process, and finally carry out the assembly procedure itself with PS components on a silica substrate. In order to analyze the difference in assembly behavior of *rigid components* with the assembly of *deformable components* on relatively rigid substrates, a comparison of PS assembly on silica templates with silica assembly on silica templates is also described. Finally, in order to demonstrate the idea of replicating templates by the use of a low-cost patterning method, the procedure to be followed for creating PDMS replicas from silica templates is also tabulated. This may be a subject for future experimental and theoretical study.

Chapter 3

Experimental Work

3.1 Outline of experiments

The assembly set-up for TASR is described in detail in this chapter. Experimental protocols include the creation and functionalization of the templates on which assembly is to be carried out, the functionalization of the components that are to be assembled (when necessary), and the actual assembly experiments themselves. The template created is a silicon die with a patterned layer of oxide on top onto which the components can assemble. Electron beam-lithography and isotropic etching are used to pattern the silicon dioxide layer with hemispherical holes. These holes serve as matching sites for the assembly of polystyrene microspheres 2 microns in diameter. The template is then functionalized in order to make it hydrophobic. The microspheres are prepared for assembly by suspending them in an appropriate solvent and treating them to separate any clusters of components into individual microspheres. The prepared components and assembly template are then placed in the assembly beaker in a water/solvent mixture which is subjected to acoustic excitation at a megahertz-scale frequency. The excitation of the fluid mixture promotes selective removal of components from incorrectly matched sites on the template along with ensuring circulation of components in the fluid. By also controlling the number of components in the fluidic medium so as so to ensure enough hits between the component and the template, the components are

assembled in matching sites. The relevant procedures are covered in detail in the following sections.

3.2 Template fabrication

The templates for all of the experiments presented here comprise silicon dies coated with a layer of silicon dioxide into which the template holes (that is, the assembly sites) are etched. It is to be noted that the templates used for the experiments discussed here have been fabricated by Amelia Servi, who was a collaborator on the current work as a part of her UROP project.

Fabrication of the patterned silicon template follows an approach that is nearly identical to the ones described in [2-4]. An oxidized silicon wafer is coated with polymethylmethacrylate (PMMA). In order to pattern hemispherical holes in the template, e-beam lithography is first used to expose various arrays of small spots in the PMMA resist layer with spot sizes ranging from 45 nm to 500 nm. Pattern development produces corresponding openings in the resist layer. The underlying oxide is then etched isotropically with buffered oxide etch (BOE) to produce the near hemispherical isotropic holes required for the assembly of microspheres. A schematic of the fabrication process to be carried out is depicted in Figure 3.1, and the details are described below.

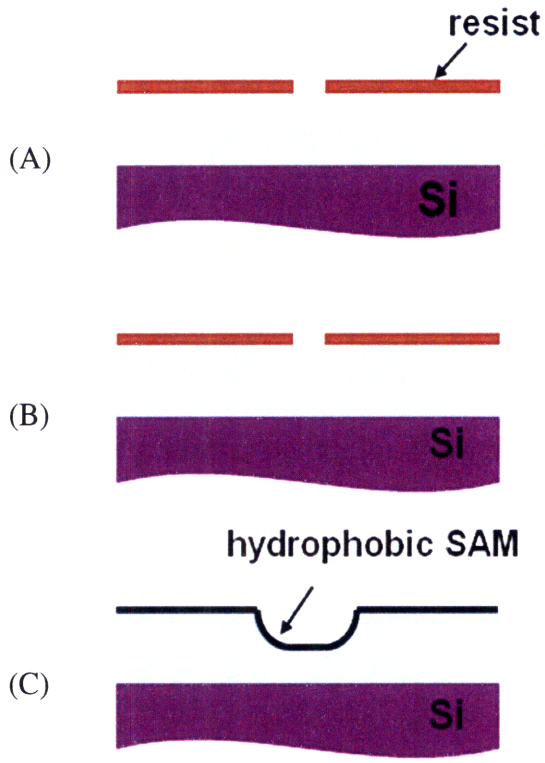

Figure 3.1: Schematic illustration of sequence for fabrication of assembly template. (A) Small patterns are exposed in oxidized Si wafer covered with resist using e-beam lithography. (B) Exposed spot are etched isotropically using BOE in order to produce desired hemispherical sites for component matching. (C) Template is covered with SAM to make it hydrophobic.

The fabrication procedure for the templates starts with a blank 6" silicon wafer. An RCA clean is carried out in preparation for the growth of thermal oxide on the wafer. An oxide layer of approximate thickness 1.8 microns is deposited onto the silicon wafer using a recipe which is carried out in 3 iterations, of 200 minutes each at 1050°C. The oxidized silicon wafer is then covered with PMMA, which acts as a positive resist for e-beam lithography, which allows for extremely high resolution (nanoscale) patterns to be defined. HMDS (hexamethyldisilazane) is deposited onto the wafer, which is then prebaked for 5 min at 220°C and thereafter cooled for 5 min. Subsequently, 950K PMMA (C10 Microchem) and chlorobenzene (ACS, 99.5% Alfa Aesar) are mixed in a ratio of 6:19 by volume to achieve a final PMMA concentration of 2.4% in the

mixture. This mixture is spun onto the wafer using a spin program of 500 rpm for 5 seconds and 3000 rpm for 90 seconds resulting in a resist layer 140 nm thick. The coated wafer is then post-baked for 15 minutes at 220°C.

In order to pattern hemispherical holes in the template, electron beam (e-beam) lithography is used to expose small spots in the PMMA resist layer, with spot sizes ranging from 45 nm to 500 nm. The CAD layout for the single die pattern used for our templates is shown in Figure 3.2.

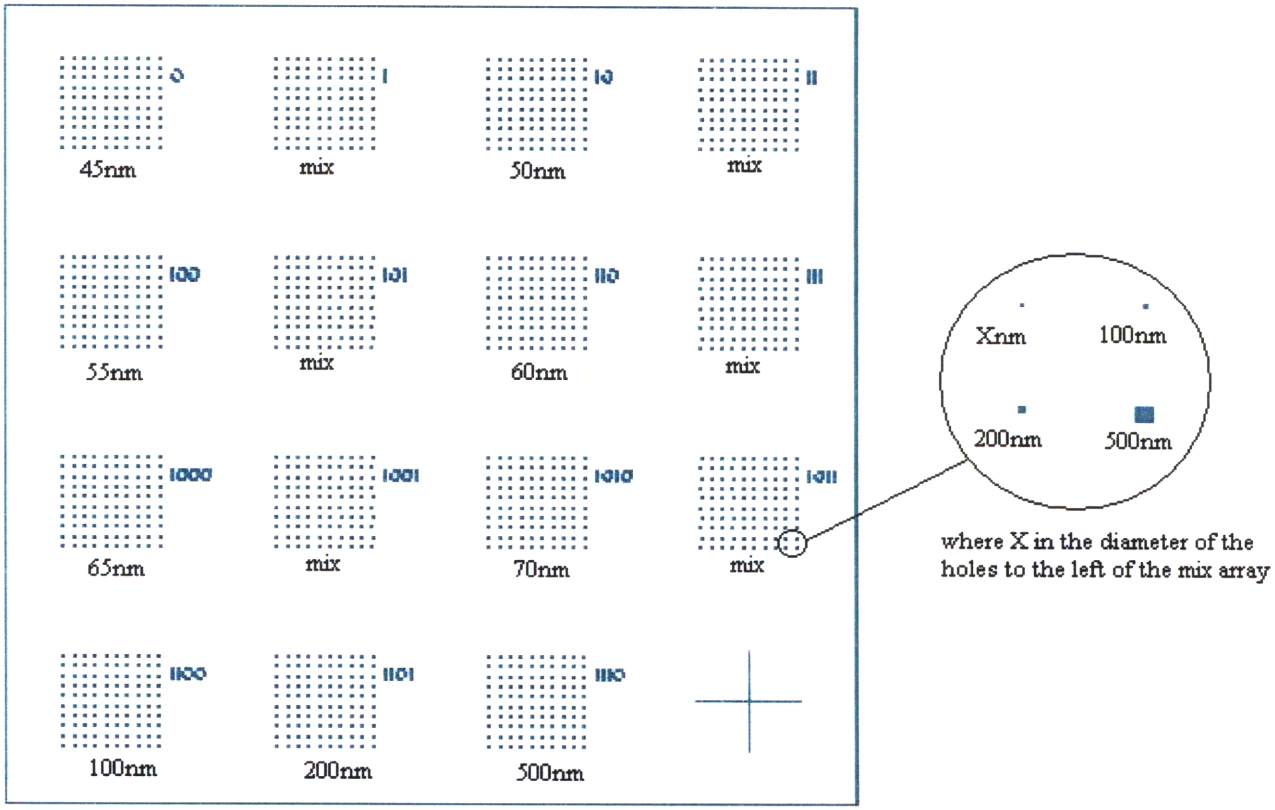

Figure 3.2: CAD layout of mask pattern used for fabrication of templated surface by electron-beam lithography. The numbers below each of the 15 grids shows the starting spot size used for that grid of spots on the e-beam tool (Courtesy of Amelia Servi)

The e-beam tool exposes spots in the resist according to the CAD pattern. There are 15 arrays of spots in the pattern, including arrays with resist exposure sizes of 45, 50, 55, 60, 65, 70, 100, 200 and 500 nm. This pattern, as created by Amelia Servi, is written with a beam of aperture 30 μm, a power of 10 keV, a step size of 10 nm and a dose of 120 μAs/cm^2. After the writing process is complete, the resist is developed in a solution of 1:2 MIBK/IPA at 25°C for 90 seconds to form the desired openings in the resist pattern. This is followed by methanol, isopropanol, and water rinses and then by a Buffered Oxide Etch (BOE) to produce isotropic holes of the required dimension. The BOE etch, which consists of a 7:1 solution of 40% NH4F: 49% HF, is carried out for 11 minutes with degas applied at the highest power for 5 out of every 30 seconds. The template is subsequently rinsed with water and dried with nitrogen. The resulting pattern on the substrate is 1 micron deep, quasi-hemispherical holes. In order to remove the resist over the patterned oxide layer, the wafer is subjected to a piranha clean comprising a solution that is 3 parts sulfuric acid and 1 part hydrogen peroxide. Finally, the resist is stripped and the wafer is diesawed (Disco abrasive system Model DAD-2H/6T) to produce 5 mm x 5 mm assembly templates, each containing several arrays of 1 micron deep quasi-hemispherical holes that match (to varying degrees) the 2 micron diameter polystyrene microspheres to be assembled into them.

Atomic force microscopy (AFM) is used to determine the as-fabricated profiles of the assembly sites. A tapping mode atomic force microscope (AFM D3000 by Veeco Instruments) is used for this purpose, and the profiling is done using a silicon nitride cantilever probe that scans the surface of the template (in the x and y directions). To lowest order, the isotropic etch produces hemispherical holes with hole radius approximately equal to the etch depth. Careful

attention to resist adhesion and etch procedures, along with small starting openings in the resist, enable an excellent approximation to the ideal hemispherical shape. The finite initial spot size results in etched holes that deviate slightly from the ideal hemispherical shape; the larger the initial spot size, the larger the deviation. Therefore, the holes with a smaller initial spot size will be a better fit for the spherical components, while the holes with a larger initial spot size will be a worse fit. Figure 3.3 shows AFM images of four quasi-hemispherical holes, each etched from a different size starting hole in the resist.

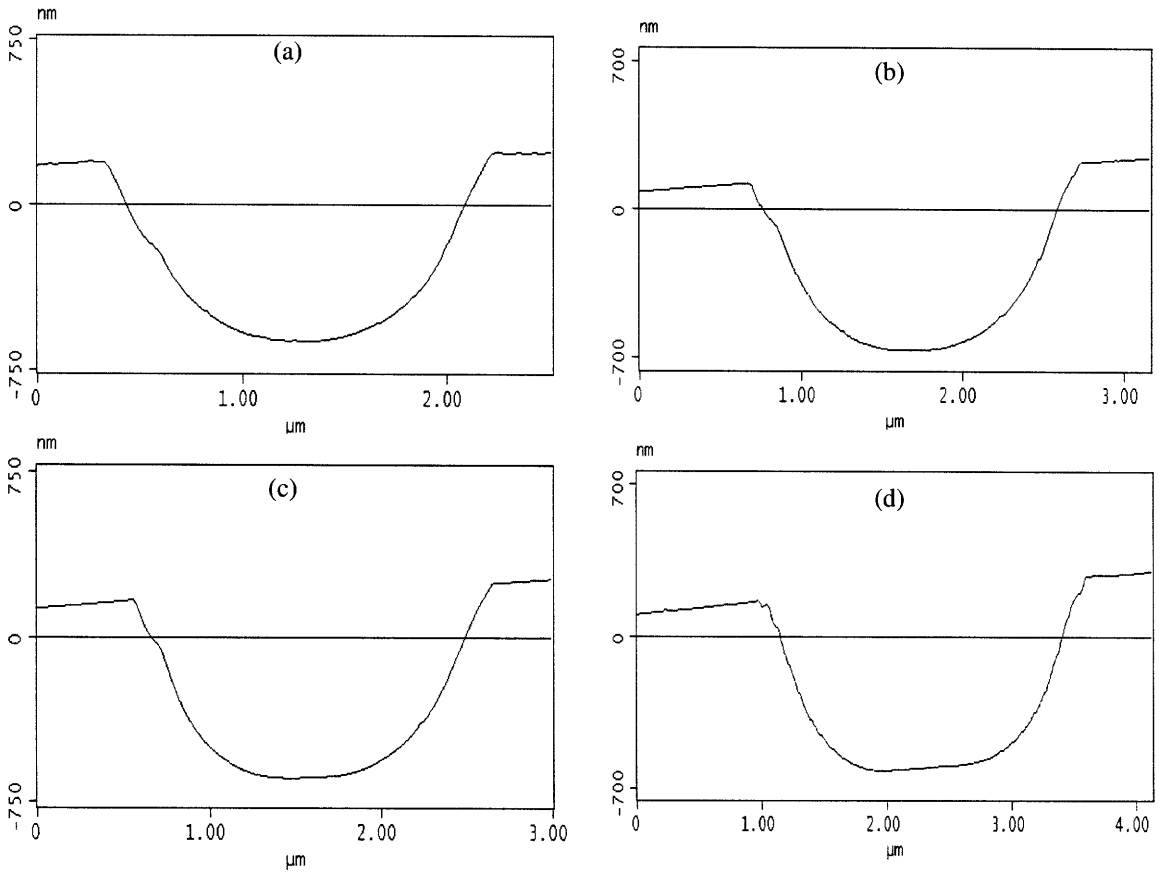

Figure 3.3: Atomic Force Microscopy (AFM) images of holes with starting spot sizes (from (a)-(d)) of 50, 100, 200, and 500 nm. Smaller starting hole sizes correspond to better shape matching with spherical components and therefore higher anticipated assembly yield (Courtesy of Amelia Servi)

3.3 Template and component preparation

Both polystyrene microspheres and silica microspheres were assembled on TASR assembly templates in this work for comparison. The experimental protocols for the two types of spheres differ only slightly, and are based on the experimental procedure described in [2-4]. The primary difference between polystyrene assembly and silica assembly lies in the preparation of the components for assembly. An outline of the experimental protocol follows.

3.3.1 Template functionalization

Since the silicon dioxide-coated template is hydrophilic, a self assembled monolayer (SAM) is grown on its surface to render it hydrophobic and to promote adhesion between the template and the hydrophobic polystyrene or SAM-coated silica components. For these experiments, SAM coating was done using toluene based octadecyltrichlorosilane (OTS), the effects of which on interfacial energy in acetone-water systems are described at length in [4]. The template was cleaned using piranha, followed by rinses in water and then ethanol, and finally air drying to prevent polymerization of the SAM. During the same time, 6 drops of OTS were added to 75 mL of Toluene, and the resulting mixture was set aside for about 45 minutes in a covered tube. The solution was poured into a flask and the template was immersed in it face-up. The flask was covered with a lid and placed in an ultrasonic bath (3510R-DTH Bransonic, manufactured by UL Transonics Corp.) for 30 minutes in order to prevent coagulation of the coating at certain spots on the template and to ensure a more uniform coating quality. Thereafter, the template was cleaned by spraying it thoroughly with dichloromethane, followed by acetone, to remove any

remaining traces of the precursor (toluene-OTS) mixture. The functionality of the coating was then checked by pouring a small drop of distilled water on the template and visually inspecting the contact angle to ensure that coating was successful. A contact angle of greater than 90° between water and the coated surface shows that the surface is hydrophobic, while an angle less than 90° shows that it is hydrophilic.

3.3.2 Component preparation

Polystyrene microspheres with a diameter of 2.077 (+/- 0.045) microns were purchased dispersed in water from Polysciences, Inc. Polystyrene is naturally hydrophobic and does not need to be coated with a self-assembled monolayer (SAM). To prepare the assembly fluid mixture, the polystyrene microspheres were pipetted into various ethanol-water mixtures (4%, 8% and 20% water). The resulting mixtures were placed in capped microcentrifuge tubes and shaken on a Vortex mixing tool (Vortex-2 Genie, by Scientific Industries) for a few minutes to disperse the components. The polystyrene component dispersions were then shaken in the ultrasonic bath for about 5 minutes to break up any agglomerates of particles. The prepared particles were used immediately to prevent re-agglomeration due to settling. For the comparison experiments with silica microspheres, the silica spheres had a mean diameter of 1.85 microns and were obtained from Bangs Laboratories Inc. (Cat. No. SSO4N). The preparation technique was essentially the same as that described in [2-4], except that the SAM-coated microspheres were finally dispersed in ethanol-water mixtures rather than in acetone-water mixtures.

3.4 Self assembly protocol

A large (1325 cc) beaker was filled with water, and a 1.7 MHz frequency acoustic transducer (MMDIT-1.7, by Advanced Sonics) was placed at the bottom of the beaker. The height of water above transducer was kept fixed at about 4 cm. The input voltage (and thus power) to the transducer was controlled by a variable voltage transformer (L10C, by The Super Electronic Company). The input voltage can be varied from 0 V to 130 V, with a corresponding transducer electrical input power varying from 0 W to 36 W. The high transducer frequency ensures that operation is well below the cavitation threshold. A second, smaller beaker (the assembly beaker) was suspended above the transducer and immersed about 0.75 cm into the water in the large beaker. About 1.25 mL of the ethanol-water assembly mixture (of variable water concentration) was poured into the assembly beaker. Figure 3.4 shows photographs of the assembly set-up used. The template was placed in the beaker, face-up. A sufficient volume of the dispersed component mixture (between 700-800 μl) was added to the assembly beaker using a pipette. The small beaker was capped, power to the transducer was turned on, and the experiment was allowed to run undisturbed for 5 minutes. At the end of the experiment, the template was taken out of the assembly mixture, placed on a flat surface and allowed to air-dry. Power to the transducer was shut off after removing the template from the assembly beaker to avoid any sudden changes in ultrasonic flow field that might influence the assembly results [4]. The assembled template was then examined under an optical microscope. After the results were documented, the components were removed by 60 s of sonication in pure ethanol, and the template was reused in an effort to ensure geometrical consistency between runs.

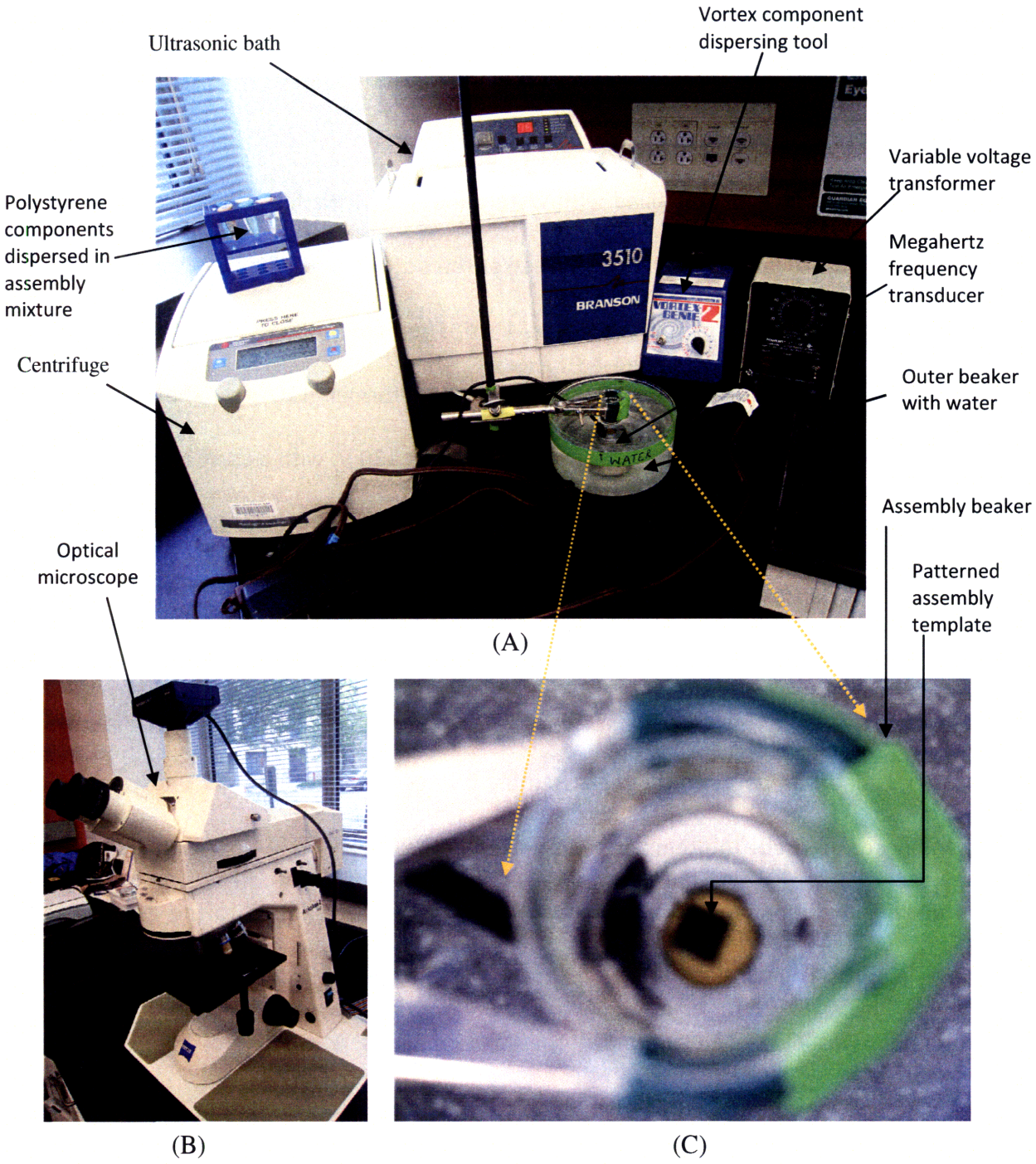

Figure 3.4: Photographs of the assembly set-up used for TASR experiments. (A) An overview of the experimental apparatus used. (B) Optical microscope used for imaging the assembly template (C) A magnified view of a portion of the set-up in (A). A megahertz frequency acoustic transducer is kept at the bottom of a large beaker which is filled with water. A smaller assembly beaker is suspended above the transducer in the larger beaker into which the patterned assembly template is immersed face-up

Experiments were conducted under a variety of conditions, including both polystyrene spheres and silica spheres as assembly components, different transducer voltages and different volume fractions of water in the assembly mixture. The results are presented and discussed in Chapter 4.

3.5 Comparative experimental study

In order to compare the assembly of PS microspheres to that of silica microspheres and also to gauge the effect of solvent on assembly results, a comparative experimental study was also carried out.

The candidate solvents for the assembly of both silica and polystyrene microspheres were methanol, ethanol, isopropanol and acetone. These solvents were chosen to match the interfacial energy range [2-4] that we were interested in for our experiments. The interfacial energy between two surfaces relates their contact area to the total free surface energy [4]. The method used for calculation of interfacial energy for a solvent mixture on a solid surface was discussed in detail previously in section 2.1.2. Methanol and isopropanol were rejected as candidates early on based on their not very promising initial assembly results as compared to those in ethanol and acetone.

Assembly experiments with both silica and polystyrene microspheres were carried out in both acetone-water and ethanol-water mixtures in order to characterize the assembly in the two fluid mixtures. The assembly process for the polystyrene microspheres has already been presented; the process for silica assembly differs only in the fact that silica microspheres must

be functionalized with a self-assembled monolayer (SAM) following the procedure described in [2-4] before preparation, whereas the naturally hydrophobic polystyrene spheres do not require this treatment. Although acetone-water mixtures are known from previous work to be an effective assembly medium for silica spheres, acetone did not prove to be suitable for polystyrene assembly. Acetone damages and distorts polystyrene microspheres over time scales of only a few minutes, as shown in Figure 3.5. In addition to the obvious drawbacks of an assembly liquid that damages the assembly components, it should also be noted that component distortion adversely affects the shape-sensitive TASR process. Therefore, ethanol-water mixtures were identified as the preferred assembly fluid.

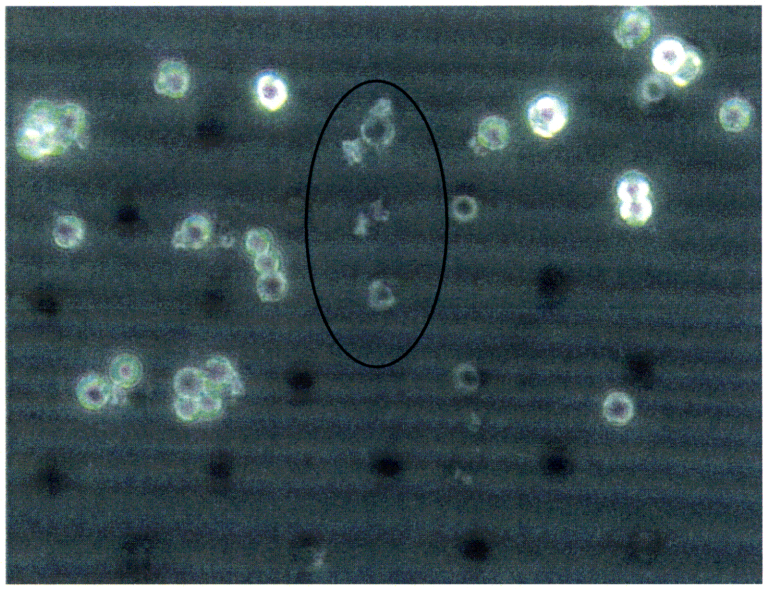

Figure 3.5: Optical micrograph showing visible distortion of polystyrene microspheres scattered on the silica template using 8% acetone-water assembly mixture at 40 V. The acetone causes swelling and dissolution of the polystyrene microspheres and causes failure of shape–matching of these components to the hemispherical sites fabricated on the templates for assembly using TASR

Results of the comparative study are discussed in Chapter 4. Apart from changing the solvent and assembly component material, a study of the influence of other assembly parameters such

as varying the voltage on transducer, the fraction of water in the assembly fluid, the density of components in assembly mixture etc. was also carried out, the results of which are also discussed in later sections.

3.6 Fabrication of deformable template replicates

Electron beam lithography is an effective means of patterning assembly templates, but it is not economical for manufacturing. One potential approach to minimizing the cost of assembly template fabrication is to create polymer replicas of master template patterns using the techniques of soft lithograhy. During the course of this research, deformable replicas were created from silica template masters by soft lithography both in order to address the issues of making use of a low-cost patterning technique for template fabrication and in order to assess the effects of substrate deformability on the TASR process. The process sequence for fabrication of these deformable templates was devised by Amelia Servi, a collaborator in the TASR project at MIT, and is documented here for completeness. Polydimethylsiloxane (PDMS) was used to create polymer replicas from the silica templates. PDMS is a commonly available polymer that can be poured in the liquid state on top of a master pattern and subsequently cured. Step-by-step details of the process sequence used are listed below. A schematic description of the two-sequence process is also shown clearly in Figure 3.6.

The silica templates were silanized by placing them in a vacuum chamber along with three drops of HDMS on a glass slide for one hour. Silanization of the silica surface was done in order to make the surface of the silica hydrophobic and to reduce the adhesion strength between the

silica surface and the PDMS. This step was necessary in order to facilitate the easy separation of the finished device from the silica during the last step in the fabrication process. While the silanization was in progress, the PDMS mix was created in parallel. In order to do this, a 10:1 mixture by weight of PDMS prepolymer with its curing agent (Sylgard 184 elastomer from Dow Corning) was measured out into a container. Since the mixture was observed to be highly viscous, an extra quantity of the mixture (at least 4g more than needed) was created in order to overcome the difficulty in removal of all of the mixture from bottom of the container. The contents of the container were mixed thoroughly with a stick and degassed in vacuum for 10-15 minutes in order to bring the air bubbles generated in the mixture onto the surface, where they were then removed with the help of a nitrogen gun. Since several moulds were created in a single batch, PDMS for multiple rounds was mixed at once and these were used within an hour of the mixing process. In order to constrain the flow of the liquid PDMS mixture and mould it in the desired shape, a 75x25mm slide box was created thereafter. Four glass slides were placed along an adhesive tape in alternating orientation at an angle of 90 degrees from each other. The sides were subsequently folded inwards so that the adhesive was inside the box which was done to assist the peeling off of the mold out of the slide box. The four-slide rectangle was then placed around another slide in order to form the bottom of the box, and adhesive was used to seal off the edges. The patterned silica wafer(s), created following the process sequence described in detail in Section 3.2, were then put into this slide box. For smaller wafers, a 25x25mm slide box was created instead of the 75x25mm box by standing all slides vertically while still using a slide as the bottom. Upside down wafer shards were then used to provide a larger area at the same height as the silicon chip of interest. After the slide box was created and

the wafer placed into it, the PDMS mixture was poured onto the wafer in this box using an approximate amount of 2.5 grams of mixture per 25x25mm area of the wafer. The PDMS layer on top of the template was baked thereafter in the box at 130 degrees C for 20 minutes in order to cure the polymer and promote cross-linking between its molecules. The mould was then peeled out of the box which was later discarded. Following this process sequence, PDMS molds of the patterned silica wafers were thus created. In order to get exact replicas of the original silica wafer, the same process was then repeated; the difference in the second run was that the PDMS mold created in the first step was now used as the master for the second molding sequence instead of the silica master as used before.

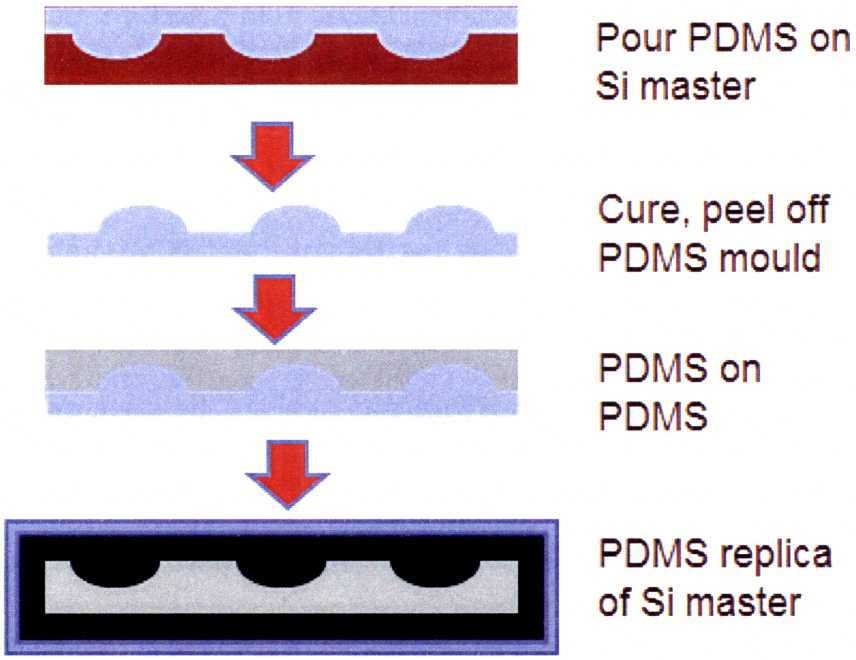

Figure 3.6: Schematic description of the process for fabrication of deformable PDMS replicates off patterned silica templates by a two-step molding process using soft lithography.

In order to make molds of the molds, the same directions were followed except for a few changes which are as follows. Since the PDMS molds obtained at the end of the first sequence were naturally hydrophobic, these were not silanized. The same type of slide box was used for the second sequence as that used in the first. However, since the PDMS mold had less weight than the silica wafer, during the second sequence some of the liquid PDMS tended to get under the PDMS master and push it upwards (unlike the case of the silica master, which owing to its greater weight stayed put). In order to overcome this problem, the first mold was made thicker than usual, using a mixture mass of 3.5gm per 25x25mm area of master instead of the 2.5gm as mentioned previously. In addition, the PDMS master became attached to the bottom slide with PDMS, and the slide was left was a permanent part of the PDMS master. In order to ensure smooth removal of PDMS mold layer from the PDMS master layer once the process was complete, before pouring liquid PDMS onto the PDMS master, adhesive tape was applied onto the flat parts created by the silicon shards used during the original molding. This was observed to be useful for separating the two layers of PDMS from each other upon completion of the process. After baking the mold, the glass sides were taken off of the box, and a razor blade was used to cut the PDMS layers apart along the plane of the adhesive tape. Great caution was exercised in removing the molds very gently, without sliding the razor blade over the active part of the template (which contained the grids of matching sites for components for self-assembly using TASR), since if all of the area surrounding the active area was detached, the layers would peel apart easily. Apart from the few differences mentioned here, rest of the steps and process parameters followed in order to create PDMS mold off the PDMS master were essentially the same as those followed in order to create the PDMS mold off

the silica master. At the end of the two sequences discussed above, PDMS replicas were created from the patterned silica master which we started off with. Figure 3.7 shows an optical micrograph of such a PDMS replicate made from the silica templates used in previous work [2-4] in order to demonstrate the effectiveness of technique for creating deformable patterned surfaces for TASR.

Since PDMS is naturally hydrophobic, it might potentially be used as a TASR template without the need to functionalize it with a hydrophobic self-assembled monolayer. This is one of the other advantages of using polymers for applications in TASR since some of the known and available polymers such as PS, PDMS, teflon etc. are naturally hydrophobic and hence do not need to be coated with a SAM in order to make them hydrophobic, thereby reducing the effort required in order to make them assemble successfully.

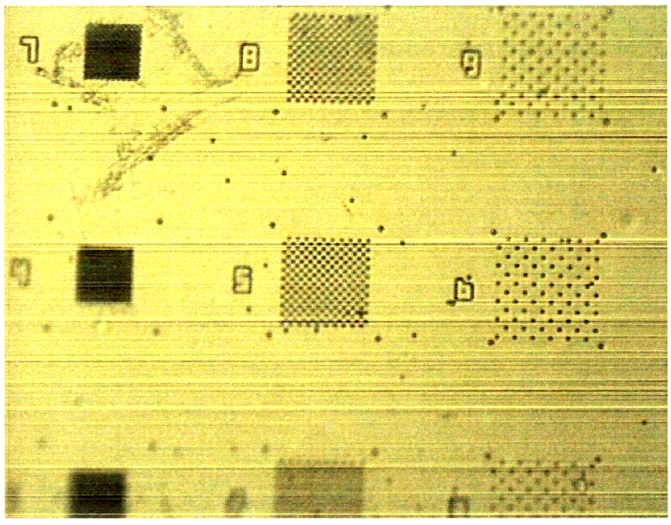

Figure 3.7: Optical micrograph of PDMS replicate created off silica masters used in previous work [2-4] using soft lithography in order to demonstrate the concept of patterning deformable templates.

Chapter 4

Results and Discussions

4.1 Overview

In this chapter, results of the experimental work are presented, followed by discussions and analysis. The results of the template patterning are presented first, followed by the assembly results, which demonstrate high assembly success for the case of uniform hole shapes and selective assembly for the case of varying hole shapes. Thereafter, the effects of assembly parameters, such as the voltage on the transducer and the water fraction by volume in assembly mixture, are discussed briefly. The assembly of rigid and deformable materials under similar assembly conditions is also presented.

Finally, the results are analyzed in the context of both the original and expanded TASR models described in Chapter 2.

Experimental Results

4.2 Template fabrication results

The template is imaged with an optical microscope to observe its grid pattern before using it for assembly. Figure 4.1 below shows optical micrographs of the patterned template before the assembly. An overview of a section of the template in Figure 4.1 (A) shows four grids designated 0, 1, 100 and 101. The holes in grid 0 (magnified view in Fig. 4.1 (B)) have the smallest starting spot size of 45 nm and exhibit the closest conformation to the desired hemispherical profile as compared to holes in other grids with larger starting spot sizes as seen previously in Figure 3.3. High assembly yield is expected in arrays with uniformly good hole shapes. In contrast, the holes in array 1 are grouped into 2x2 grids of holes with different starting spot sizes as seen in Figure 4.1 (C), as a means of analyzing assembly selectivity into holes of different sizes and shapes.

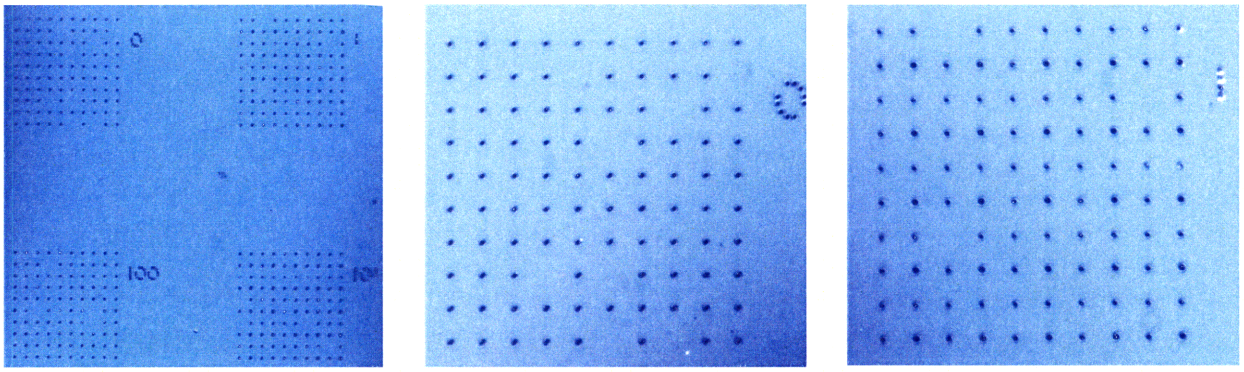

(A) (B) (C)

Figure 4.1: Optical micrographs of patterned template before assembly experiments using TASR. (A) Overview of four patterned grids with different starting spot sizes (B) Grid 0 comprised of uniformly sized holes with starting spot sizes of 45 nm (C) Grid 1 comprised of mixed 2x2 arrays of 45, 100, 200 and 500 nm starting spot sizes. Missing holes in grids are defects in the e-beam lithography or developing process.

4.3 Simultaneous and selective assembly

The deformable polystyrene spheres were assembled using TASR into matched sites in the patterned silica templates using the experimental protocol discussed in detail in Chapter 3. The assembly in this case was carried out in 8% water – 92% ethanol mixture at a transducer voltage of 45V. After assembly, the assembly yield was quantified by calculating the ratio of the number of holes of each size that are filled with components to the total number of holes of that size. Figure 4.2 (A) shows an optical micrograph of the portion of the assembly template shown in Figure 4.1 (A) after assembly of PS microspheres. Figure 4.2 (B) shows Array 0 with holes of uniform 45 nm starting spot sizes, almost completely filled except for a single empty hole. This corresponds to an assembly yield of 99%; this high yield is consistent with the fact that the holes are extremely well-matched in shape and size to the polystyrene spheres. This image is magnified progressively until a completely-filled defect free region with 100% assembly yield is visible clearly in Figure 4.2 (C).

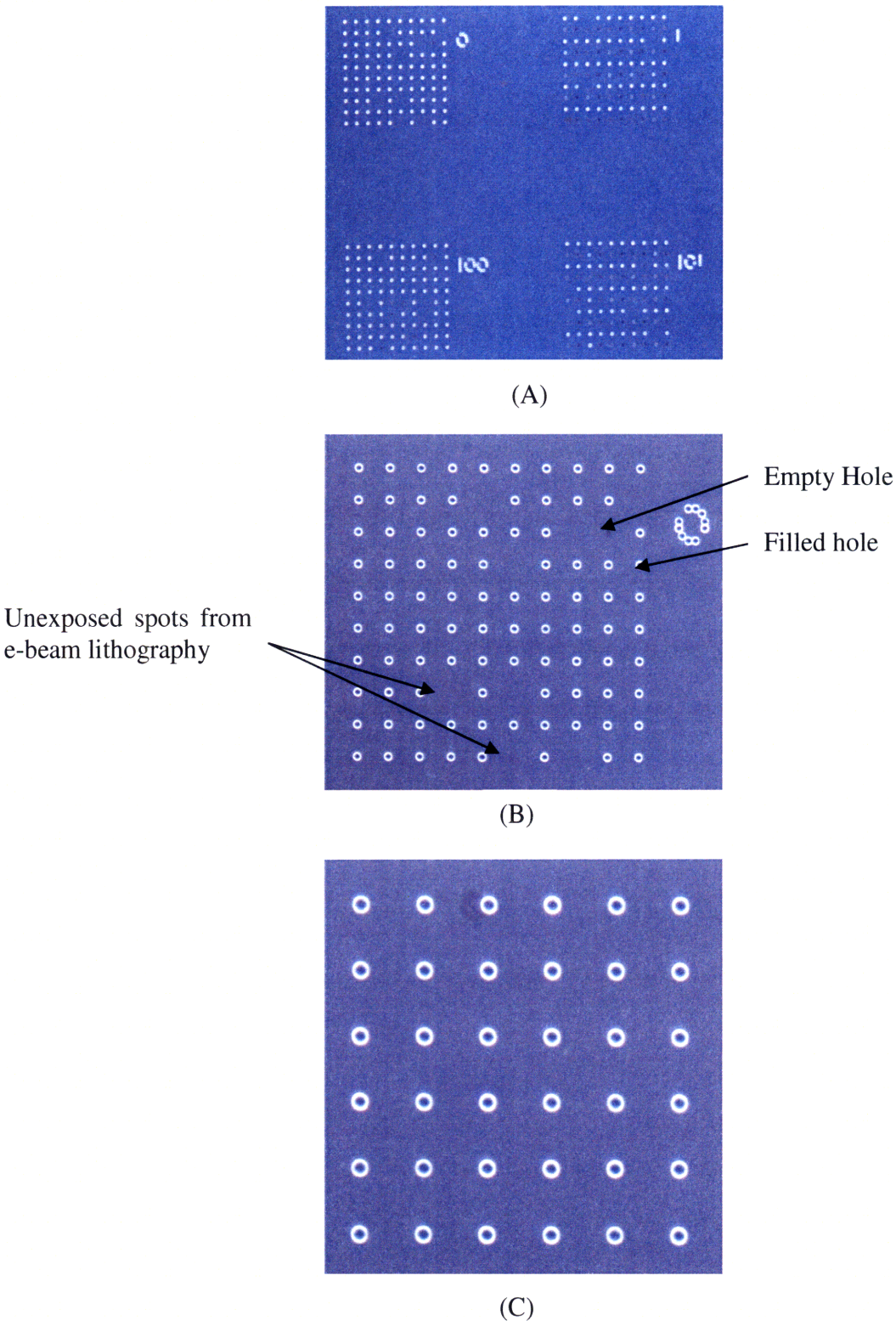

Figure 4.2: Optical micrographs showing polystyrene microspheres (2 micron in diameter) self assembled on a patterned silicon template using TASR. This demonstrates nearly 100% yield for a uniform array of holes with a starting resist opening 45 nm under these assembly conditions. Comparison with the known empty holes shown in Fig. 4.1 confirms that the circular patterns in these images are filled holes rather than empty ones

Whereas the uniform array shows uniformly high assembly yield, assembly results in arrays containing holes of different sizes (such as arrays 1 and 101 in Figure 4.3 (A)) demonstrated selective assembly.

As described previously, different sized holes were created in a single isotropic etch step by varying the size of the openings in the masking resist layer to produce features like those shown schematically in Figure 4.3 (C). In the 2x2 grid shown in the schematic, holes that are depicted to be the best match (closest to ideal hemispherical profile) are expected to be full, whereas the holes shown to be the worst match (largest deviation from ideal hemispherical profile) are expected to be empty. These expectations are supported by the experimental results shown in Figure 4.3 (B) and (D), which are optical micrographs of assembly results in the above described array comprising four different hole sizes/shapes organized into repeating 2x2 units. The results demonstrate selective filling of four different hole sizes/shapes created from 45 nm, 100 nm, 200 nm, and 500 nm starting resist openings. In this particular array (Array 1) and under these experimental conditions, the holes created from 45, 100, and 200 nm starting resist features were all filled, while the holes etched from 500 nm starting resist openings were unfilled.

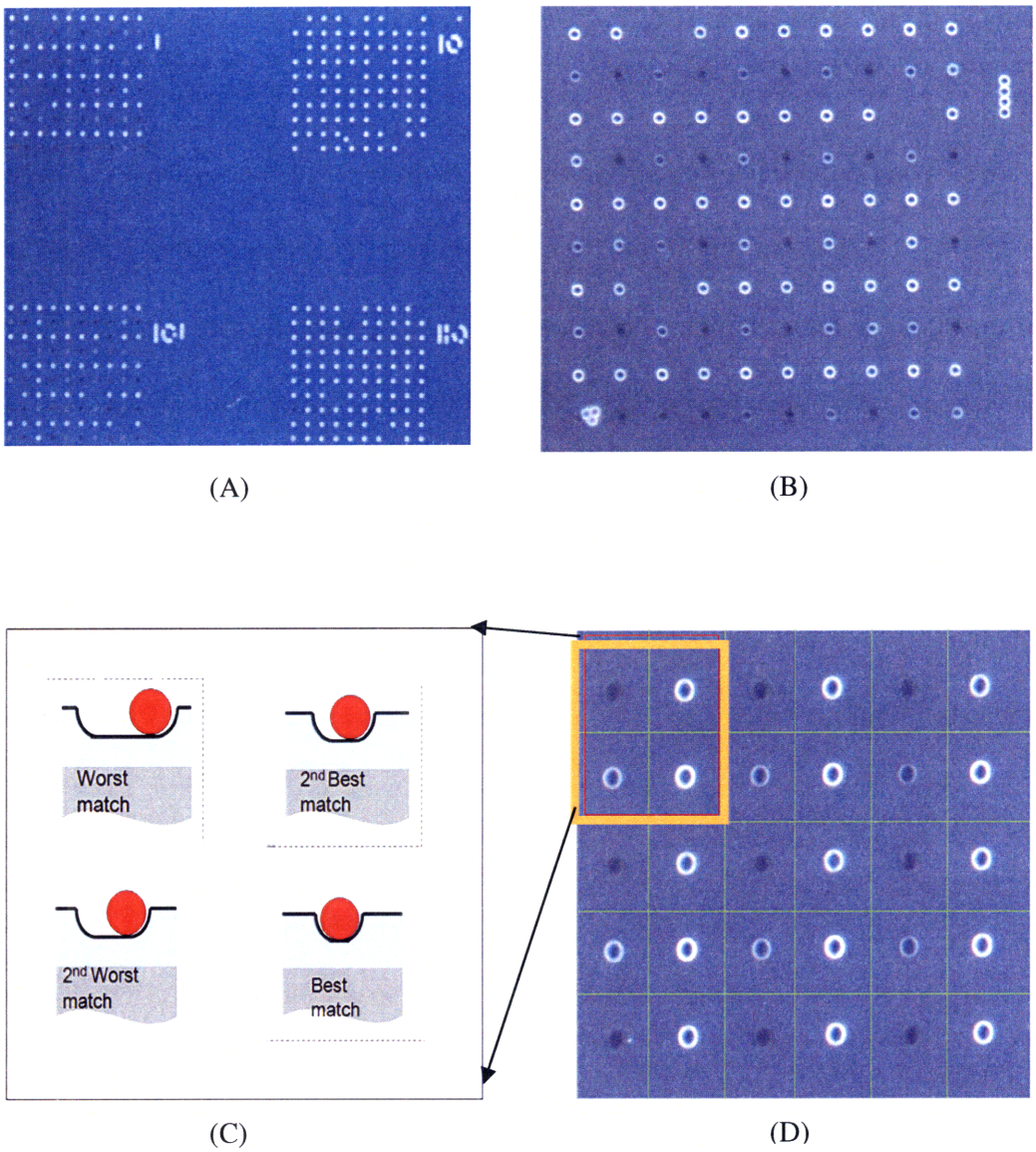

Figure 4.3: (A) Optical micrograph of section of template showing Arrays 1, 10, 101 and 110. While arrays 10 and 110 show uniform assembly, array 1 and 101 show selective assembly (B) Magnified optical micrograph of Array 1 (C) Schematic diagram of the repeated 2x2 pattern of different size/shape holes on the assembly template, with starting resist opening sizes of 500 nm (upper left), 200 nm (lower left), 100 nm (upper right), and 45 nm (lower right). (D) Optical micrograph of assembly into an array of holes comprising multiple units of the 2x2 unit pattern. The holes with the largest starting size are all empty, while the better matched holes are all filled

4.4 Variation of yield from template to template

The variation in yield between nominally identical assembly templates was also measured. The same experiments were run on three different templates using the same conditions of voltage on the transducer and water fraction by volume in the assembly mixture. The results are shown in Figure 4.4, which features optical micrographs of the same array on three different templates after assembly. This array has a starting spot size of 100 nm at the assembly sites. Keeping the rest of the assembly conditions same i.e. a voltage of 45 V on the transducer and using an assembly mixture that was 8% water fraction by volume, the yield varied by less than 4% from template to template.

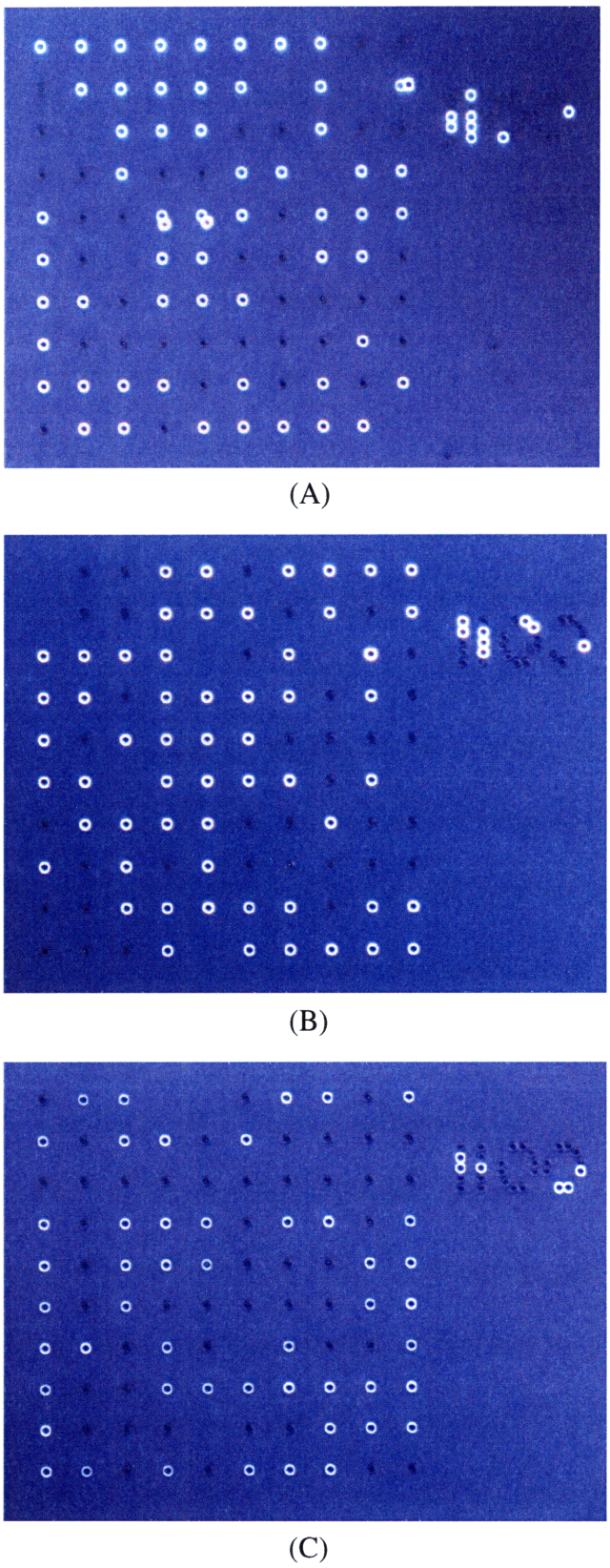

Figure 4.4: Optical micrographs showing variation in assembly yield from template to template under identical assembly conditions of 45 V and 8% water fraction by volume. The assembly yield varies from 60.64% in (A) to 61.3% in (B) to 57.4% in (C).

4.5 Influence of assembly parameters on yield

4.5.1 Effect of voltage on transducer

Illustrated in Figure 4.5 with the help of optical micrographs is how a 5V change in voltage on the transducer used in the assembly set-up influences assembly yield significantly. Yield first increases with an increase in voltage, reaches a maximum value and then decreases with subsequent increase in voltage. This trend observed in the case of the self assembly of polystyrene microspheres is similar to the trend observed in the assembly of relatively more rigid silica microspheres in previous work [2-4].

The reason for low yields at lower voltages is that there is not enough stirring of the medium at low input voltages; this results in poor circulation of the components in the flow field. The components are thus not able to find all of the assembly sites on the template, so that some holes that could successfully retain components remain empty for lack of component circulation to those sites. On increasing the input voltage, the fluid medium is stirred better. Although the removal agents also increase with increase in voltage, until a certain voltage, the retention agents are dominant. Therefore, the assembly yield starts to increase, since components find the appropriate locations on the template and stay in them as a result of the retention agents. Increase in assembly yield continues until a certain input voltage at which the removal agents become comparable to the retention agents. Further increase in the voltage beyond this point makes the removal agents dominant, and results in a decrease in assembly yield.

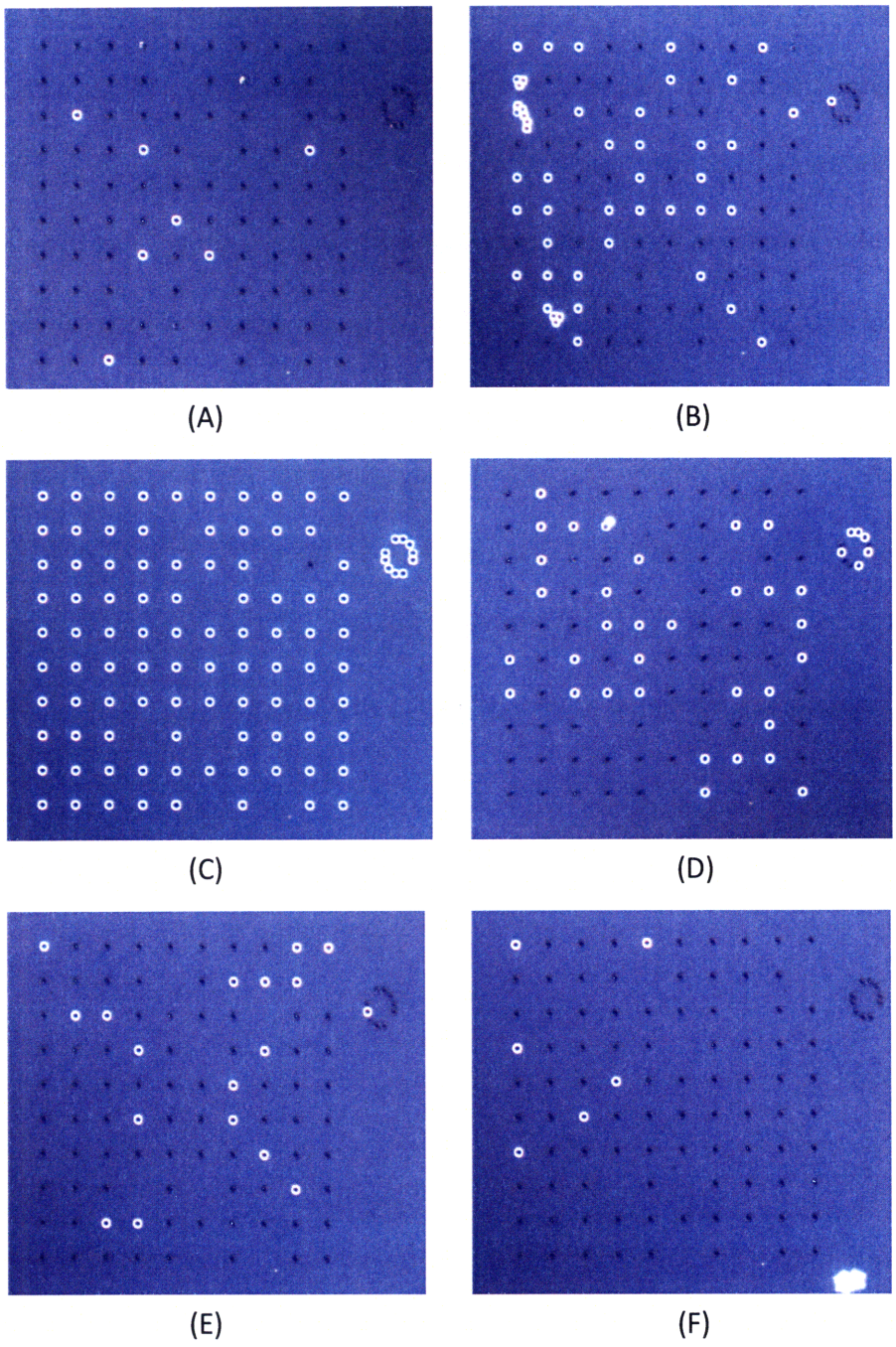

Figure 4.5: Optical micrographs showing effect of variation in voltage on the transducer on TASR assembly yield results. Experiments were performed at a water volume fraction of 8% with input voltages of: (A) 35 V, (B) 40 V, (C) 45 V, (D) 50 V, (E) 55 V, and (F) 60 V. Assembly yield climbs from a low value of 7% at 35 V to 98.9% at 45V before dropping down again to 6.5% at 60 V during the progressive increase in voltage.

A quantitative comparison of the fractional assembly yield with variation in voltage is depicted in Figure 4.6. The yield increases from a low value of 7 % at 35 V, to 41% at 40 V, to a peak value of 99.9% at 45 V; after that it drops to 36% at 50V, to 18% at 55V and finally to 6.5% at 60 V. The wide variation in yield with small changes in voltage shows that the assembly yield is very sensitive to voltage changes. The graph also shows that the fraction of defects is low. Defects in assembly are defined as components or their aggregates on the surface of the template which are not assembled correctly at the patterned sites. These defects are counted over the hole array area extended by a spacing of about one lattice on either side of the array. The number of such defects is divided by the total number of holes to give the fractional defect yield, in the same way the fractional assembly yield is quantified.

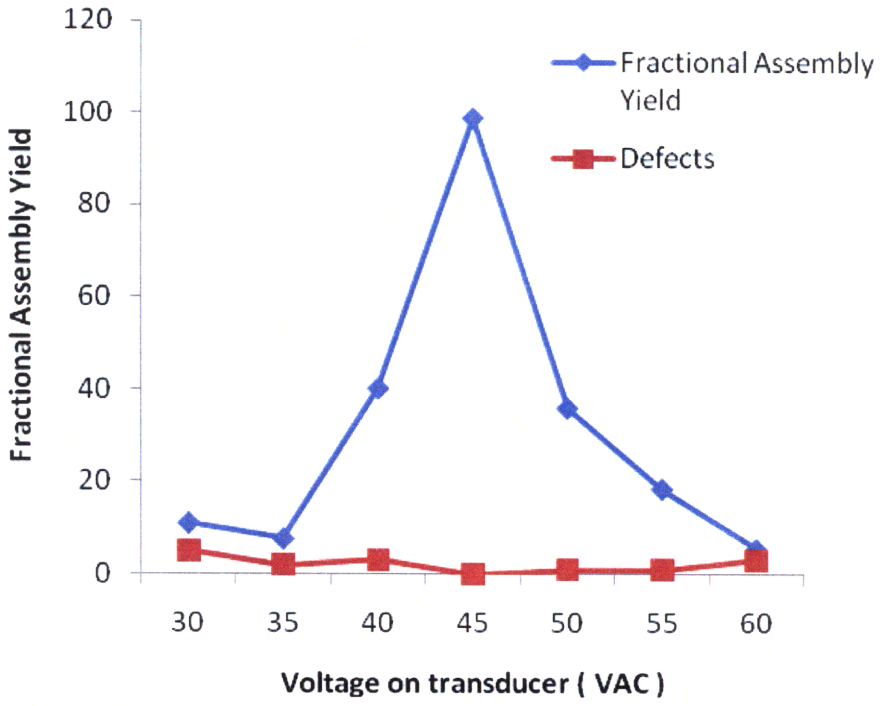

Figure 4.6: Variation of fractional assembly yield and defects in assembly plotted vs. voltage on the transducer during assembly. The assembly yield first increases with increase in voltage, takes a peak value of nearly 100% at 45V and falls down sharply thereafter with subsequent increase in voltage. Assembly defects are observed to be low.

4.5.2 Effect of volume fraction of water in assembly mixture

The self-assembly experiments using TASR were also done with assembly mixtures having varying concentrations of water by volume. The primary effect of changing the concentration of water in the assembly fluid is to change the mixture's interfacial energy with the SAM on the template; it also changes a few other fluid properties such as density, viscosity etc. that might affect the fluidic forces to a small extent as well. Optical micrographs in Figure 4.7 illustrate the effect on assembly yield when the water concentration in the assembly mixture is varied. Clearly, the assembly yield depends significantly on the interfacial energy of the solvent mixture, as also predicted by the original TASR model. On increasing the water concentration in the assembly mixture, the interfacial energy of the fluid mixture with the solid surfaces increases, as demonstrated previously in Figure 2.1. A higher input voltage is then needed in order to achieve high assembly yield at higher water concentrations in the assembly mixture. The best way to understand the relationship between the actual behavior of the system at different assembly conditions to the expected trends under these conditions is to observe the correlation of the assembly yield with the ratio of moments that promote component retention to moments that promote component removal, which will be discussed in detail in section 4.7.

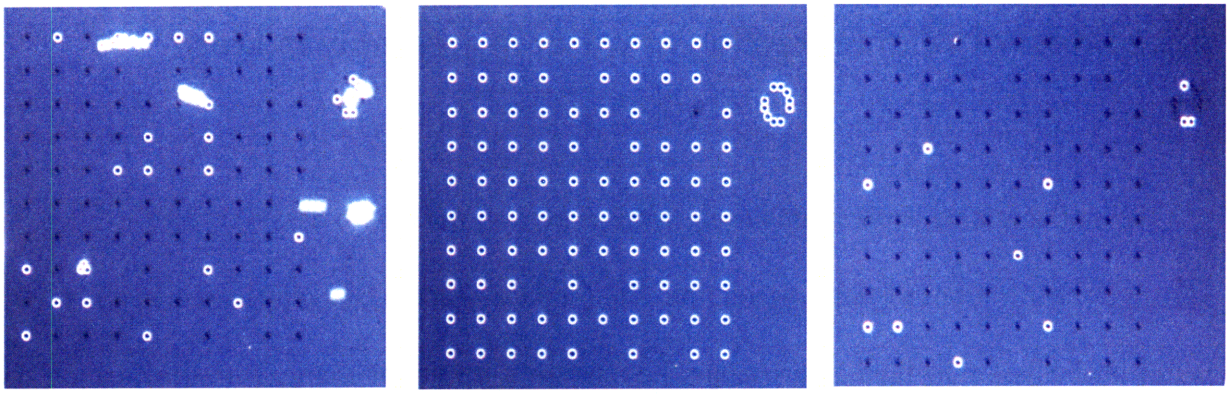

(A) (B) (C)

Figure 4.7: Optical micrographs showing variation in assembly yield with varying fraction of water by volume in assembly mixture, for water fractions of (A) 4% water (B) 8% water and (C) 16% water at 45 V. An assembly yield of 21.7% is obtained at 4% water, which increases to 99% on increasing water fraction to 8%, before dropping down to 8.7% at 16% water by volume in the assembly mixture.

4.6 Results of comparative assembly

As mentioned in Chapter 3, a study to compare the assembly of PS microspheres to that of silica microspheres (as in the previous work [2-4]) and also to gauge the effect of solvent on assembly results was carried out.

It was shown previously in Figure. 3.5 that PS could not be assembled using acetone on account of the distortion that occurs in PS in organic solvents such as acetone, toluene and benzene. Hence, acetone could not be considered as a solvent in the assembly mixture for the purpose of comparison of assembly of silica microspheres with PS microspheres. In contrast, a very good assembly yield for PS was observed using ethanol as the solvent. Since both PS and silica assembled well in ethanol, ethanol was chosen as the solvent for comparative assembly experiments with PS and silica microspheres on silica substrates.

Thereafter, the assembly of silica microspheres on a patterned silica template using ethanol-water mixture was compared to the assembly of polystyrene microspheres on the same template at the same voltage condition and water volume fraction concentrations in the assembly mixture. At a voltage of 45V and water fraction by volume of 8%, the yield for PS (99.9%) was observed to be much higher than yield for silica (45%). At higher voltages, such as 70 V, the yield for silica increased to 75% while yield for PS dropped to nearly 0%.

Analysis and Discussions

4.7 Model Verification

To better understand the role of component deformability in the functioning of the TASR process, the variation in assembly yield with variation in starting spot size and assembly conditions was considered in the context of the original TASR model [2-4] which relates the assembly yield in part to the degree of shape matching between the undeformed components and substrate.

In order to analyze this correlation between assembly yield and shape-matching, the fractional contact area between components and assembly sites on the substrate was calculated using the algorithm described in Section 2.1.2. To determine the nominal fractional contact area for each hole geometry, an 8^{th} order polynomial curve fit was made to the hole profiles obtained from AFM images using the surface analysis software SPIP by Image Metrology. Figures 4.8(A) and 4.8(B) are AFM images showing a cross-sectional profile and a 3-D top view of one of the holes on the template that had a 50 nm starting spot size. Compared to the other hole geometries on the template, this hole geometry was expected to result in nearly the best shape match to the 2 micron diameter microspheres; although holes created from the 45 nm starting spot size might be a slightly better match, the difference between the two is negligibly small. The 8^{th} order polynomial curve fit obtained for this particular hole on the template is depicted in Figure 4.8(C). Note that the top view reveals some deviation from the ideal axisymmetric hole shape assumed in the calculations, which could introduce some error into the nominal fractional contact area calculations if the component happens to interact with the affected region of the hole. The potential impact of such deviations will be minimized by

the fact that it is more energetically favorable for components to interact with better-matched regions of the hole surface.

The resulting hole shape was then compared with the sphere shape to determine the area over which the surfaces are within the contact distance (taken to be 1.5 nm here as in [2-4]). The nominal fractional contact area is then the ratio of the nominal contact area (neglecting surface roughness effects) between the sphere and the hole to the surface area of the sphere. The ideal case of full contact between a sphere and a perfectly-matched hemispherical binding site would correspond to a fractional contact area of 0.5, which means that the contact area between the sphere and the hole is 50% of the component's total surface area. As Figure 4.9 shows, a high fractional contact area of about 0.45 is observed for the case of contact between an un-deformed PS microsphere and a hole with a starting spot size of 50 nm when the sphere is placed at the point of maximum contact area with the hole. This is indicative of a high degree of shape matching between the component and the hemispherical site on the template and is a much higher value than previously recorded values [2-4], where the nominal contact area was always less than 10% of the component surface area.

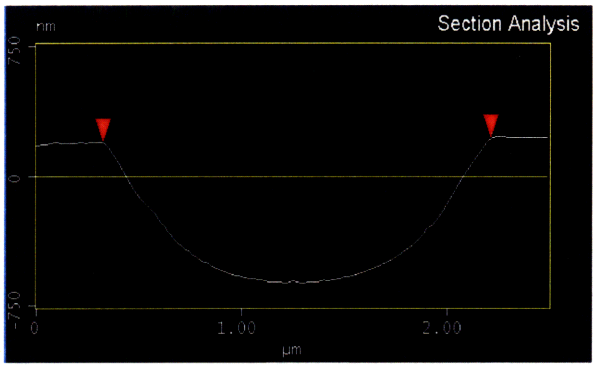

(A)

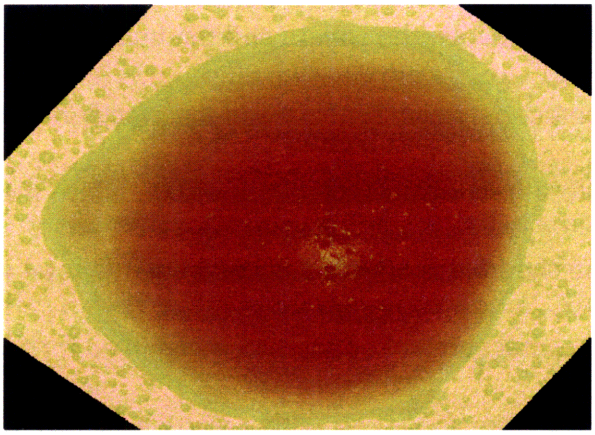

(B)

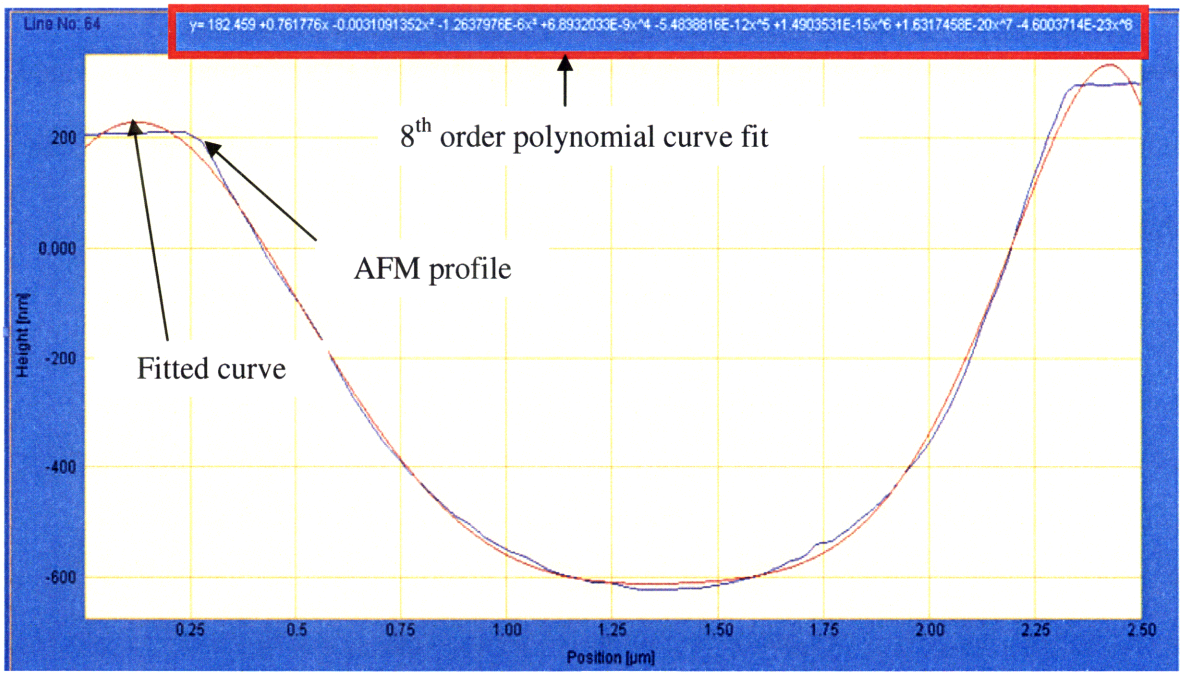

(C)

Figure 4.8: (A) AFM cross-sectional profile of a hole with a 50 nm starting spot size on a patterned silica template (B) 3-Dimensional view of the same hole in a top view (C) 8th order polynomial curve fit to the above hole profile using SPIP software by Image Metrology.

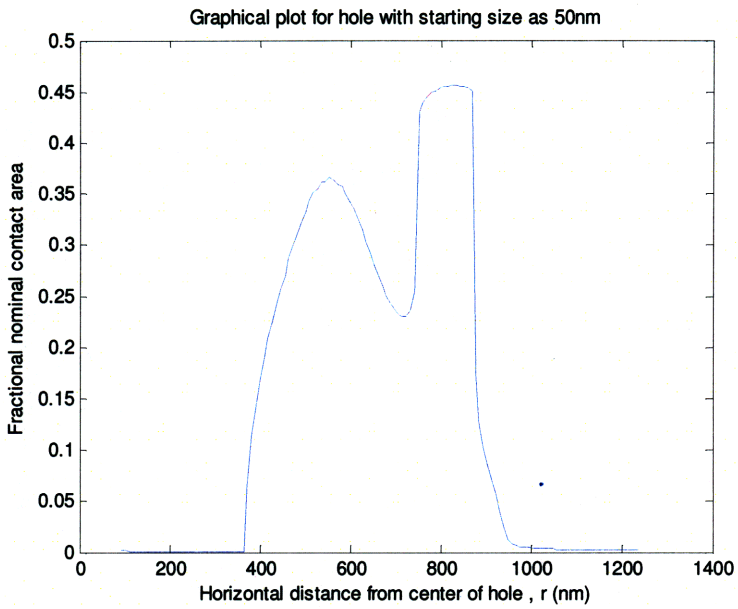

Figure 4.9: Plot of fractional nominal contact area (Ratio of nominal contact area between microsphere and substrate to the surface area of sphere without including effects of surface roughness) versus starting distance from center of hole, r (nm) for hole with starting spot size as 50nm.

Figure 4.10 shows a plot of the fractional assembly yield (where a fractional yield of 1 corresponds to an actual assembly yield of 100%) vs. the nominal size of the resist feature (the starting spot size) from which each hole was etched. Also plotted on the same graph is the nominal fractional contact area between an undeformed polystyrene sphere and the as-fabricated assembly site holes. The results confirm the expectation that a smaller starting hole size corresponds to a better component-hole match, and therefore results in higher assembly yield. A small resist opening size of 50 nm corresponds to a nominal fractional contact area of 0.45 and resulted in a high assembly yield of 100%. The largest resist opening size of 500 nm corresponds to a nominal fractional contact area of 0.003 and resulted in a very low assembly yield of 0.03%.

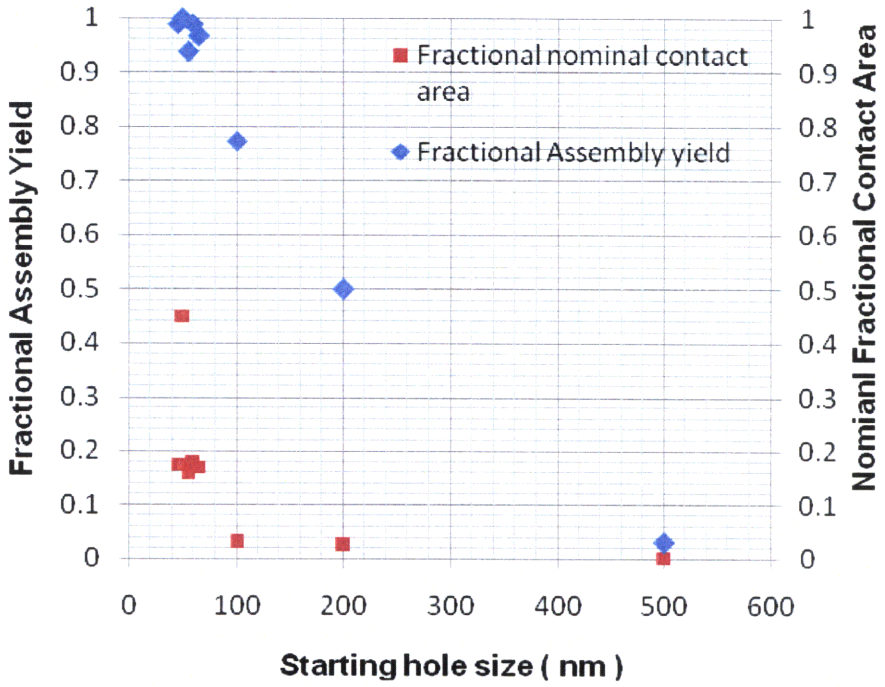

Figure 4.10: Fractional assembly yield and fractional nominal contact area plotted vs the starting spot size for holes on the patterned silicon template. As the starting spot size (and hence the hole size) increases, the fractional nominal contact area decreases and correspondingly, assembly yield also decreases

Following the analysis of Eid [3-4] and Jung [2], the effects of surface roughness on the assembly were also analyzed. In order to do this, atomic force microscopy was used to obtain the surface images of the components and the template surface at the nano-scale. Figure 4.11 shows some 3-dimensional surface plots and their cross-sectional views for a polystyrene microsphere self-assembled on a patterned silica template using TASR at different imaging ranges starting from a few microns going down to 10 nm. Figure 4.12 shows similar 3-D plots and section images for a patterned hole on the coated silica surface that is the assembly site for the polystyrene microsphere. Nano-scale images of polystyrene and coated silica surfaces were then used to analyze the surface roughness using surface analysis software (Nanoscope by Veeco). The rms values and peak surface heights for each of the mating surfaces were recorded

as shown in Table 4.1. Using these individual roughness parameters of interacting surfaces, the net roughness factor, C_r was calculated using equations (2.4)-(2.6) discussed in section 2.1.3 which was used to describe the overall effect of roughness of the system. This factor in our case was determined to be 0.2354, as shown in Table 4.1, with an error of ± 0.12, due to variation in rms roughness and peak heights over different parts of the polystyrene and silica surfaces.

Higher numerical value of roughness factor as determined in our case in comparison with values obtained in previous work [3-4] implies higher real contact area between the two mating surfaces as seen from Equation (2.7). This is attributed to the smoother surfaces of both the template and the component in the current work compared to previous work [2-4].

Table 4.1: Key surface roughness analysis results obtained for the polystyrene components and patterned silica template surface using Atomic Force Microscopy and Nanoscope software (by Veeco).

Surface Parameter	Value
Component rms roughness	0.153 nm ± 0.1 nm
Template surface rms roughness	0.310 nm ± 0.1 nm
Component surface peak height	0.751 nm ± 0.1nm
Template surface peak height	1.393 nm ± 0.1 nm
Roughness factor	0.2354 ± 0.12

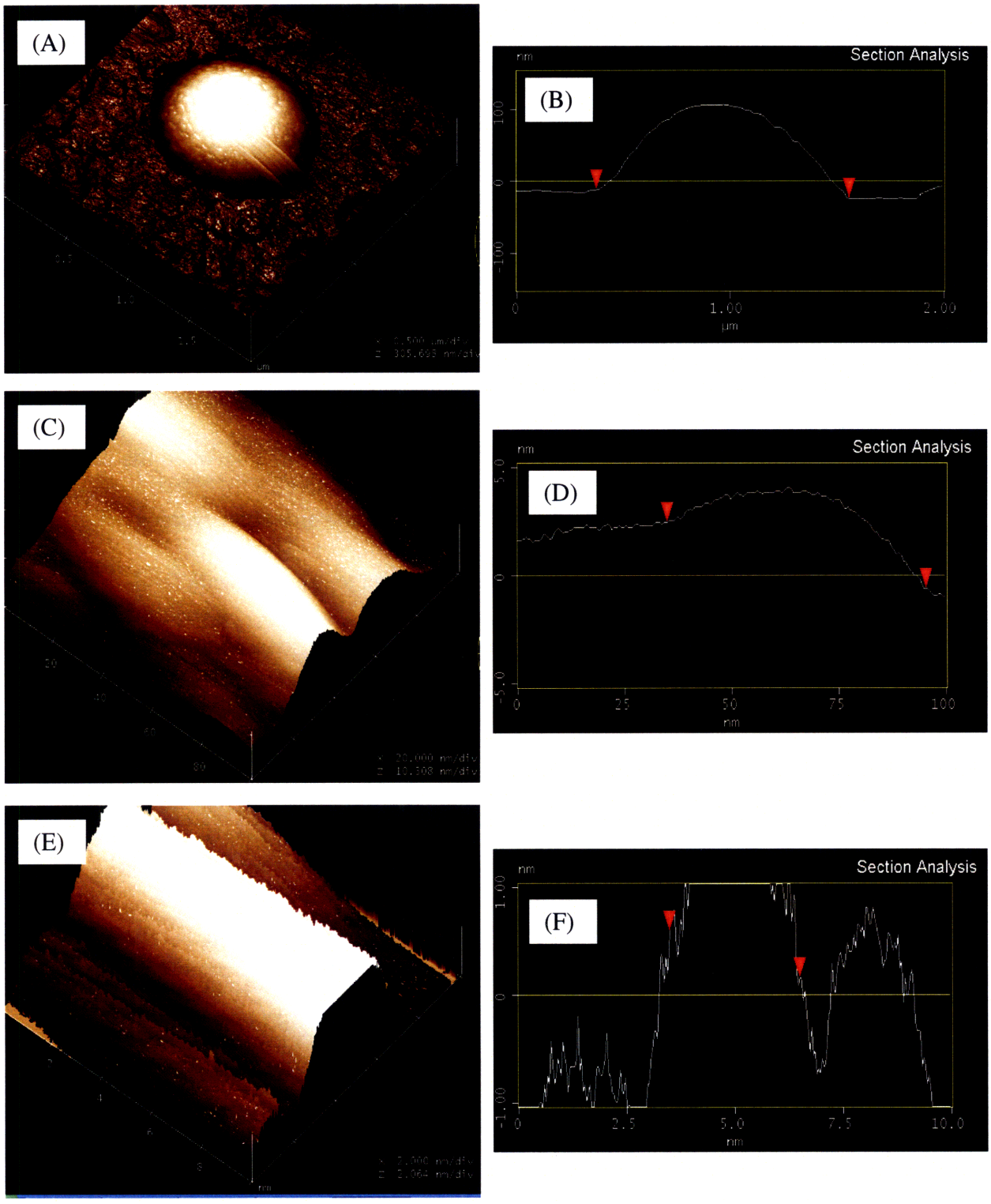

Figure 4.11: AFM images showing 3-D surface plots and cross-sections of a polystyrene microsphere assembled in an assembly site on a silica surface, at different size scales ranging from a few microns in (A)-(B) to 100nm in (C)-(D), down to 10 nm in (E)-(F). Surface roughness parameters for polystyrene such as rms roughness and peak heights were obtained from these images (Images courtesy of Amelia Servi).

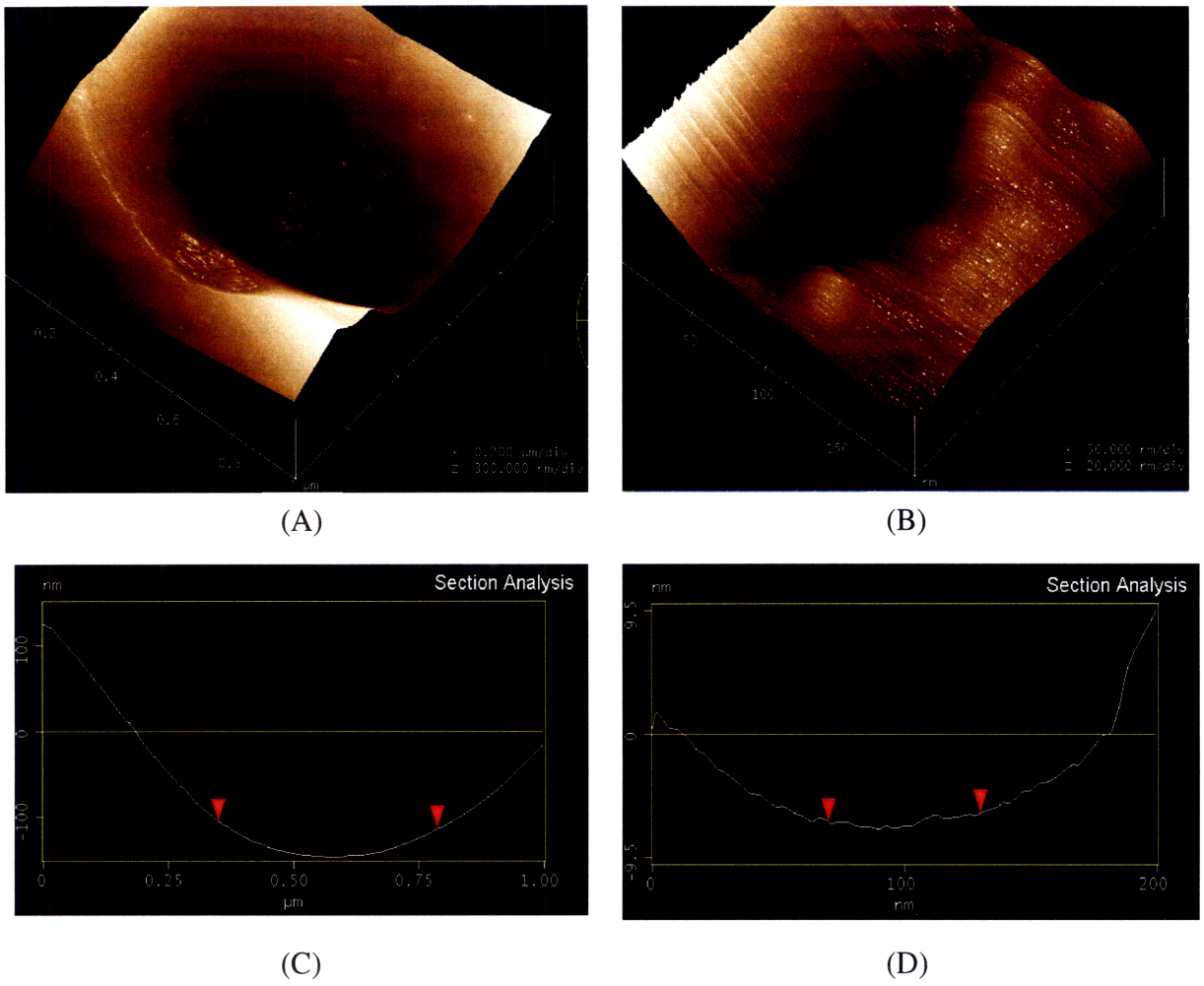

Figure 4.12: AFM images showing 3-D surface plots and cross-sections of a hole on the coated silica surface at different size scales. (A) and (B) show 3-D surface plots at size scales of 1 micron and 200 nm respectively while (C) and (D) are the corresponding sectional images of these plots. Surface roughness parameters for silica template such as rms roughness and peak heights were obtained from these images.

The results obtained from current experiments were then analyzed using the original TASR model to assess the degree to which the deformable sphere results show quantitative agreement with the original model for rigid structures. According to the original model, the transition from zero assembly yield to 100% assembly yield is centered about the point at which the ratio of the mechanical moments that promote component retention to the mechanical

moments that promote component removal is equal to one. The ratios of retention moments to removal moments for different experimental parameters were found using the values of retention and removal moments calculated from equations (2.8)-(2.20) as described in Section 2.1.5. The assembly yield was then plotted against moment ratio values, and the trend for variation of assembly yield as a function of this ratio was studied.

Figure 4.13 plots the experimentally measured assembly yield vs. the ratio of the mechanical moments for assembly both of the deformable polystyrene spheres and of the rigid silica spheres that were assembled for comparison purposes.

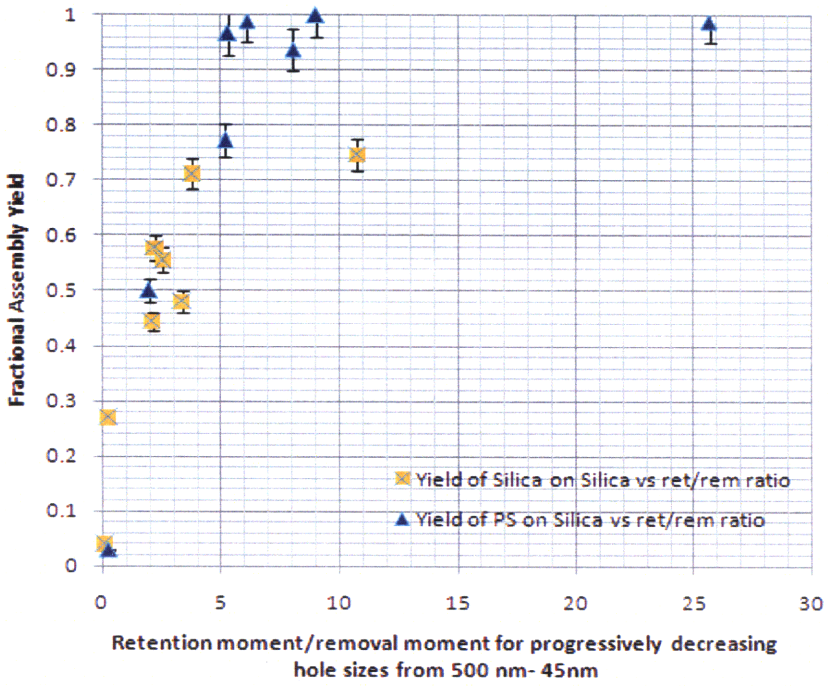

Figure 4.13: Plot of fractional assembly yield vs the ratio of retention moment to removal moment for assembly of both silica and polystyrene microspheres on a coated silica template

As seen from the figure, the silica and polystyrene assembly results exhibit similar though not identical trends of increasing yield with increasing moment ratio. . It can be observed from the figure that the trend for variation of assembly yield with variation in the moment ratios for silica closely follows the trend for PS. There is a slight variation in the trends at the farthest point in the plot which might be attributed to defects or accumulation of particulates on the template with progression of experiments. It can also be observed from the figure that the transition to full assembly yield appears to take place at values of the moment ratio that are higher than one. It should be noted, however, that the ratio of retention moment to removal moment has a degree of uncertainty in it, so that the moment ratio may not be precisely what it appears to be in the figure. This would not contribute scatter to the results; rather, it would shift a set of data points to either higher or lower values of retention moment while retaining the overall shape of the assembly yield curve. The quantification of the uncertainty in data values shown in Figure 4.13 is described in detail in Section 4.8.

These results show that TASR does work with deformable polystyrene spheres despite the fact that the ratio of the interference to the critical interference for polystyrene on a flat silica surface under typical TASR loads slightly exceeds the critical value of one for the onset of plastic deformation, as seen previously in Section 2.5.1, Chapter 2. At the same time, as mentioned before, the assembly results for PS are not identical to those of silica spheres.

The degree of success in the TASR assembly is explained by the fact that the deformable spheres assembled in holes rather than on flat surfaces. As mentioned before, the larger equivalent radius of curvature R_{eq} (calculated using equation (2.2)) for the sphere-hole contact decreases the ω/ω_c ratio for deformable spheres in holes as compared with deformable

spheres on flat surfaces. It was seen in Table 2.3 previously that the values of ω/ω_c for the polystyrene spheres in the holes were significantly below the critical value of one, and hence these cases were predicted to yield successful assembly results with TASR. This is consistent with the experimentally observed effectiveness of TASR for the polystyrene spheres. Assembly of defect spheres on flat regions of the template may remain a concern for systems in which the interference/critical interference ratio exceeds one on the flat even when it is less than one in assembly sites. The different ω/ω_c ratios calculated for the different hole sizes also correspond to different degrees of deformation of the spheres in the different-sized holes; this is consistent with the variation in optical appearance of the polystyrene components inside holes of different sizes that is visible in Figure 4.3(D).

4.8 Uncertainty calculations

There are uncertainties both in the assembly yield itself and in the calculated ratios of retention moments to removal moments. The error bar in the assembly yield is 4%, corresponding to the error obtained from repeatability of results in experiments. Following the analysis of [3-4], the uncertainty in the ratio of retention moments to removal moments is presented in this section.

There are several factors that could influence the uncertainty in for the calculated moment ratios. For example, minor variations between hole shapes can contribute to the uncertainty. There are also uncertainties in the experiments that arise from any variations among the spheres, and from any variations in the surface coating at different locations on the template. However, it was shown in previous work [3-4] that the fluidic uncertainties were the dominant factor in the system, and hence minor variations in ratio calculations due to uncertainties caused by the factors discussed above will not be considered here. Fluidic uncertainty emerges mainly as a result of the spatial variation in the acoustic excitation in the apparatus used, as mentioned previously in Section 4.6. In order to quantify the uncertainty in the moment ratio (ret/rem), results from calorimetry experiments done by Jung [2] were used, since the current experiments and analysis were done following similar experimental conditions as those used in [2]. Based on his calculations, the uncertainty in intensity, I_o at the template surface, at an input voltage of 45 V was calculated, which, for a template position at the center of the beaker (as also maintained in current experiments), was found out to be ± 11.32 W/m^2. This uncertainty was used to determine maximum and minimum values for the intensity in the beaker; these

values in turn were used to determine the corresponding minimum and maximum values of retention to removal moment (ret/rem ratio).

It was found that the uncertainties in the values of surface roughness also affect the values of the retention and the removal moments to a considerable extent. As seen in section 4.7, there is an uncertainty in the value of the roughness factor for our system, as a result of the variation in rms values of surface roughness and peak heights for both the component and the template surfaces. This variation in the roughness factor was used to find the maximum and minimum values of retention to removal moment ratio, similar to the effects of intensity variation discussed before.

Therefore, taking into consideration the net uncertainty in the system, maximum ret/rem values are obtained at a minimum intensity (since this corresponded to a minimum removal moment) and maximum surface roughness factor (corresponding to minimum roughness, higher fractional contact area and therefore, higher adhesive retention moments) whereas the minimum ret/rem values correspond to the maximum intensity and minimum surface roughness factor. Figure 4.14 plots the fractional assembly yield (with its error bars) vs. the minimum, maximum, and nominal values of the ret/rem ratio for the assembly of PS microspheres on patterned silica template. The assembly conditions for these values are same as those for the data shown previously in Figure 4.13. As seen from the figure, upon inclusion of uncertainties in the system, the transition from low assembly yield (less than 50%) to high assembly yield (higher than 50%) is centered about ret/rem ratios of less than one for the case of minimum experimental values, about two for nominal values, and about five for maximum experimental values. The transition to near 100% assembly yield is complete at higher values of

the moment ratio (about four for minimum experimental values, and as high as 18 for maximum experimental values).

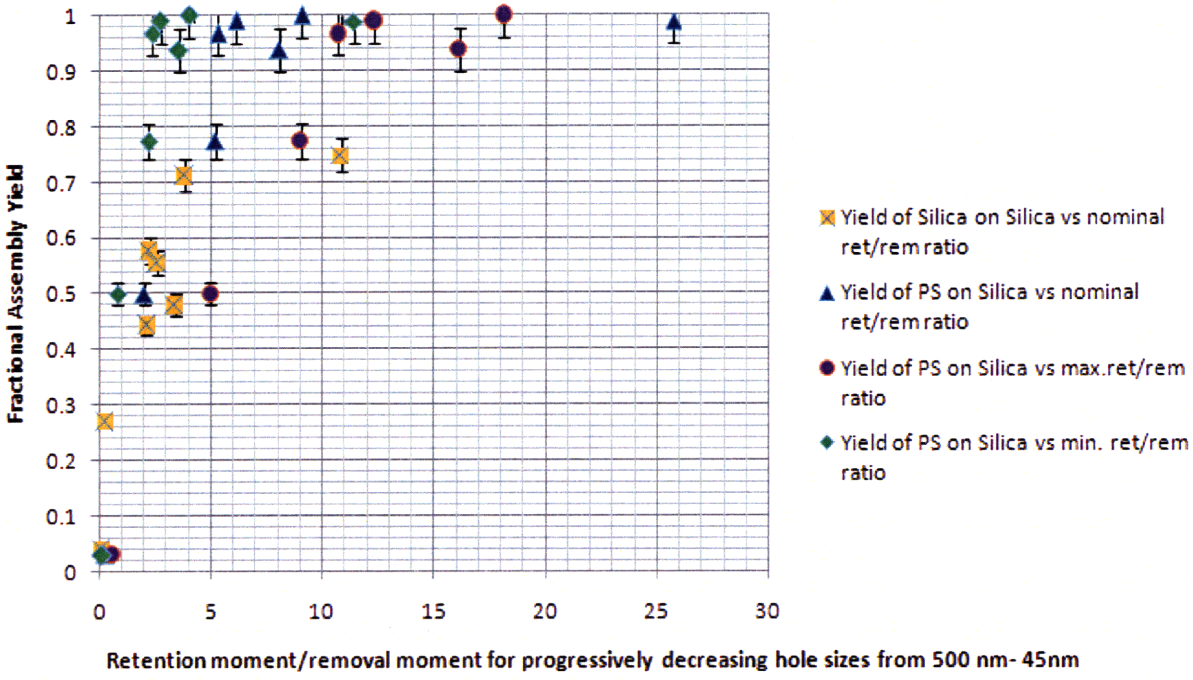

Figure 4.14: Measured assembly yield plotted vs. the ratio of retention moments to removal moments (ret/rem values). The yield is plotted vs. the minimum, nominal and maximum values of ret/rem ratio, taking into account uncertainties in the intensity of the acoustic excitation due to spatial variation and the value of surface roughness.

The uncertainty analysis clearly shows that, within the uncertainty bounds for the present experiments, the trend for variation of fractional assembly yield with ret/rem ratios is essentially identical for the assembly of both PS and silica microspheres. This shows that the original TASR model can, in fact, accurately describe assembly in systems comprising deformable materials when deformation of the assembly components is purely elastic in nature.

4.9 Possibility of plastic deformation at the nano-scale

One might wonder whether nanometer-scale asperities due to substrate roughness may result in a small amount of plastic deformation in the deformable spheres that could enable an increase in contact surface area and disrupt the TASR process. At extremely short length scales, the template surface resembles a rigid surface with asperities that can indent the relatively flat surface of the deformable spheres. Even if the plastic deformation that results from nanometer-scale asperities dissipates relatively little energy overall because of the small volumes of material that are involved, it may disrupt the energy balance enough to modify the detailed assembly results. Although the original TASR model agrees with the data obtained here quite well, the possibility for such local plastic deformations is assessed here.

In order to do that, cross-sectional views of the templated silica surface at the patterned assembly sites were first examined closely at the scale of a few nanometers in order to observe the distribution of the asperities, if any, on the surface, which could be potential sources of plastic deformation. Figure 4.15 shows cross-sectional images of two different locations in a single hole on the silica template that was used to carry out experiments. The top-views of the images were obtained by atomic force microscopy, while the cross-sectional analysis was obtained from the AFM images using a surface analysis software package (SPIP by Image Metrology). It is seen from the figure that the aspect ratios of some of the 'peaks' is as low as 0.1, in the worst case. This suggests that the possibility of such topography on the template surface being a potential source of local plastic deformation for the deformable sphere surface is low.

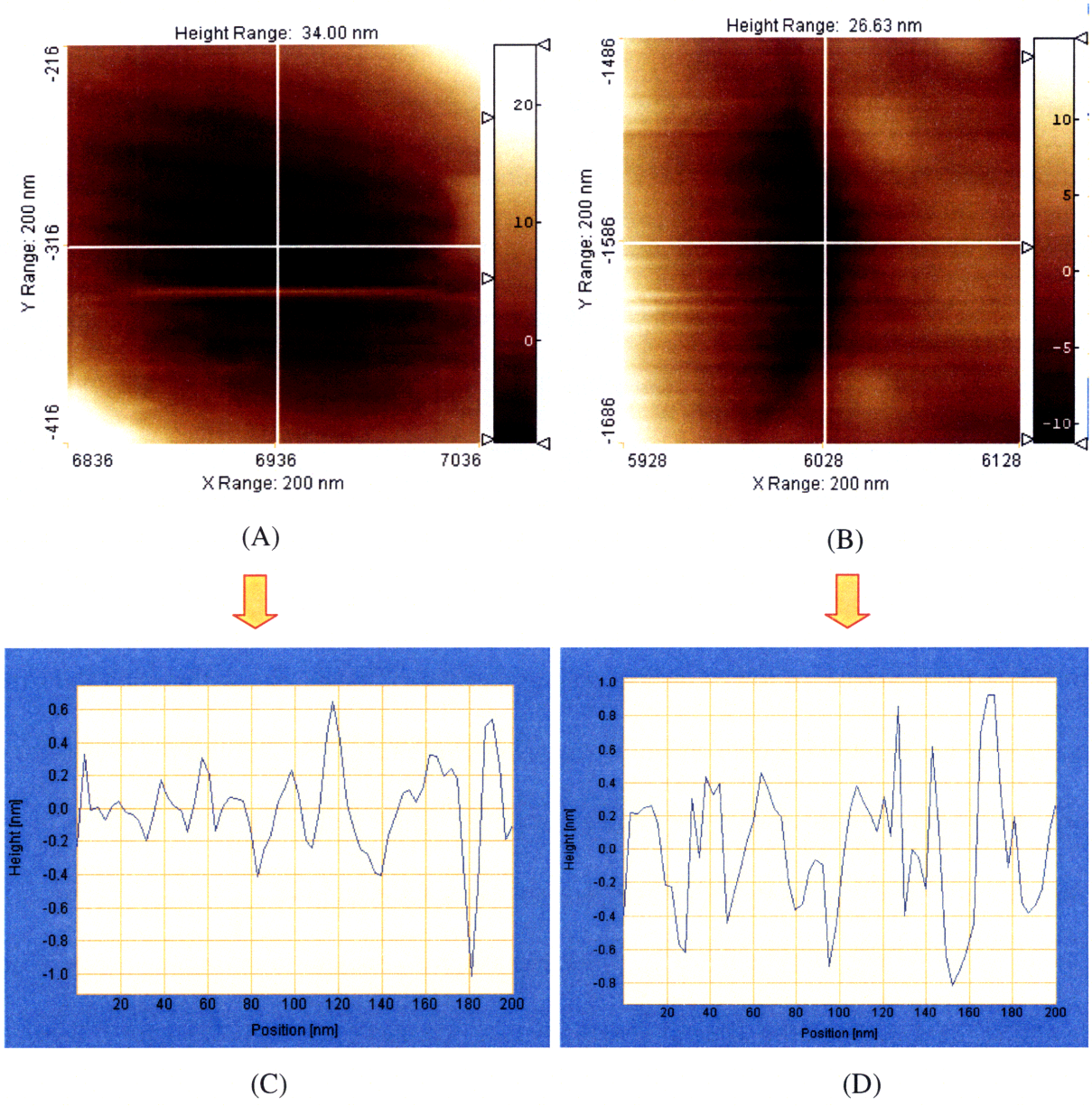

Figure 4.15: Cross-sectional roughness analysis showing aspect ratios of nano-scaled peaks on the as-fabricated silica surface of the template at the patterned sites. (A) and (B) are top-views of two different locations inside a hole on the template surface obtained by atomic force microscopy. (C) and (D) are cross-sectional views of (A) and (B) respectively obtained using surface analysis SPIP software package by Image Metrology. Low aspect ratios in topography suggest that nano-scale plastic deformation of polystyrene microspheres due to asperities on patterned silica surface will be minimal if it occurs at all.

However, this observation is also tested theoretically, by means of an elastic-plastic contact analysis between rough surfaces. This is done following the basic concepts of elastic-plastic surface contact analysis described previously in Chapter 2. A Plasticity Index, ψ, can be defined to describe the nature of contact at the interface of the two rough surfaces under consideration. The surfaces can equivalently be represented by a rigid rough surface in contact with a smooth deformable surface. The value of ψ is then given by the equation [36-37]:

$$\psi = \frac{E'}{H}\sqrt{\sigma_{eq}/R} \qquad (4.1)$$

where E' is the combined modulus as described previously in equation (2.23), H is the hardness of the softer material, in this case, the polystyrene microsphere, σ_{eq} is the equivalent rms surface roughness value as defined in equation (2.4) which takes into account the roughness of both the component as well as the template surfaces, and R is the radius of curvature of the surface asperity which is assumed to be nearly spherical at the summit.

For values of the plasticity index ψ of less than 0.6, the contact is found to be mostly elastic in nature [36-37]. When the value of ψ exceeds 1, the contact turns to mostly plastic. Between 0.6 and 1, the nature of interaction is elastic-plastic. Substituting the appropriate parameter values for our case of a PS microsphere contacting the silica substrate, the values for plasticity index are calculated for different radii of curvature of the surface asperities, as shown in Figure 4.16. As seen from the figure, as the radius of curvature of the surface asperity (assumed spherical at summit) increases, the chances of having plastic deformation in the system decrease, indicated by low values of the Plasticity Index, ψ. However, for sharp asperities

having radii in the range of a few hundred nanometers, the surface of the deformable material undergoes local plastic deformation, since the value of ψ exceeds 1 for such cases.

Therefore, the occurrence of nano-scale, localized plastic deformation in the system will mainly depend on the radius of curvature of the asperities on the rough surface within a particular region of contact. As seen from Figure 4.15, this radius of curvature near the summit is varying widely from peak to peak, which might lead to onset of localized plastic deformation at a few locations, while the contact might be elastic at others. The sharpest features seen in 4.15 have a radius of curvature of approximately 100 nm, which might cause a negligible amount of localized plastic deformation.

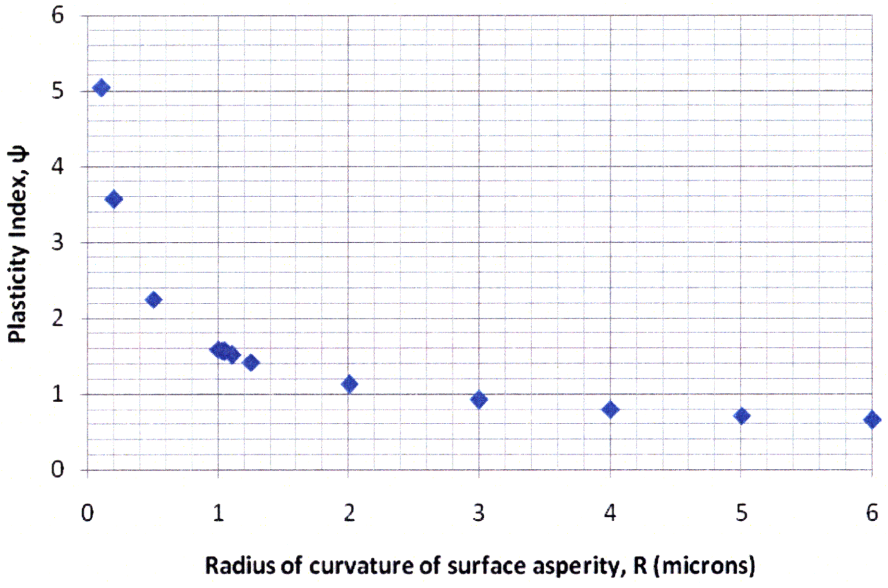

Figure 4.16: Plasticity Index, ψ plotted vs. radius of curvature of asperities, R on surface. As the radius of curvature increases, the value of Plasticity Index decreases. Purely elastic regime extends for values of ψ below 0.6 which are obtained for radii of curvature of 6 microns and above, while predominantly plastic regime extends for value of ψ above 1 which are obtained for radii of curvature below 2 microns.

This is as expected in theory, as mentioned by Green wood et. al. [37], since most surfaces at this scale have a plasticity index greater than 1.0 except for exceptionally smooth surfaces. On the other hand, there are also certain flatter regions on the template site as seen from the figure where the contact between the PS microsphere and the template will be fully elastic.

It is to be noted here that the localized plastic deformation caused in certain regions of the interface are not significant enough to disrupt the overall energy balance of the TASR set-up since the overall contact still remains elastic. This is determined by the low density of sharp asperities over the surface and also the negligible estimated radial as well as axial spread of the plastically deformed region in the vicinity of the asperity, which is known to stabilize over a period of time [37]. Since it is not possible to achieve perfectly smooth surfaces in reality, complete elimination of plastic deformation from the system when working with deformable surfaces might not be possible. However, by a better control of the template fabrication process, it may be possible to minimize the surface roughness which will eventually lead to a 'flattening' of the asperities and bring down the average value of the Plasticity Index at the surface. This will promote a more elastic contact at the interface, and may eventually lead to better assembly results in TASR with deformable materials.

Chapter 5

Conclusions and Future Work

5.1 Conclusions

In this thesis, the successful, TASR-based, shape- and size-selective assembly of deformable microcomponents on rigid substrates was demonstrated for the first time.

Previous work [2-4] using TASR focused on the assembly of rigid microspherical components on rigid template surfaces. The assembly of deformable microcomponents using TASR, which works on shape and size selectivity, was identified as a challenging task due to the possibility of change in shapes due to increased contact area between the component and the substrate as a result of deformation.

A theoretical model was first created in order to predict the conditions under which TASR-based assembly of deformable components on a rigid substrate will be successful. This model, which complemented the original TASR model, was used to identify the mechanical nature of contact at the interface of the assembly component and the template substrate. The success of this model was then demonstrated by comparison of the model predictions with experimental results for a component material (polystyrene) for which the material properties lie near the boundary of how much deformability can be tolerated by the TASR process.

Based on model predictions, the assembly of polystyrene microspheres on a patterned silica template was considered experimentally. Rigid silica components were also assembled under

identical conditions in order to compare the results for the assembly of rigid and deformable materials. Patterned silica templates were created which showed excellent conformation to the ideal hemispherical profiles desired for assembly of microspheres into the matched sites. The results for assembly of deformable polystyrene microspheres on these patterned substrates exhibited both a good degree of assembly selectivity of given deformable components into different-sized holes, and very high assembly yields of up to 100% for deformable components in well-matched holes. These results showed agreement with the predictions of the theoretical model for assembly of deformable materials using TASR.

The experimental results were also examined in the context of the original TASR theoretical model [2-4]. It was found that the original model can be extended to describe the behavior of deformable materials under many (though not all) experimental circumstances despite the variation in contact area which occurs as result of the deformation.

A detailed analysis of the effect of varying the experimental parameters on the assembly yield was used to determine the ideal conditions that needed to be maintained in order to achieve high assembly results. The trends in variation of assembly yield on varying these controllable parameters helped elucidate the TASR process for self-assembly of deformable systems in greater depth. Similar trends were observed in the assembly of rigid and deformable materials.

Therefore, a strengthened theoretical foundation was used to successfully demonstrate and analyze experimentally, the selective assembly using TASR in deformable systems. Further verification of the theory for deformable materials proposed here is possible by extension of experimental work to encompass a broader range of deformable materials.

5.2 Challenges for future work in progress

There are several new directions that can be taken from this point forth in work related to TASR. Some of these courses of study are discussed here in relation to the results of current study. The theoretical model presented in this thesis considers in detail the case of deformable components assembling on relatively rigid substrates. The *theory for deformable substrates* also needs to be more fully developed, taking into account the range of elastic behavior in different materials. Examining the role of deformability in the template substrate theoretically as well as experimentally will be a key issue for assembly into low-cost, replicated, polymer-based templates.

While the current work successfully extends the applicability of TASR from rigid materials into a new domain of polymers, there are other interesting options available as well to which TASR study can be extended, such as *biological materials*. The possibility of introducing *anisotropic components* into the assembly arena should also be considered and worked upon. Based on these aims and guidelines, some of the work that is currently in progress in this direction is glanced upon in following sections.

5.2.1 Extension of theoretical modeling

The theoretical model proposed so far describes the mechanical contact analysis for cases of deformable microspheres contacting rigid substrates as a metric for the success in assembly using TASR. The theoretical framework has also been extended for certain deformable substrates such as PMMA, which for all practical purposes, can be treated as rigid substrates in comparison to the deformable spheres that are assembling on them in terms of possibility of plastic contact. Further analysis to describe completely the assembly of systems involving deformable materials should focus on describing the case of rigid microspheres impinging on deformable substrates. One of the suggested starting points in order to assess this case has been discussed previously in section 2.4.3, where literature results from finite element modeling are used to calculate the critical value for transformation of contact from the purely elastic to the elastic-plastic regime. Although this method gives a good starting point, more work needs to be done taking into account a host of new materials in order to make this analysis general and applicable to any such system. The theoretical results obtained for such a case will also have to be verified experimentally.

So far, the work related to TASR has only focused on the assembly of spherical components, both theoretically as well as experimentally. The experimental extension of TASR to components of new shapes will require the supporting theoretical model to describe such cases. While the basic TASR model (as developed in [2-4]) for structures other than spherical still needs to be developed, the current model proposed here based on Hertzian elastic theory

might be extended to describe the contact mechanics of shapes other than spherical by taking into account the mean radius of curvature obtained from curvatures in different directions.

Another theoretical extension will have to be made in the model to describe biological systems using TASR. The mechanical analysis of biological systems is not straightforward and would require several assumptions to be made in to describe the elastic behavior of species such as animal cells, human RBC, DNA or spores accurately. Biological factors causing change in shape of the species under consideration also need to be taken into account in such a case where mechanics might not be able to describe the behavior of the system completely.

5.2.2 Approach to self-assembly of biological materials

The concept of assembly of deformable materials using shape and size selectivity can potentially be extended to include biological materials as well. One promising area for study is cell-sorting using this technique. Because of the lack of having well-defined shapes for many biological materials, TASR might not be applicable to all biological systems as mentioned before. However, some relatively robust biological species pose cases of interest and relevance to self-assembly using TASR.

One such case being considered currently for future work is the self assembly of SF-9 cells. The SF9 insect cell line is a clonal isolate derived from the parental *Spodoptera frugiperda* cell line IPLB-Sf-21-AE1, 2. The cells belonging to this clan are fairly robust and maintain a spherical shape in culture for relatively longer periods of time before attaching themselves on the surface available. Once attached, they can be easily removed from the surface once again by providing slight agitation. The cell line is highly susceptible to infection with *Autographa californica* nuclear polyhedrosis virus (AcNPV baculovirus), and can be used with all baculovirus expression vectors (*e.g.* Invitrogen's Bac-to-Bac® and Bac-N-Blue™ Expression Systems) to produce recombinant proteins. Upon infection with this baculovirus, the cells burgeon in size and go from an approximate mean diameter of 15 microns before infection to a mean diameter of around 22 microns upon infection with the baculovirus. Therefore, from a small population containing a mix of both the infected and uninfected cells, cells of each type can be separated out using the concept of size selectivity for self-assembly using TASR. This concept is explained better with the help of Figure 5.1 which shows images of the SF-9 cells before and after

infection, indicating cell viability during the process of infection and also shows optical micrograph of the template that has been fabricated for demonstrating experimentally the same concept.

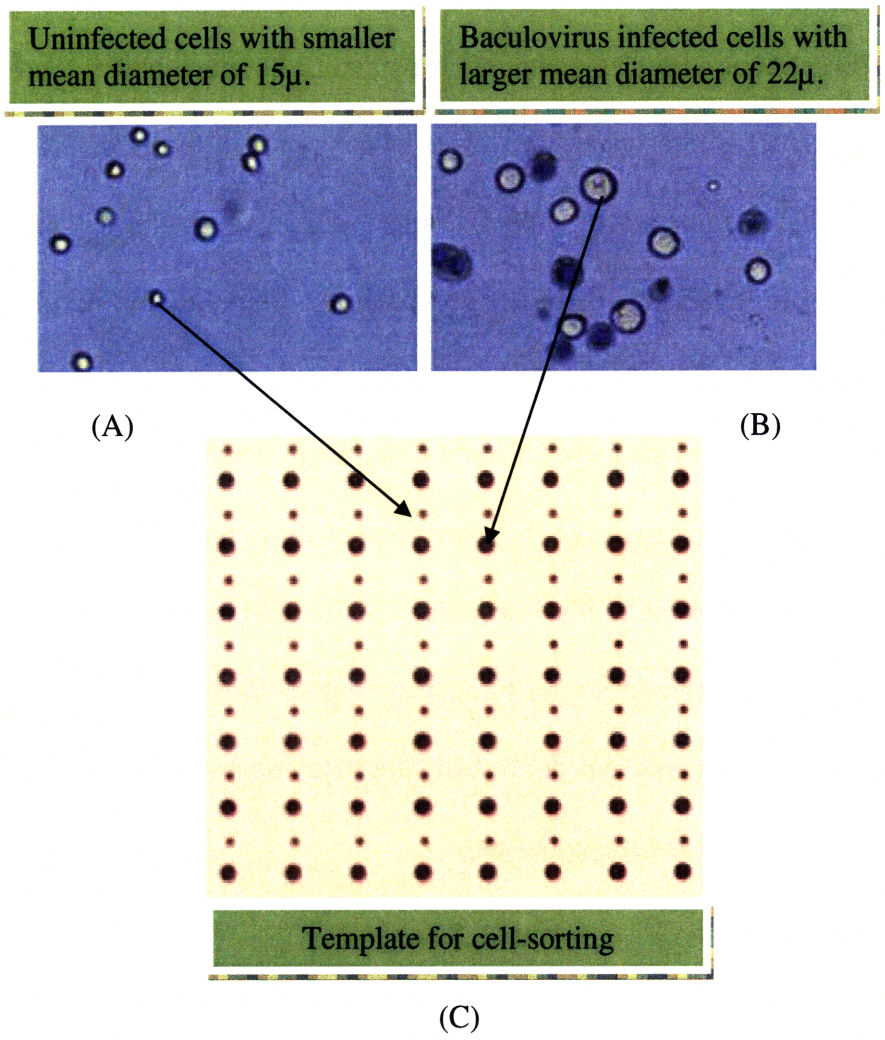

Figure 5.1: (A) Image of healthy SF-9 insect cells (B) Image of enlarged SF-9 cells after infection with baculovirus. Cells labeled in blue with the help of a dye called Trypan Blue indicate dead cells after infection with virus (C) Optical micrograph of silicon master template created for sorting of the healthy cells from infected cells based on concept of size selectivity and self-assembly using TASR.
(Images of cells taken from www.nexcelom.com)

Since the cells are nearly spherical in shape, therefore, matching hemispherical profiles are required on the patterned template for self-assembly using TASR. The process sequence used for creating the hemispherical holes on the substrate for the self-assembly of cells is quite different from that used for the assembly of polymeric microspheres such as PS on silica as listed in Section 3.2. The main difference in the process arises due to the fact that the hemispherical holes required for assembly of cells need to be much bigger than those for the assembly of microspheres. Starting with a blank silicon wafer in order to create the master template (from which templates of materials more suited for biological purposes can be created by use of soft-lithography using the approach mentioned in Section3.5), the isotropic etch needed in order to create the final profile is therefore done on *silicon* itself using Plasma etching rather than on *silica* using the Buffered Oxide Etch as has been done till this point. A schematic diagram of the process used for fabrication of these templates, shown in Figure 5.2 highlights the key aspects of the fabrication sequence. An SEM image of one of the 15 micron diameter holes on the patterned silicon template created using the above approach is also shown in Figure 5.3. Experiments in order to test, illustrate and understand this concept of self-assembly of cells using TASR are still underway.

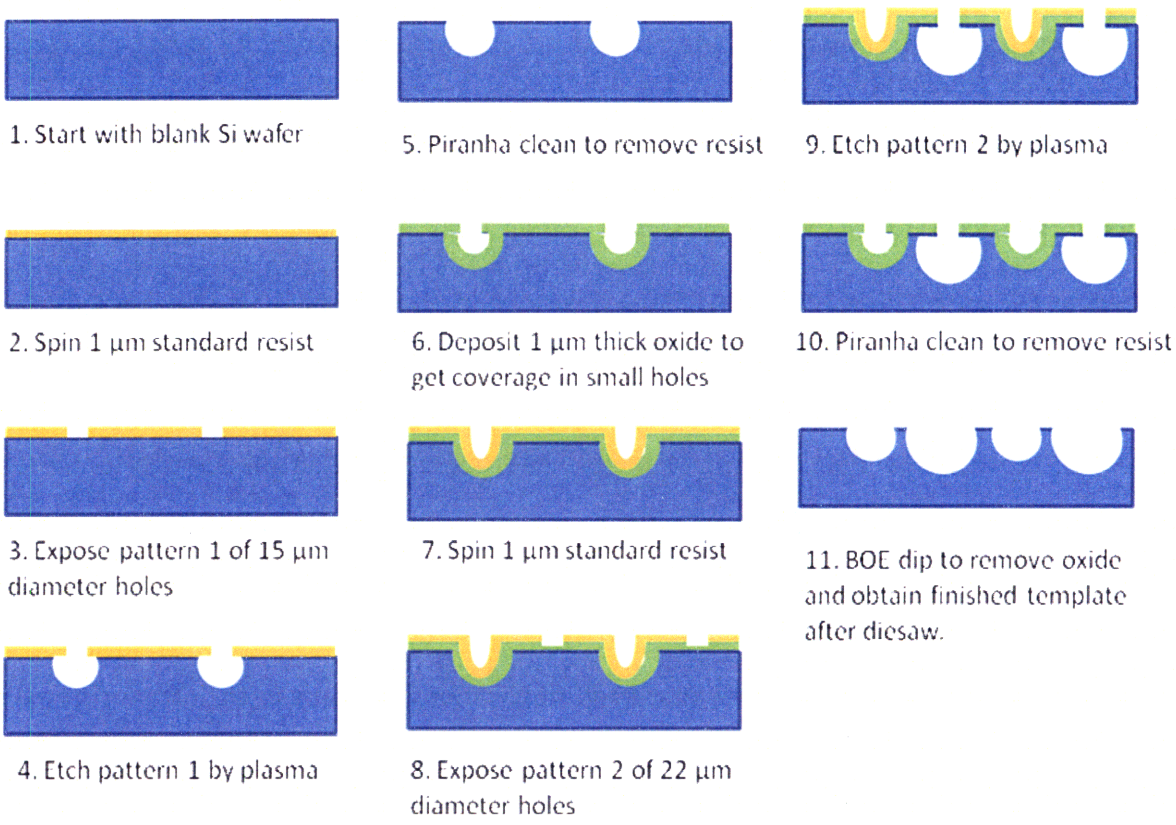

Figure 5.2 Fabrication process flow highlighting key steps to be followed for creating silicon template masters for the purpose of cell sorting of different sized SF-9 cells using TASR.

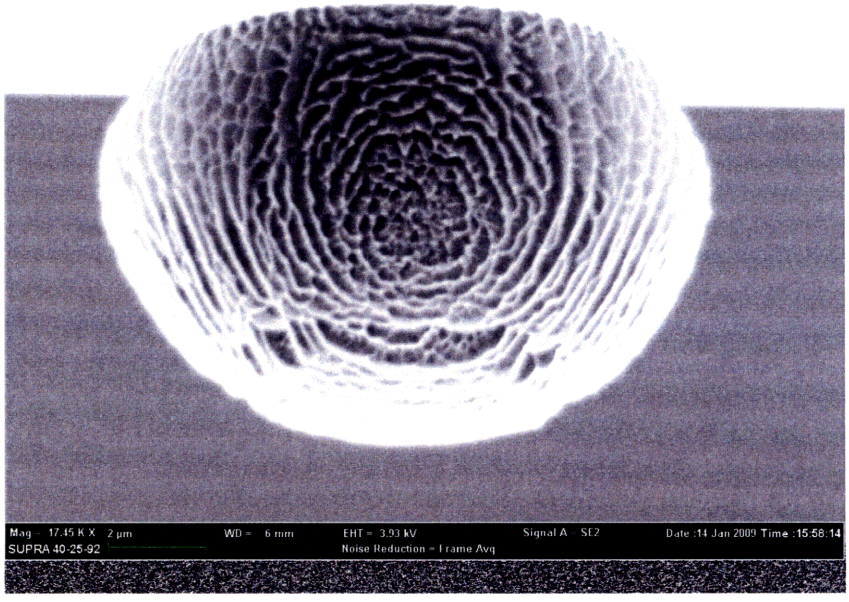

Figure 5.3: Scanning Electron Microscopic image of one of the holes on the patterned silicon master template fabricated for self-assembly and sorting of SF-9 cells. The nearly isotropic hemispherical profile, with slight undercut observed is achieved by deep reactive ion etching of silicon.

5.2.3 Approach to self-assembly of components of new shapes

Another field of current interest in self-assembly using TASR is the assembly of anisotropic components. Successful assembly of shapes other than microspheres will open up new possibilities for applications of this technique. One such targeted area of application that could utilize self-assembled structures made of components with shapes other than spheres is in creation of electrical connections where metal nanorods or wires in the form of nano-sized cylinders might be more practical to use than spheres. Based on these lines, current work related to TASR is also focused on the assembly of shapes other than spheres in order to extend the applicability of the process to new materials, applications and processes. Introducing a new shape into the process introduces complexities not only in the experiments but also in the theoretical analysis. One of the potential challenges that could be faced experimentally in the assembly of components having anisotropic shapes might be controlling the orientation of the component in order to make sure that it always lands in the assembly site in the same orientation as exists on the assembly site on the template, since for certain applications, components might always be desired in the same orientation. The analysis of forces and moments as has been used in the original TASR model to describe the competition of retention vs the removal will also change accordingly. In the theoretical analysis of deformable systems comprised of anisotropic components using the new TASR theory introduced here in Chapter 2, the Hertzian contact theory will have to be extended to incorporate different radii of curvature of the component in different directions, as is usually the case for anisotropic components.

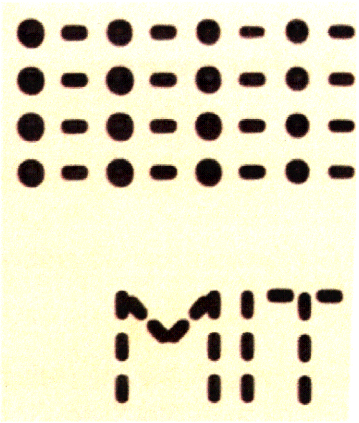

Figure 5.4: Optical micrograph showing patterned silicon template with patterns containing both cylindrical as well as spherical assembly sites aimed at the simultaneous assembly of different shapes using TASR

Another interesting case for analysis using TASR based on the above discussion might be the simultaneous assembly of isotropic and anisotropic components, where each component finds its respective matching site on the template. Inspired by this concept, we have fabricated silicon templates with nano-sized semi-cylindrical assembly sites that alternate with hemispherical sites for demonstrating simultaneous assembly of cylindrical and spherical 3-D objects. An optical micrograph of a small portion of the fabricated template is shown in Figure 5.4. Future work will focus on testing of these devices experimentally and extending the TASR theory to encompass and describe the self-assembly of objects with anisotropic profiles.

References

[1] George M. Whitesides and Bartosz Grzybowski, Self-Assembly at All Scales, *Science* 29 March 2002: Vol. 295. no. 5564, pp. 2418 – 2421

[2] S. Jung and C. Livermore, Nanoletters, Achieving selective assembly with template topography and ultrasonically induced fluid forces, Vol 5, no.11, p. 2188-94, 2005.

[3] F. Eid, S. Jung, C. Livermore, Templated assembly by selective removal: simultaneous, selective assembly and model verification, Nanotechnology 19 (2008) 285602.

[4] F. Eid, C. Livermore, Simultaneous Templated Assembly of Different-sized Nanocomponents by Selective Removal, M.S. Thesis, MIT, June 2006.

[5] Mizuta, H. et al. Nanoscale Coulomb blockade memory and logic devices, Nanotechnology 12, 155-159 (2001).

[6] George V. Eleftheriades, Keith G. Balmain, Negative-refraction metamaterials: fundamental principles and applications, John Wiley and Sons, 2005

[7] Aizenberg, J., Braun, P. V. & Wiltzius, P. Patterned colloidal deposition controlled by electrostatic and capillary forces, Physical Review Letters 84, 2997-3000 (2000).

[8] Xia, Y. N., Yin, Y. D., Lu, Y. & McLellan, J. Template-assisted self-assembly of spherical colloids into complex and controllable structures, Advanced Functional Materials 13, 907-918 (2003).

[9] Cui, Y. et al. Integration of colloidal nanocrystals into lithographically patterned devices. Nano Letters 4, 1093-1098 (2004).

[10] Chen, K. M., Jiang, X. P., Kimerling, L. C. & Hammond, P. T. Selective self organization of colloids on patterned polyelectrolyte templates, Langmuir 16, 7825-7834 (2000).

[11]H. J. J. Yeh and J. Smith, "Fluidic self-assembly for the integration of GaAs lightemittingdiodes on Si substrates," Photonics Technology Letters, IEEE, vol. 6, pp. 706-708, 1994.

[12] Cheng, J. Y., Ross, C. A., Thomas, E. L., Smith, H. I. & Vancso, G. J. Fabrication of nanostructures with long-range order using block copolymer lithography, Applied Physics Letters 81, 3657-3659 (2002).

[13] T.L. Sobey et. al., Subdiffraction Single-Molecule Fluorescence Microscopy on DNA Origami, Proceedings of the conference on " Foundations of Nanoscience : Self-Assembled Architectures and Devices, p. 51-54, 2009.

[14] R. Chhabra et. al., Study of Photonic Intercations between Gold nanoparticles and Fluorescent Molecules using DNA as Scaffolds, Proceedings of the conference on " Foundations of Nanoscience : Self-Assembled Architectures and Devices, p. 51-54, 2009.

[15] Christophe Caloz, Tatsuo Itoh, Electromagnetic metamaterials: transmission line theory and microwave applications : the engineering approach, John Wiley and Sons, 2005

[16] Kante et. al., Metamaterials for optical and radio communications, Comptes Rendus Physique, 9 (2008) 31-40

[17] Valentine, J., et. al., Three-dimensional optical metamaterial with a negative refractive index, Nature 455, 376-379, 18 September 2008.

[18] C.T. Black et. al., Polymer self assembly in semiconductor microelectronics, IBM J. Res. And Dev., Vol. 51, No. 5 , September 2007.

[19] J.A. Ferguson et. al, High-Density Fiber-Optic DNA Random Microsphere Array, Anal. Chem. 2000, 72, 5618-5624

[20] A.W. Wun et. al., Non-linear transduction strategies for chemo/biosensing on small length scales, J. Mater. Chem., 2005, 15, 2697–2706

[21] S. Arnold, A. Gathon, SPECTROSCOPY OF PHOTONIC ATOMS: A MEANS FOR ULTRA-SENSITIVE SPECIFIC SENSING OF BIO-MOLECULES, Advances in Spectroscopy for Lasers and Sensing, 2006, 1–18.

[22] T. Walenzyk et. al., Synthesis of mono-dispersed spherical silica particles containing covalently bonded chromophores, International Journal of Cosmetic Science, 2005, 27, 177–189

[23] G.H. Lathe and C.R.J. Ruthven, The Separation of Substances and Estimation of their Relative Molecular Sizes by the use of Columns of Starch in Water, Biochem. J., 1956, 62, 665-674, PMID: 13249976

[24] J. N. Israelachvili, Intermolecular and Surface Forces. San Diego: Academic Press, 1991.

[25] Yaws, C.L., Chemical Properties Handbook , New York: McGraw-Hill, 1999. http://www.knovel.com/knovel2/Toc.jsp?BookID=49&VerticalID=0

[26] K. L. Johnson, Contact Mechanics. Cambridge: Cambridge University Press, 2003, pp. 406-411.

[27] Q. Qi and G. Brereton, "Mechanisms of removal of micron-sized particles by high-frequency ultrasonic waves," Ultrasonics, Ferroelectrics and Frequency Control, IEEE Transactions on, vol. 42, pp. 619-629, 1995.

[28] E. E. Michaelides, "Hydrodynamic force and heat/mass transfer from particles, bubbles, and drops—The Freeman Scholar Lecture," J. Fluids Eng., vol. 125, pp. 209-238, 2003.

[29] J. Jacobsen, A. Jayaraman, and A. Belmonte, "Monotone Solutions of a Nonautonomous Differential Equation for a Sedimenting Sphere," class notes for 34C60, Department of Mathematics, Penn. State University, Fall 2000.

[30] N. M. Kim and S. M. Kim, "Application of megasonic cleaner to sub-micron particles of SIL optical flying head," Microsys. Tech., vol. 9, pp. 225-231, 2003.

[31] G. Torr, "The acoustic radiation force," Amer. J. Phys., vol. 52, pp. 402, 1984.

[32] Department of Aerospace Engineering, University of Illinois at Urbana-Champaign, "Introduction to Multi-phase Fluid Dynamics." http://www.ae.uiuc.edu/~loth/CUP/Ch1text.pdf.

[33] P. K. Kundu and I. M. Cohen, Fluid Mechanics. San Diego: Elsevier Academic Press, 2004.

[34] N. Chaki and K. Vijayamohanan, "Self-assembled monolayers as a tunable platform for biosensor applications." Biosens. Bioelectron., vol. 2002, pp. 1-12, 2001.

[35] A. Nowicki, W. Secomski and J. Wójcik, "Acoustic streaming: Comparison of low-amplitude linear model with streaming velocities measured by 32-Mhz doppler," Ultrasound in Med. and Biol., vol. 23, 1997.

[36] S.M. Ali, P. Sahoo, "Elastic–plastic adhesive contact of rough surfaces based on plastic asperity concept" , Tribology Letters, Vol. 22, No. 2, May 2006.

[37] J.A. Greenwood and J.B.P. Williamson, Proc. R. Soc. Lond. A 295 (1966) 300.

[38] http://www.matweb.com/

[39] Gonzalo Vazquez, Estrella Alvarez, and Jose M. Navaza, Surface Tension of Ethyl Alcohol + Water from 20 to 50 .degree.C, *J. Chem. Eng. Data*, 1995, 40 (3), 611-614

[40] W. S. Bonnell, L. Byman, and D. B. Keyes, Surface Tension of Ethyl Alcohol-Water Mixtures, *Ind. Eng. Chem.*, 1940, 32 (4), 532-534

[41] Hertz, H., 1896, *Miscellaneous Papers by Heinrich Hertz*, MacMillan & Co, London, UK, p. 146–183.

[42] L. Kogut, I. Etsion, Elastic-Plastic Contact analysis of a sphere and a rigid flat, Journal of Applied Mechanics, Sep. 2002, Vol. 69.

[43] R.L. Jackson, I. Green, A finite element study of elasto-plastic hemispherical contact against a rigid flat, Journal of Tribology, April 2005, Vol. 127.

[44] Mesarovic, S. D., and Fleck, N. A., 2000, Frictionless Indentation of Dissimilar Elastic-Plastic Spheres, Int. J. Solids Struct., 37, pp. 7071–7091.

[45] Chang, W. R., Etsion, I., and Bogy, D. B., 1987, An Elastic-Plastic Model for the Contact of Rough Surfaces, ASME J. Tribol., 109, pp. 257 – 263

[46] Chang, W. R., Etsion, I., and Bogy, D. B., 1988, "Static Friction Coefficient Model for Metallic Rough Surfaces," ASME J. Tribol., 110, pp. 57–63.